MICROWAVE RADIOMETER INTER-CALIBRATION: ALGORITHM DEVELOPMENT AND APPLICATION

by

Rachael Ann Kroodsma

A dissertation submitted in partial fulfillment
of the requirements for the degree of
Doctor of Philosophy
(Atmospheric, Oceanic, and Space Sciences)
in the University of Michigan
2014

Doctoral Committee:

Asst. Res. Scientist Darren S. McKague, Co-Chair
Professor Christopher S. Ruf, Co-Chair
Professor Anthony W. England
Asst. Professor Derek J. Posselt
Professor Thomas T. Wilheit, Texas A&M University

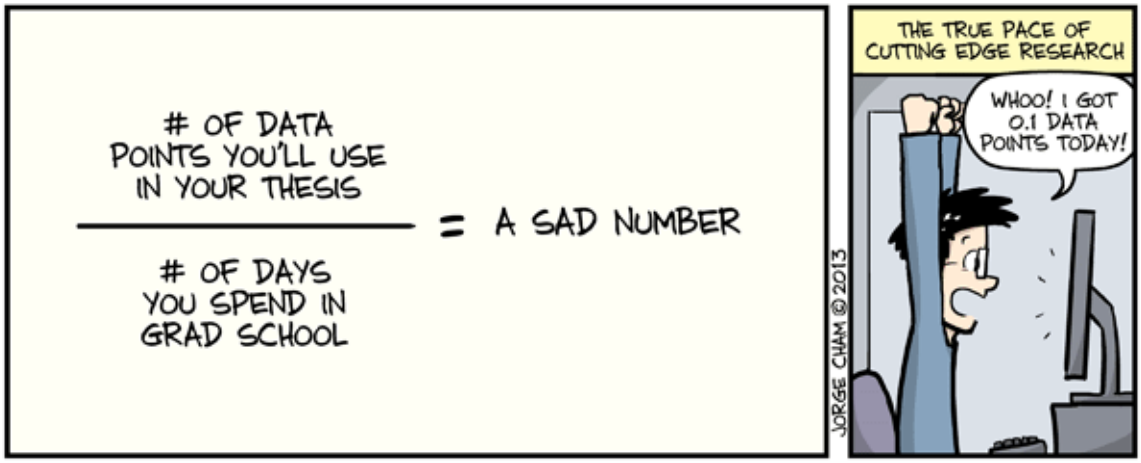

WWW.PHDCOMICS.COM

Dedication

To
My Mom

Who has always been there and
supported me in everything I do

Acknowledgements

I would like to foremost thank my co-advisors, Christopher Ruf and Darren McKague, for guiding me through graduate school and believing in me enough to take me on as their student. Thanks for your advice, your critique, and your encouragement. I have been very fortunate to have both of you as mentors.

I also want to thank the others who have aided me throughout my dissertation work. Thanks to my committee for your helpful comments on my dissertation. Thanks also to my collaborators on the GPM X-Cal team who have been instrumental in my continuing research and who I have learned a great deal from.

Thanks to the amazing faculty and staff in the AOSS department. You have been so helpful during the many years I have been here. AOSS has become my second home and I will miss the atmosphere (no pun intended!) of the department.

And finally thanks to my family and friends for all your support. Thanks for the laughter, the adventures, the shoulder to cry on, and all the conversations. My time at the University of Michigan was an experience I will truly never forget and will hold dear in my heart.

Table of Contents

Dedication ii
Acknowledgements iii
List of Figures vii
List of Tables xiv
List of Acronyms xvi
Abstract xvii
Chapter 1 Introduction 1
1.1 The Water Cycle and the Measurement of Precipitation 1
1.2 Theory and Measurement of Precipitation from Space 3
1.2.1 Theory of Radiometry 3
1.2.2 Microwave Remote Sensing 5
1.2.3 Spaceborne Radiometers 8
1.2.4 Spaceborne Microwave Radiometers: Roadmap to TRMM and GPM 10
1.2.5 The Tropical Rainfall Measuring Mission 12
1.2.6 The Global Precipitation Measurement Mission 15
1.3 Microwave Radiometer Calibration 17
1.3.1 On-Board Calibration 17
1.3.2 External Calibration 19
1.3.3 Vicarious Cold Calibration 20
1.3.4 Vicarious Warm Calibration 23
1.3.5 Inter-Calibration 24
1.4 Structure of Thesis 26
Chapter 2 Vicarious Cold Calibration: Application to Microwave Radiometers 28
2.1 Introduction 28
2.1.1 Vicarious Cold Calibration Theory 28
2.1.2 Vicarious Cold Calibration Algorithm Details 34
2.2 Vicarious Cold Cal TB for Microwave Imagers from 10 to 37 GHz 37
2.2.1 TB Histograms 37

2.2.2 Cold Cal TB Seasonal Variation 38
2.2.3 Cold Cal TB EIA Variation 43
2.3 Extension of Vicarious Cold Calibration to Higher Frequencies 46
2.3.1 Challenges with High Frequency Range: 85 – 92 GHz 46
2.3.2 Cold Cal TB at 89 GHz 47
2.3.3 TB Filters for Hydrometeor Scattering 49
2.4 Summary 52
Chapter 3 The Vicarious Cold Calibration Single Difference 53
3.1 Introduction 53
3.2 Single Difference for Microwave Imagers from 10 to 37 GHz 58
3.3 Extension of Single Difference to High Frequency Range 85 – 92 GHz 62
3.3.1 Introduction 62
3.3.2 Identification of Filters to Remove TBs Associated with Hydrometeor Scattering 64
3.3.3 Application of TB Filters 66
3.4 Application of the Single Difference: Satellite Attitude Analysis 73
3.4.1 Introduction 73
3.4.2 Pitch/Roll Retrieval Algorithm 75
3.4.3 Application to the WindSat Radiometer 76
3.5 Summary 79
Chapter 4 Vicarious Cold Calibration Double Difference Method for Inter-Calibration of Spaceborne Microwave Imagers 80
4.1 Introduction 80
4.1.1 Previous and Current Inter-Calibration Studies 80
4.1.2 Spaceborne Microwave Imagers for Inter-Calibration 82
4.1.3 Vicarious Cold Calibration Double Difference Method 84
4.2 Vicarious Cold Calibration Double Difference: Application to Microwave Imagers 86
4.2.1 Inter-Calibration of AMSR-E with TMI 87
4.2.2 Double Difference Seasonal Cycle Analysis 90
4.2.3 Diurnal Sampling Effect on the Double Difference 96
4.3 Inter-Calibration Uncertainty 100
4.3.1 Double Difference Comparisons using GDAS, ERA-I, and MERRA 101
4.3.2 Seasonal Cycle and Diurnal Variability in the Double Difference 103
4.3.3 Double Difference Uncertainty Calculation 109

4.4 Inter-Calibration Application: GPM Mission 112
4.5 Summary 116
Chapter 5 Impact of Inter-Calibration on Retrieved Rain for the Global Precipitation Measurement Mission 117
5.1 Introduction 117
5.2 Rain Retrieval using the WCC Algorithm 120
5.2.1 Algorithm Description 120
5.2.2 Rain Retrieval Results: Pre-Inter-Calibration 121
5.2.3 Rain Retrieval Results: Post-Inter-Calibration 123
5.2.4 Analysis 125
5.3 Rain Retrieval using the GPROF 2010 Algorithm 129
5.3.1 Algorithm Description 129
5.3.2 Rain Retrieval Results: Pre-Inter-Calibration 129
5.3.3 Rain Retrieval Results: Post-Inter-Calibration 132
5.3.4 Analysis 133
5.4 Sensitivity of Rain Retrieval Algorithms to Cold and Warm DDs 136
5.5 Summary 141
Chapter 6 Conclusions and Future Study 142
6.1 Summary 142
6.2 Contributions 144
6.3 Future Work 146
6.3.1 Application of Inter-Calibration to GMI 146
6.3.2 Development of a Middle Calibration Point 146
6.3.3 RTM Errors in the Inter-Calibration 147
6.3.4 Further Analysis of Inter-Calibration Impact on Retrieved Rain Rates 147
References 149

List of Figures

Figure 1.1: Planck function spectral brightness for the sun (top) and Earth (bottom)..... 4

Figure 1.2: TOA TB as seen by a spaceborne microwave radiometer. 7

Figure 1.3: Water vapor and oxygen absorption lines at microwave frequencies. 8

Figure 1.4: TB vs. SST for a clear sky, calm ocean scene at various V-pol (left) and H-pol (right) frequencies typical of microwave imagers at an EIA of 53°. 21

Figure 1.5: Sample TB histogram at 18.7 GHz V-pol for the entire range of over-ocean TBs (top) and just the cold end of the histogram (bottom). 22

Figure 1.6: SSM/I $|TB_{37V}-TB_{37H}|$. Green colors indicate regions of depolarization, with the darkest green indicating the greatest depolarized regions ($|TB_{37V}-TB_{37H}| = 0$). 24

Figure 1.7: SSM/I $|TB_{37V}-TB_{37H}|$ over South America. Green colors indicate regions of depolarization, with the darkest green indicating the greatest depolarized regions ($|TB_{37V}-TB_{37H}| = 0$). 24

Figure 2.1: Regions of SSTs associated with the coldest TBs for 19 GHz V-pol. The colors indicate the SSTs within +/- 5 K of 280 K, where the theoretical minimum TB for 19V occurs. 29

Figure 2.2: Regions of SSTs associated with the coldest TBs for 37 GHz H-pol. The colors indicate the SSTs within +/- 5 K of 301 K, where the theoretical minimum TB for 37H occurs. 29

Figure 2.3: Occurrence of TBs from the lower 10% of the histogram for AMSR-E 18.7V, overlayed on the SST regions that produce the theoretically coldest TBs. 30

Figure 2.4: Occurrence of TBs from the lower 10% of the histogram for AMSR-E 36.5H, overlayed on the SST regions that produce the theoretically coldest TBs. 31

Figure 2.5: Histograms of SST for AMSR-E 18.7V (left) and 36.5H (right) associated with all the TB observations for January 2006 (Total histogram) and the SSTs associated with the TBs in the coldest 10% of the TB histogram CDF. 32

Figure 2.6: Histograms of integrated water vapor for AMSR-E 18.7V (left) and 36.5H (right) associated with all the TB observations for January 2006 (Total histogram) and the SSTs associated with the TBs in the coldest 10% of the TB histogram CDF. 33

Figure 2.7: Histograms of wind speed for AMSR-E 18.7V (left) and 36.5H (right) associated with all the TB observations for January 2006 (Total histogram) and the SSTs associated with the TBs in the coldest 10% of the TB histogram CDF. 33

Figure 2.8: Example modeled TB histograms for 19 GHz viewing nadir (blue), 53° V-pol (green), and 53° H-pol (red). 35

Figure 2.9: 2nd degree polynomial fit to the inverse CDF from 2% to 10% of the TB histogram for 19 GHz V-pol (left) and H-pol (right). The cold cal TB is the value of the 2nd degree polynomial at 0% CDF. 36

Figure 2.10: AMSR-E 23.8V GHz observed cold cal TB over a year for the globe, NH, and SH. The NH cold cal TB shows a strong seasonal cycle, which is attributed to the large variation in water vapor throughout the year. 40

Figure 2.11: AMSR-E 10.65V GHz observed cold cal TB over a year for the globe, NH, and SH. This channel has a smaller seasonal cycle than 23.8 GHz since it is not as sensitive to atmospheric water vapor. 40

Figure 2.12: Occurrence of TBs from the lower 10% of the histogram for AMSR-E 18.7V for July 2005. The regions of the coldest TBs shift to the north in both the NH and SH due to sea ice extent. 42

Figure 2.13: Occurrence of TBs from the lower 10% of the histogram for AMSR-E 18.7V for January 2006. The regions of the coldest TBs shift to the south in both the NH and SH due to sea ice extent. 42

Figure 2.14: Dependence of TB on EIA for V-pol (left) and H-pol (right) channels. 43

Figure 2.15: Cold cal TB across the scan for AMSR-E 10.65 GHz V-pol for SH descending (left) and NH descending (right) orbits 45

Figure 2.16: Scan dependent EIAs for AMSR-E SH descending (left) and NH descending (right) orbits. The EIA is the same for all low resolution AMSR-E frequencies and polarizations. 45

Figure 2.17: Comparison of AMSR-E 89 GHz V-pol TB histogram (top) with the 10.65 GHz V-pol TB histogram (bottom) for January 2006. The long cold tail present for 89V is due to hydrometeor scattering, while 10V has a much sharper lower bound and a restricted cold tail primarily due to additive noise. The long cold tail can destabilize the vicarious cold calibration statistic if not properly filtered. 48

Figure 2.18: Cold cal TB for AMSR-E 89V (top) and 89H (bottom). A seasonal cycle in the cold cal TB is present for both polarizations, but stronger for H-pol. The range of variation over the year is approximately 4 K for V-pol and 9 K for H-pol. 49

Figure 2.19: 2D histograms of 89 GHz vs. 18.7 GHz (top), 23.8 GHz (middle), and 36.5 GHz (bottom). The left column shows V-pol and the right shows H-pol. Colors indicate

number of TB counts. Low 89 GHz TBs tend to be correlated with high TBs at the lower frequencies. 51

Figure 3.1: AMSR-E observed 23.8V TBs (left) and simulated 23.8V TBs (right). The simulated TBs are generated for every pixel location. 55

Figure 3.2: Example of the observed TB histogram (blue line) and simulated TB histogram (green line) for AMSR-E 36.5 GHz V-pol. Although the overall shapes of the histograms differ, the shape at the cold end is similar which is what factors into vicarious cold calibration..... 56

Figure 3.3: AMSR-E 18.7V observed (top) and simulated (bottom) TBs for the coldest 10% CDF of the total TB histogram for January 2006. 57

Figure 3.4: Comparison of AMSR-E observed cold cal TB (black line) and single difference (green line) for the NH. The simulated TBs are able to model the geophysical variability and reduce the seasonal cycle. 60

Figure 3.5: Observed cold cal TB and single difference across the scan for AMSR-E 10.65V SH descending orbits. The simulations are able to model the EIA variation across the scan and reduce the variation for the single difference. 61

Figure 3.6: Cold cal TB for AMSR-E 89V observed and simulated TBs (top) and single difference (bottom) by month for July 2005 - June 2006. The simulations are able to model the seasonal variation in the cold cal TB and reduce it in the single difference.... 63

Figure 3.7: Cold cal TB for AMSR-E 89H observed and simulated TBs (top) and single difference (bottom) by month for July 2005 - June 2006. The simulations are able to model the seasonal variation in the cold cal TB and reduce it in the single difference.... 63

Figure 3.8: 2D histogram of 89V observed TBs minus simulated TBs vs. cloud top temperature for January 2006. Colors indicate number of counts. The magnitude of the scattering increases with decreasing CTT..... 65

Figure 3.9: Cloud top temperature vs. SST 2D histogram for January 2006. Colors indicate number of counts. Most of the very cold CTTs occur at high SSTs. 66

Figure 3.10: Observed and simulated cold cal TB using different filter thresholds for 37V – 37H..... 68

Figure 3.11: Single difference and the derivative of the single difference with respect to the TB threshold. A threshold of 50 K is a reasonable value for the filter. 68

Figure 3.12: Single difference for AMSR-E 89V with various filters applied. The precipitation filter and CTT filter give the best performance. 70

Figure 3.13: TB histograms for 89V with various filters applied. The precipitation filter removes the largest percentage of the cold tail. 71

Figure 3.14: Single difference for AMSR-E 89H with various filters applied. The filters do not have as significant an impact on the cold cal TB for H-pol as they do for V-pol. 72

Figure 3.15: TB histograms for 89H with different filters applied. The bottom plot has a smaller TB range to highlight the cold tail. H-pol does not have a significant cold tail, but the precipitation filter removes what little tail there is. 72

Figure 3.16: Geometry of the EIA for a spaceborne microwave radiometer..... 74

Figure 3.17: Positive roll and pitch angles of a satellite. The grey shaded area indicates the front of the satellite, i.e the forward-looking side of the satellite. 76

Figure 3.18: Observed cold cal TB across the scan for the WindSat 10.7V GHz channel. 77

Figure 3.19: Modeled cold cal TB at 0° pitch/roll with modeled cold cal TB at a pitch of 0.18° and roll of -0.21° compared with the observed cold cal TB for the WindSat 10.7V GHz channel..... 78

Figure 3.20: EIA across the scan for a derived pitch of 0.18° and roll of -0.21° for the WindSat 10.7V GHz channel at an altitude of 830 km..... 78

Figure 4.1: Flow diagram of the vicarious cold calibration double difference method.... 85

Figure 4.2: AMSR-E - TMI double difference by channel and month for July 2005 - June 2006..... 88

Figure 4.3: Ascending - descending double differences for AMSR-E - TMI. The descending orbits give a slightly higher double difference value than the ascending orbits for most channels, especially H-pol. 89

Figure 4.4: Single difference for 22V channel by month for TMI and AMSR-E. AMSR-E single difference has a slight seasonal cycle while TMI has a cycle that is a greater by a factor of two. 92

Figure 4.5: Single difference for 22V channel by month for TMI and AMSR-E using data with latitudes limited to TMI observed latitudes (40°S to 40°N). Limiting the latitudes of AMSR-E produces a seasonal cycle in the single difference similar to TMI. 92

Figure 4.6: Double difference AMSR-E - TMI using all AMSR-E data (globe) compared with using AMSR-E data with latitudes limited to TMI observed latitudes. Limiting the AMSR-E data to TMI latitudes decreases the seasonal cycle of the double difference by about a factor of two. 93

Figure 4.7: Occurrence of TBs from the lower 10% of the histogram for AMSR-E 18.7V for July 2005, limiting the latitudes to ± 40°. 94

Figure 4.8: Occurrence of TBs from the lower 10% of the histogram for AMSR-E 36.5H for July 2005, limiting the latitudes to ± 40°. 94

Figure 4.9: Double difference by month and channel for AMSR-E – TMI. 96

Figure 4.10: Ascending DD - descending DD for AMSR-E - TMI comparing AMSR-E all latitude data versus limiting the AMSR-E latitudes to those observed by TMI. 97

Figure 4.11: Ascending DD - descending DD for AMSR-E - TMI comparing three different filters: TMI filtered to AMSR-E local times with AMSR-E limited latitudes (triangles), AMSR-E limited latitudes to +/- 40° (squares), and AMSR-E and TMI using all data (circles). 98

Figure 4.12: Vicarious cold calibration double difference values for F13 - TMI using three different simulation re-analysis field inputs: GDAS, ERA-I, and MERRA. The different re-analysis fields do not all give the same double difference value, implying that the double difference is not able to completely remove errors in the RTM geophysical input fields. 102

Figure 4.13: Vicarious cold calibration double difference values for AMSR-E - TMI using three different simulation reanalyses for RTM inputs: GDAS, ERA-I, and MERRA. 103

Figure 4.14: Ascending DD - descending DD for F13 – TMI using GDAS, ERA-I, and MERRA as simulation inputs. The only channel to show any significant difference among the three reanalyses is 19H which has a spread of less than 0.3 K. 105

Figure 4.15: Ascending DD - descending DD for AMSR-E – TMI using GDAS, ERA-I, and MERRA as simulation inputs. GDAS and ERA-I show fairly good agreement at all channels while MERRA appears to be an outlier, especially for 90V and 90H. 105

Figure 4.16: TMI single difference by local time using GDAS, ERA-I, and MERRA for geophysical inputs to the RTM. If the simulations are able to correctly model diurnal variation in the cold cal TB, the single difference should be flat across all local times but this is not the case for most channels. 109

Figure 4.17: AMSR2 inter-calibration offsets with TMI as calculated by the 4 members of the GPM X-Cal group. The UM vicarious cold calibration double difference method gives very consistent results with the other methods of inter-calibration. 115

Figure 5.1: Calibration differences between SSM/I F15 and TMI for all similar channels. 119

Figure 5.2: July 2005 rain accumulations for TMI (top) and SSM/I F15 (bottom). TMI appears to retrieve higher rain accumulations than F15, especially near the equator. 121

Figure 5.3: Zonal mean difference of rain accumulations for SSM/I F15 – TMI from July 2005 – June 2006. The greatest difference in rain occurs near the tropics. 122

Figure 5.4: SSM/I F15 rain accumulation versus TMI rain accumulation, divided into the sub-tropics (grey) and the tropics (blue). The black line is the 1:1 line. TMI generally retrieves higher rain accumulation amounts than F15. 123

Figure 5.5: Zonal mean difference of rain accumulations for inter-calibrated F15 – TMI from July 2005 – June 2006. The large difference in the tropics has been greatly reduced. 124

Figure 5.6: Inter-calibrated F15 rain accumulation versus TMI rain accumulation, divided into the sub-tropics (grey) and the tropics (blue). The black line is the 1:1 line. The rain accumulations show better agreement when F15 is inter-calibrated to TMI. 125

Figure 5.7: Scatter plots of F15 vs. TMI pre-inter-calibration (left) and post-inter-calibration (right) rain accumulation differences, divided into the sub-tropics (grey) and the tropics (blue). The black line is the 1:1 line and the red line is the line of best fit. .. 126

Figure 5.8: t-statistic values for TMI/F15 (top) and TMI/F15 inter-calibrated (bottom). 13.1% of grid boxes reject the null hypothesis for F15 unadjusted while only 1.5% reject it when F15 is inter-calibrated to TMI. 128

Figure 5.9: July 2005 rain accumulations for TMI (top) and SSM/I F15 (bottom). 130

Figure 5.10: Zonal mean difference of rain accumulations for SSM/I F15 – TMI from July 2005 – June 2006. The difference is not nearly as large as the difference using the WCC algorithm for Level 3 rain accumulation. 131

Figure 5.11: SSM/I F15 rain accumulation versus TMI rain accumulation. The black line is the 1:1 line. It appears that TMI and F15 retrieve fairly similar rain accumulations with some scatter. 131

Figure 5.12: Zonal mean difference of rain accumulations for SSM/I F15 intercal – TMI from July 2005 – June 2006. There is a noticeable improvement in the consistency of rain accumulations near the equator. 132

Figure 5.13: Inter-calibrated SSM/I F15 rain accumulation versus TMI rain accumulation. The black line is the 1:1 line. The rain accumulations do not appear to shift much from the pre-inter-calibration scatter plot. 133

Figure 5.14: Scatter plots of F15 rain accumulations compared with TMI (left), and F15 inter-calibrated rain accumulations compared with TMI (right), along with the 1:1 line (black line) and the line of best fit to the data (red line). There is a slight improvement to the rain consistency when F15 is inter-calibrated to TMI. 134

Figure 5.15: WCC zonal mean rain differences F15 - TMI comparing three different types of inter-calibration: constant bias using the cold end DD (intercal cold), constant bias using the warm end DD (intercal warm) and the linear interpolation between the cold and warm DDs (intercal). 138

Figure 5.16: G10 zonal mean rain differences F15 - TMI comparing three different types of inter-calibration: constant bias using the cold end DD (intercal cold), constant bias using the warm end DD (intercal warm) and the linear interpolation between the cold and warm DDs (intercal). 138

List of Tables

Table 2.1: Mean of the geophysical variables (SST, integrated water vapor, and wind speed) associated with the TBs for the total histogram and the 10% CDF histogram for AMSR-E channels. 34

Table 2.2: AMSR-E seasonal cycle amplitudes for the global cold cal TB. 41

Table 3.1: Summary of results for the observed cold cal TB and single difference seasonal cycle amplitude. The single difference has a smaller seasonal cycle amplitude than the observed cold cal TB, most notably for the 23.8 GHz water vapor channel. 60

Table 3.2: Single difference for AMSR-E channels, averaged over July 2005 - June 2006. 60

Table 3.3: Single difference for AMSR-E channels, averaged over July 2005 - June 2006 using simulated TBs that use a wind speed of 0 m/s for all pixels instead of the GDAS wind speed. 61

Table 4.1: Past, current, and future conical scanning microwave radiometers used for inter-calibration. The radiometers have similar channels, but vary slightly in frequency, EIA, and orbits. The '--' symbol in the local crossing time column indicates a radiometer in non-sun-synchronous orbit which views all local times. 83

Table 4.2: Mean of the geophysical variables (SST, integrated water vapor, and wind speed) associated with the TBs for the total histogram and the 10% CDF histogram for the AMSR-E channels, limiting the latitudes to ± 40° 95

Table 4.3: Comparison between the AMSR-E and TMI double difference standard deviation with limiting AMSR-E latitudes versus using all AMSR-E data. Limiting the AMSR-E latitudes results in a smaller standard deviation for all channels. 96

Table 4.4: Double differences AMSR-E - TMI for 3 cases of data filtering. Case 1: Using all AMSR-E and TMI data. Case 2: Filtering AMSR-E TBs to include only those data from 40°S to 40°N. Case 3: Filtering the AMSR-E TBs to the latitude range from Case 2 and filtering the TMI TBs to include only local times from 00:00 to 03:00 and 12:00 to 15:00. 99

Table 4.5: Values of the F13 - TMI double difference using GDAS, ERA-I, and MERRA as simulation inputs. The spread (max DD among the three minus the min DD) is also shown. The 22V and H-pol channels show the greatest spread. 19V, 37V, and 85V channels all have a spread <= 0.1 K which is considered insignificant. 102

Table 4.6: Values of the AMSR-E - TMI double difference using GDAS, ERA-I, and MERRA as simulation inputs. The spread (max DD among the three minus the min DD) is also shown. 103

Table 4.7: Standard deviation of the F13 DDs for 12 months (July 2005 - June 2006) using the three reanalyses GDAS, ERA-I, and MERRA. 104

Table 4.8: Standard deviation of the AMSR-E DDs for 12 months (July 2005 - June 2006) using the three reanalyses GDAS, ERA-I, and MERRA. 104

Table 4.9: Standard deviation of the DD for F13 and AMSR-E using GDAS, ERA-I, and MERRA. The lowest standard deviations occur for 10V, 10H, and 37V, while the highest standard deviations occur for 22V, 90V, and 90H. 110

Table 4.10: Double differences (μ_{tot}) and errors of the double differences (σ_{tot}) by channel for F13 and AMSR-E inter-calibrated to TMI. 111

Table 5.1: Inter-calibration differences for F15 - TMI at a cold temperature and warm temperature. These numbers were found using vicarious cold calibration for the cold DD and the Amazon warm calibration for the warm DD. 119

Table 5.2: Average rain accumulation difference (F15 - TMI) pre- and post-inter-calibration for three globe regions. All regions show a decrease in the rain difference between F15 and TMI after inter-calibration but TMI still retrieves higher rain amounts. 126

Table 5.3: Average rain accumulation difference for three regions: globe (all latitudes), tropics (20°S to 20°N) and sub-tropics (40°S to 20°S and 20°N to 40°N). 134

List of Acronyms

AMSR-E	Advanced Microwave Scanning Radiometer for the Earth Observing System
AMSR2	Advanced Microwave Scanning Radiometer 2
APC	Antenna Pattern Correction
CDF	Cumulative Distribution Function
CLW	Cloud Liquid Water
CSU	Colorado State University
CTT	Cloud Top Temperature
DD	Double Difference
EIA	Earth Incidence Angle
ERA-I	European Center for Medium Range Weather Forecasting Interim Reanalysis
ESMR	Electrically Scanning Microwave Radiometer
GDAS	Global Data Assimilation System
GEO	Geostationary Earth Orbit
GPM	Global Precipitation Measurement
GMI	GPM Microwave Imager
GPROF	Goddard Profiling algorithm
G10	GPROF 2010
H-pol	Horizontal polarization
IR	InfraRed
ITCZ	Inter-Tropical Convergence Zone
LEO	Low Earth Orbit
MERRA	Modern Era Reanalysis
MODIS	Moderate Resolution Imaging Spectroradiometer
NASA	National Aeronautics and Space Administration
NEDT	Noise Equivalent Delta Temperature
NH	Northern Hemisphere
PR	Precipitation Radar
RTM	Radiative Transfer Model
SD	Single Difference
SH	Southern Hemisphere
SMMR	Scanning Multichannel Microwave Radiometer
SSM/I	Special Sensor Microwave/Imager
SSMIS	Special Sensor Microwave Imager Sounder
SSS	Sea Surface Salinity
SST	Sea Surface Temperature
TA	Antenna Temperature
TAMU	Texas A&M University
TB	Brightness Temperature
TOA	Top of Atmosphere
TRMM	Tropical Rainfall Measuring Mission
TMI	TRMM Microwave Imager
UCF	University of Central Florida
UM	University of Michigan
V-pol	Vertical Polarization
WCC	Wilheit, Chang, and Chiu algorithm
X-Cal	GPM Inter-Calibration Working Group

Abstract

Microwave radiometer inter-calibration is an essential component of any effort to combine measurements from two or more radiometers into one dataset for scientific studies. One spaceborne instrument in low Earth orbit is not sufficient to perform long-term climate studies or to provide measurements more than twice per day at any given location on Earth. Measurements from several radiometers are necessary for analyses over extended temporal and spatial ranges. In order to combine the measurements, the radiometers need to be inter-calibrated due to the instruments having unique instrument designs and calibrations. Inter-calibration ensures that consistent scientific parameters are retrieved from the radiometers.

The development of a cold end inter-calibration algorithm is presented. The algorithm makes use of vicarious cold calibration, along with the double difference method, to calculate calibration differences between radiometers. The performance of the algorithm is characterized using data from current conical scanning microwave radiometers. The vicarious cold calibration double difference is able to sufficiently account for design differences between two radiometers including frequency, earth incidence angle, and orbital characteristics. An estimate of the uncertainty in the inter-calibration algorithm is given as a result of potential errors in the geophysical inputs and improper accounting of seasonal and diurnal variability.

The vicarious cold calibration double difference method is shown to be a valid and accurate inter-calibration algorithm. Results are compared with calibration

differences calculated using alternate algorithms and sufficient agreement is attained. Inter-calibration is shown to be necessary for achieving consistency in retrieved scientific parameters by using the vicarious cold calibration double difference method to inter-calibrate two radiometers that are then used to derive rain accumulations. Inter-calibration results in a significant improvement in the rain accumulation agreement between the radiometers. This validates inter-calibration algorithm development and shows that it has a positive impact on achieving consistency in scientific parameter retrievals.

Chapter 1
Introduction

1.1 The Water Cycle and the Measurement of Precipitation

Many atmospheric, land surface, and ocean interactions and processes are driven by the global water cycle. Monitoring the global water cycle, which includes understanding the distribution and amount of water on Earth, is critical since water is necessary for life to exist. The consensus is that the water cycle experienced intensification during the twentieth century [1],[2]. In order for this intensification to be better understood, modeled, and predicted, the water cycle needs to be accurately measured.

One way to monitor the water cycle is through the measurement of precipitation. Precipitation is an important component of the global water cycle, as it has a direct impact on Earth's hydrology and dictates the global energy balance through latent heat release. Increased knowledge of precipitation leads to a greater understanding of the global water cycle and how it is changing. Recent studies have shown a correlation between warmer temperatures and extreme precipitation events [3],[4]. Studies of the link between global warming and precipitation are increasingly important as global warming intensifies.

Since precipitation is an important contributor to the water cycle, there have been many efforts over the past decades to measure it. The oldest measurements of precipitation come from rain gauges, but there are two significant problems with using gauges: (1) gauges are subject to many errors; and (2) gauges only perform point

measurements. Large uncertainties in the precipitation measurements from gauges are a result of environmental conditions, such as wind, and properties of the gauge, such as installation and variations in the design [5]. The second concern with gauges is that they only make measurements at a single point and are mostly concentrated over land in developed countries. This leaves at least 70% of the Earth mostly unmeasured since gauge measurements over the ocean are rarely made, and the measurements that are made come primarily from gauges on board ships which can introduce further errors in the measurements (e.g. water splash from the ocean surface). Efforts have been made to combine rain gauge measurements into a global dataset [6], but due to the poor spatial and temporal sampling, relatively large errors result, especially in over-ocean regions.

Higher frequency temporal and spatial sampling of precipitation measurements is needed if the full range of precipitation events is to be monitored. Precipitating systems can vary from convective storms with a temporal scale of minutes and a spatial scale of hundreds of meters to large storm fronts which can have a temporal scale of days and a spatial scale of hundreds of kilometers [7]. In order to properly monitor the water cycle, precipitation needs to be measured at these various temporal and spatial scales both over land and the ocean. This cannot be done using only *in situ* gauge measurements. A better solution is to make measurements remotely from space. The next section will discuss the theory behind measuring precipitation using passive remote sensing and present a brief history of the instruments used to measure precipitation from space.

1.2 Theory and Measurement of Precipitation from Space

1.2.1 Theory of Radiometry

All objects with a temperature above absolute zero radiate electromagnetic energy due to thermally induced vibration. The temperature of the object determines the frequency spectrum over which the energy is radiated. This relationship is known as Planck's function given by

$$B_f = \frac{2hf^3}{c^2}\left(\frac{1}{e^{hf/kT}-1}\right) \tag{1.1}$$

where B_f is the blackbody spectral radiance (W/m^2/sr/Hz), h is Planck's constant 6.63e-34 J·s, f is frequency in Hz, k is Boltzmann's constant 1.38e-23 J/K, T is the temperature in Kelvins (K), and c is the speed of light 2.998e8 m/s. In passive remote sensing, this emitted radiation is measured and properties of the object can be inferred. The most common forms of passive remote sensing use the microwave and infrared (IR) ranges of the electromagnetic spectrum. Given the effective radiating temperature of an object, the frequency spectrum over which it radiates can be calculated from Planck's function. The sun's effective radiating temperature is approximately 5700 K while the Earth's is 255 K. This net effective temperature for the Earth is the result of the balance between incoming solar radiation and outgoing radiation from the Earth, assuming an Earth albedo of 0.3. Figure 1.1 shows the spectral radiance for both the sun (top) and Earth (bottom). The sun's emission peaks in the visible range at ~500 nanometers. Visible and near IR spaceborne radiometers measure emission originating from the sun, e.g. radiation reflected off of clouds. On the other hand, the Earth's emission peaks in the IR range at ~11 micrometers so longwave IR radiometers measure radiation emitted from the Earth. While the Earth's radiation peaks in the IR range, it also emits a small amount of

radiation in the microwave spectrum. This is the radiation that is remotely sensed using microwave radiometers.

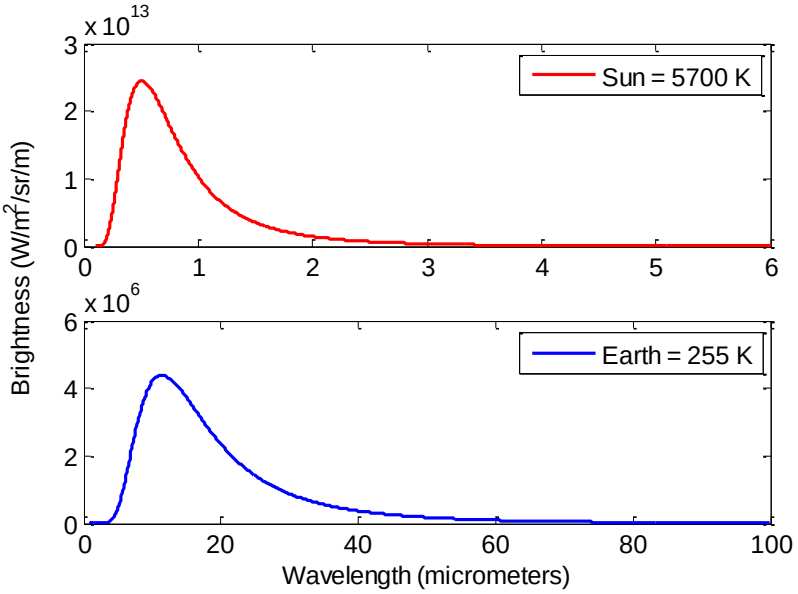

Figure 1.1: Planck function spectral brightness for the sun (top) and Earth (bottom).

The Earth's surface and atmosphere contribute to the total radiation observed by a spaceborne radiometer. However, not all radiation emitted from the surface or from the lower atmosphere will make it to the top of atmosphere (TOA). Electromagnetic waves interact with particles in the atmosphere where the radiation can be both scattered and absorbed. The degree of scattering and absorption depends, among other things, on the size of the particle relative to the wavelength. Rayleigh scattering occurs when the particle size and wavelength are related as

$$x = \frac{2\pi r}{\lambda} \ll 1 \tag{1.2}$$

where r is the radius of a spherical particle and λ is the wavelength of radiation. The variable x in (1.2) is referred to as the size parameter. Mie scattering is defined as the case when (1.2) does not hold true because the size parameter is of order unity and the

particle is comparable to the wavelength. Geometric scattering is the third type of scattering, which occurs when the size parameter is much larger than the wavelength ($x >> 1$).

Some common atmospheric particles that will interact with Earth's radiation are cloud droplets and raindrops. Cloud droplets can be as large as 100 μm, drizzle up to about 500 μm, and raindrops up to 6 mm [8]. A typical thermal IR wavelength of 10 μm is much smaller than any of these particles, giving a size parameter of approximately 30 for cloud droplets, 150 for drizzle, and 1800 for raindrops. This places the scattering type in the geometric region, so most IR wavelengths emitted from the surface below a dense cloud will not reach the TOA to be sensed by a spaceborne IR radiometer. Instead, the radiometer will measure radiation emitted from cloud tops and, in those regions where there are no clouds, the surface with some contribution by the atmosphere. On the other hand, a typical microwave wavelength of 1 cm is much larger than cloud droplets (size parameter 0.03, Rayleigh scattering) but is on the order of raindrops (size parameter 1.8, Mie scattering). Microwaves easily pass through clouds without being scattered and with little to moderate absorption, allowing a spaceborne microwave radiometer to measure radiation that originates from the Earth's surface as well as the atmosphere below the clouds, including precipitation.

1.2.2 Microwave Remote Sensing

For frequencies in the microwave spectrum below 300 GHz, when $hf/kT << 1$, Planck's equation simplifies to the Rayleigh-Jeans approximation. This approximation is important since it shows that, in the microwave regime, the brightness of an object is linearly proportional to its physical temperature, or

$$B_f = \frac{2f^2kT}{c^2} = \frac{2kT}{\lambda^2} \tag{1.3}$$

A brightness temperature (TB) can be defined as the physical temperature an object would need to be to produce the same B_f as that observed if it were a blackbody. Objects that are not blackbodies have emissivities ε less than 1 as defined by

$$\varepsilon = \frac{TB}{T} \tag{1.4}$$

In the absence of scattering, the microwave TOA TB can be derived using a Radiative Transfer Model (RTM) for the atmosphere that only accounts for absorption. The TOA TB as seen by a spaceborne microwave radiometer is calculated according to [9]

$$TB_{TOA} = TB_{up} + \left[\varepsilon_s(f,\theta)T_s + (1-\varepsilon_s(f,\theta))\left(TB_{dn} + T_c e^{-\tau(f)\sec\theta}\right)\right]e^{-\tau(f)\sec\theta} \tag{1.5}$$

where the optical depth τ is given by

$$\tau(f) = \int_0^{TOA} \alpha(f,z)dz \tag{1.6}$$

and the upwelling (TB_{up}) and downwelling (TB_{dn}) brightness temperatures are given by

$$TB_{up} = \sec\theta \int_0^{TOA} \alpha(f,z)T(z)\exp\left(-\sec\theta\int_0^{TOA}\alpha(f,z')dz'\right)dz \tag{1.7}$$

$$TB_{dn} = \sec\theta \int_0^{\infty} \alpha(f,z)T(z)\exp\left(-\sec\theta\int_0^{z}\alpha(f,z')dz'\right)dz \tag{1.8}$$

TB_{up} and TB_{dn} are functions of the frequency f, earth incidence angle (EIA) θ, absorption coefficient profile $\alpha(f,z)$, and temperature profile $T(z)$. The TOA TB is then calculated from TB_{up}, TB_{dn}, the surface emissivity $\varepsilon_s(f,\theta)$, surface temperature T_s, the cosmic background temperature T_c, and the optical depth τ. The surface emissivity is a function of frequency and EIA, and the optical depth is a function of frequency. Figure

1.2 gives a graphical representation of microwave radiative transfer through the atmosphere.

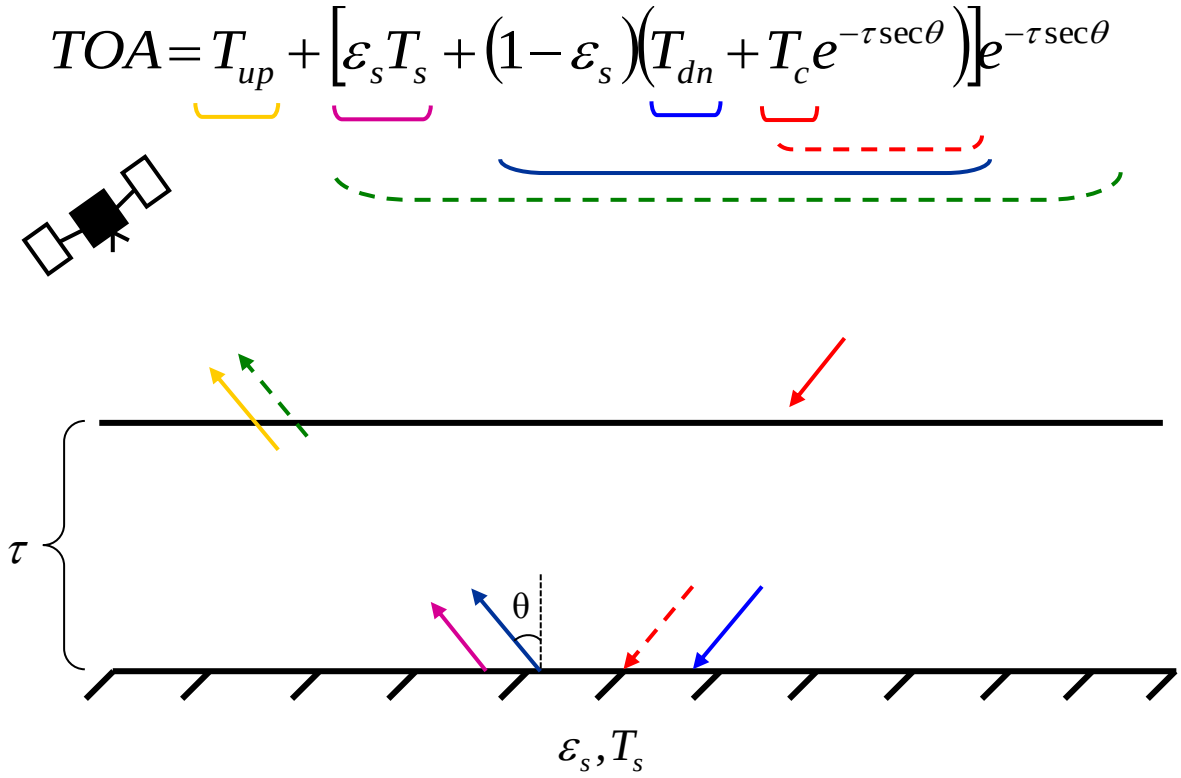

Figure 1.2: TOA TB as seen by a spaceborne microwave radiometer.

The main contributors to atmospheric absorption at microwave frequencies are water vapor, oxygen, and liquid water. Water vapor and oxygen both have absorption lines in the microwave spectrum as shown in Figure 1.3. This figure was created using the Rosencrantz 1998 [10] model for water vapor and the Liebe 1992 [11] model for oxygen absorption. Standard surface properties are assumed: a pressure of 1013 mb, temperature of 295 K, and water vapor density of 7.5 g/m^3. Water vapor has absorption lines centered at 22.235 GHz and 183.31 GHz in the microwave. Oxygen has a series of absorption lines from 49.96 to 69.49 GHz and a line centered at 118.75 GHz. In the lower

troposphere, pressure broadening causes the individual lines between 49.96 and 69.49 GHz to broaden into a single line.

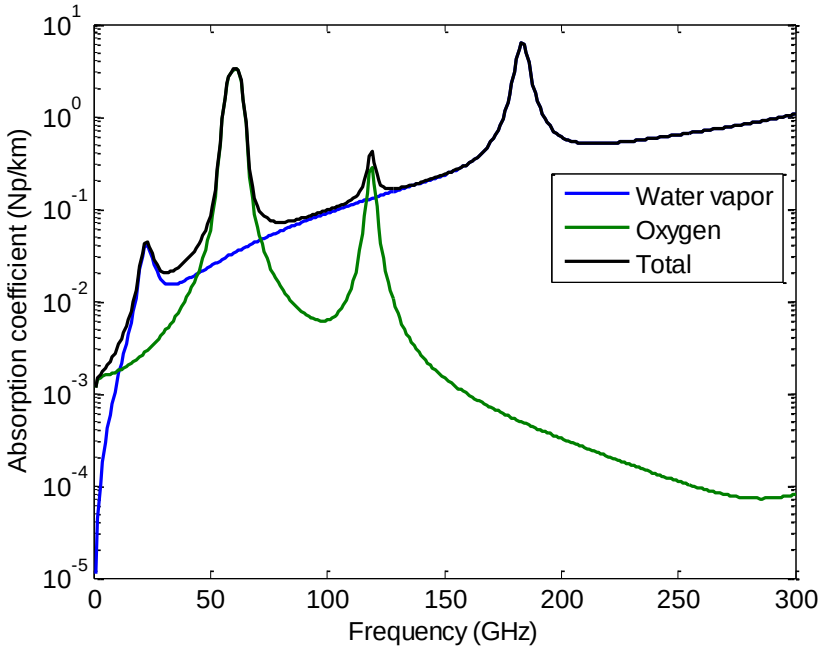

Figure 1.3: Water vapor and oxygen absorption lines at microwave frequencies.

1.2.3 Spaceborne Radiometers

In the 1970s, the first Geostationary Earth Orbit (GEO) satellites dedicated to meteorological applications were launched. The instruments onboard these satellites operated in the IR and visible bands. GEO satellites are placed at a distance of approximately 36,000 km from Earth and directly above the equator, giving a full Earth image between approximately 80°S and 80°N. This provides almost global coverage with measurements available nearly every 15 minutes. If the IR and visible radiometers in GEO could be used to measure precipitation, this would provide a vast improvement in both spatial and temporal resolution compared to gauges.

Unfortunately, it has been determined that IR and visible radiometers are more useful in estimating areas of rain, rather than rain rates themselves. After launching these instruments in GEO, several algorithms were developed in an attempt to use the IR and visible measurements to derive precipitation (e.g. [12]-[14]). However, since IR and visible typically measure what is occurring at the cloud tops and are not able to penetrate into or below the clouds; these measurements are only indirectly related to precipitation. This means that a relationship has to be inferred between what is happening at the cloud tops and what is going on below the clouds. If used to estimate rain rates, the many assumptions made with IR and visible can cause significant errors in the measurements [15]. Since it is desirable to have an accurate quantitative estimate of rain rather than just areas of rain, different instruments besides IR or visible radiometers need to be used.

Microwaves interact directly with the precipitation below the cloud and can give a quantitative measure of rain rates, offering a more physically-based precipitation retrieval than visible or IR. Microwave radiometers are therefore preferred for making precipitation measurements from space but a disadvantage is that the instruments have yet to fly in GEO. The antenna required for microwave radiometers at that distance from Earth is too large to be manufactured to achieve sufficient spatial resolution. As a result, microwave radiometers are limited for use on Low Earth Orbit (LEO) satellites where the antenna is a reasonable size that gives adequate spatial resolution. The disadvantage with LEO is that the revisit time of the satellite is only about once per day at any given location on Earth. This is not a sufficient temporal resolution to observe most precipitation events, which typically have time scales on the order of minutes to hours. Despite this fact, microwave radiometers are still preferred as the primary instrument for

measuring precipitation compared to IR or visible because of the physically-based precipitation retrieval.

The first spaceborne microwave radiometers to be launched were not designed specifically to measure precipitation, but they had channels that were sensitive to precipitation and were used to develop retrieval algorithms. These radiometers paved the way for two satellites with radiometers onboard that were developed specifically for measuring precipitation: the Tropical Rainfall Measuring Mission (TRMM), currently in operation, and the Global Precipitation Measurement (GPM) Core Observatory, set to launch in February 2014.

1.2.4 Spaceborne Microwave Radiometers: Roadmap to TRMM and GPM

One of the first microwave radiometers on an Earth-orbiting spacecraft was the Electrically Scanning Microwave Radiometer (ESMR) on Nimbus 5, launched in 1972 [16]. This instrument had one channel at 19.35 GHz horizontal polarization and was launched with the objectives of observing the atmosphere and developing models to measure atmospheric parameters. While ESMR was not designed specifically to measure precipitation, it provided some of the first rain measurements derived using a spaceborne microwave radiometer [17] and aided in the development of one of the first models for retrieving rainfall from microwave radiometers [18]. One of the drawbacks to using ESMR for rain measurements was that only rain over ocean could be measured. The ocean has a low emissivity, thereby providing a cold background against the rain that increases the TOA TB through absorption. The high emissivity of land causes rain over land to be almost indistinguishable from the land surface when using just one channel. Another drawback is that using one channel for rain retrieval creates an under-

constrained model, so a unique rain rate cannot be retrieved. Additional channels are needed to help constrain the retrieval and obtain more accurate rain measurements.

A second ESMR instrument was launched in 1975 on Nimbus 6 [19] with similar scientific objectives to ESMR-5 but with a different design. The three main changes to ESMR-6 were the frequency, polarization, and look angle. ESMR-6 had a frequency centered at 37 GHz with both vertical and horizontal polarization and viewed the Earth at a constant 45° look angle. The two polarizations provided a way to determine areas of rain over land. Using just one polarization, areas of rain over land and inland lakes can look very similar, but using the two polarizations allowed for distinguishing between inland lakes (highly polarized) and regions of rain (less polarized) [20]. The ESMR instruments confirmed that 19.35 GHz and 37 GHz were two useful frequencies for retrieving rain rates.

The Scanning Multichannel Microwave Radiometer (SMMR) [21] and the Special Sensor Microwave/Imager (SSM/I) [22], were two radiometers launched after ESMR that had channels able to measure precipitation. SMMR was launched in 1978 on two different platforms. The radiometer included five frequencies, all dual-polarized, at 6.63, 10.69, 18.0, 21.0, and 37.0 GHz. Unfortunately, SMMR had significant calibration issues, which resulted in an unreliable absolute calibration of the TBs. This meant that accurate rain rates were not retrievable from the instrument. SSM/I was first launched in 1987, with an additional six SSM/I instruments launched over the following 13 years on different platforms. The radiometers were built with four frequencies: 19.35, 22.235, 37.0, and 85.5 GHz. All were dual-polarized, except for 22.235 GHz which only had vertical polarization. The addition of the 85.5 GHz channel allowed rainfall over land to

be accurately measured, due to the strong scattering signal at the high frequency compared to the low frequencies. The additional channels of SSM/I relative to ESMR allowed more advanced rain retrieval algorithms to be developed involving various combinations of microwave channels [23]. The SSM/I instruments were used to measure precipitation with great success (e.g. [24]), but one drawback was the lack of data for the diurnal cycle of precipitation. The SSM/I instruments, as well as the radiometers launched prior to SSM/I, were flown in sun-synchronous orbits. This type of orbit only gives observations at two local times, which is not sufficient to monitor the diurnal cycle of precipitation. The radiometers were flown in orbits with different equatorial local time crossings to aid in sampling the diurnal cycle, but the separation in local time crossings was at most three hours between the platforms. This was determined to not be sufficient to accurately monitor the diurnal cycle of precipitation [25]. Furthermore, combining measurements from two or more SSM/Is required either assuming the calibrations were identical or inter-calibrating the instruments. One way to resolve these two problems is to use one instrument placed in a non-sun-synchronous orbit, which allows measurements at all local times to measure the entire diurnal cycle.

1.2.5 The Tropical Rainfall Measuring Mission

The first satellite dedicated to the measurement of precipitation was TRMM, launched in November 1997 [26]. The two main instruments onboard are the TRMM Microwave Imager (TMI) and the Precipitation Radar (PR). TMI is a conical scanning microwave radiometer with frequencies centered at 10.65, 19.35, 21.3, 37, and 85.5 GHz. All frequencies have vertical and horizontal polarization except 21.3 GHz, which only has vertical polarization. The design of TMI is similar to SSM/I, with the addition of the

10.65 GHz channels to be sensitive to heavier rain rates. The PR operates at 13.8 GHz and is used to measure the vertical profile of rain, helping to constrain the microwave radiometer retrieval algorithms. TRMM was placed in a non-sun-synchronous orbit with 35° inclination, giving a revisit time of about twice per day for those regions lying within approximately 40°S to 40°N. The orbit was chosen to observe the full diurnal cycle of rain, as well as to specifically observe the tropics which is where about two thirds of the global precipitation occurs [27].

TRMM had an original design lifetime of three to five years, yet after 16 years in orbit it is still in operation with both the TMI and PR on board working well. The satellite was originally launched into an orbit with an altitude of 350 km but was boosted to a new altitude of 402.5 km in August 2001. This was done to extend the lifetime of the mission, since the higher altitude allowed for less drag on the satellite and therefore less consumption of fuel. The result of boosting TRMM has provided an invaluable 16 year time period of precipitation measurements.

Three of TRMM's major accomplishments include the generation of a rainfall climatology [28], greater knowledge of the diurnal cycle of rain [29], and the first estimates of the relationship between precipitation and the profile of latent heating [30]. The rainfall climatology is made possible by the long lifetime of the TRMM satellite. Second, the diurnal cycle of rain is able to be measured since TRMM is in a non-sun-synchronous orbit. The spaceborne radiometers prior to TRMM with frequencies to measure rain were launched into sun-synchronous orbits which could only observe two local times. Finally, the latent heat measurements are made possible by measurements of

the vertical rain profiles using TMI and PR, as well as by improvements to cloud resolving models which are essential to the retrieval of profiles of latent heat [31].

Three major limitations of TRMM include lack of global coverage, inability to measure snowfall, and insufficient temporal resolution. First, the lack of global coverage is a result of TRMM's 35° orbital inclination, which gives observations limited only to the tropics. In order to obtain an understanding of the global water cycle, this latitude range needs to be extended. Second, TRMM was not designed to measure precipitation in the form of snow which was acceptable since the satellite only views the tropics. However, in order to observe the global water cycle, which contains precipitation in the form of snow as well as rain, the instrument should also be able to measure falling snow. Finally, TRMM has the limitation of insufficient temporal resolution since it has a revisit time of only twice per day.

Since TRMM has the limitations of insufficient temporal and spatial coverage, several studies have been done to help improve these limitations by combining TRMM retrieved rain with rain measurements from IR instruments and rain gauges [32],[33] as well as combining TMI measurements with other microwave radiometer measurements, e.g. SSM/I [34],[35]. The inclusion of IR and rain gauges helped in extending the spatial coverage of TRMM rain measurements, but this method was still prone to large errors in regions where TRMM observations were not available and assumptions had to be made about the rain using just the IR or gauge measurements. Using TMI along with measurements from other microwave radiometers to give better spatial and temporal coverage showed promise, but this required inter-calibrating the radiometers in order to properly combine the measurements.

1.2.6 The Global Precipitation Measurement Mission

The GPM mission was developed to extend rainfall measurements beyond the TRMM mission lifetime and also to expand the capabilities of current measurements by obtaining precipitation on a global scale with greater revisit times [36]. A microwave radiometer on a single satellite is unable to fulfill these goals by itself, so the only way to increase the latitudinal coverage as well as revisit times using microwave radiometers in LEO is to use several radiometers on individual satellites in different orbits. The concept of GPM is to use a constellation of microwave radiometers on various satellite platforms to achieve global coverage and a revisit time of approximately three hours.

GPM consists of a constellation of microwave radiometers built by many different manufacturers, some of which are already on-orbit and others to be launched within the next few years. The main satellite in the GPM constellation is called the GPM Core, set to be launched in February 2014. The satellite will be launched into a non-sun-synchronous orbit at 407 km with a 65° inclination angle. GPM Core has instruments onboard similar to the TMI and PR but with additional frequencies and improved calibration. The GPM Microwave Imager (GMI) on the Core has frequencies centered at 10.65, 18.7, 23.8, 36.5, 89.0, 165.5, 183.31±3, and 183.31±7 GHz. All frequencies are dual-polarized except for the 23.8 and 183.31 GHz channels which only have vertical polarization [37]. The instrument similar to TRMM's PR is the Dual-frequency Precipitation Radar (DPR) which includes two frequencies: 13.6 GHz, similar to TRMM's PR, and 35.5 GHz, which was added to have increased sensitivity to light rain [38].

The three limitations identified with TRMM are improved by specific design characteristics of GPM. First, the latitudinal coverage of TRMM is increased by GPM Core's higher inclination orbit, in addition to the global coverage provided by the sun-synchronous orbiters in the GPM constellation. Second, GPM will be able to measure both liquid and frozen precipitation with the inclusion of the 165.5 GHz and 183.31 channels on GMI since these frequencies have been shown to be sensitive to falling snow [39]. Finally, the temporal resolution of TRMM is improved by the constellation of satellites in GPM that will, when combined together, give observations roughly every three hours, improving the revisit time of TRMM by a factor of four.

In order to achieve consistent precipitation measurements among the constellation of radiometers, the TB measurements from the radiometers all need to be closely matched. However, the calibration quality of TBs from different radiometers is usually not the same as a result of individual instrument design and calibration. Inter-calibration of the radiometers is necessary to make the TB measurements among the sensors agree. Inter-calibration accounts for design differences among the radiometers and calculates a TB offset and/or scale correction that is a result of differences in the radiometer absolute calibrations. The next section will describe how the on-board calibration of an individual radiometer is performed and give methods to externally calibrate radiometers. These methods can be used for inter-calibration.

1.3 Microwave Radiometer Calibration

Spaceborne microwave radiometers are instruments designed to measure the microwave radiation emitted from the Earth's atmosphere and surface. The basic design of a radiometer consists of an antenna to receive the incoming radiation, a front end to filter and amplify the signal to an acceptable power level, and a back end that detects and records the signal. Calibration of the radiometer is a necessary and very important aspect of the radiometer system so that accurate radiometric measurements can be made. Calibration of the radiometer involves a two-step process: (1) convert the raw voltage counts into antenna temperatures (TAs) [40] and (2) convert the antenna temperatures into brightness temperatures that can then be used for scientific purposes [41]. The TAs are representative of the signal that is received at the antenna from all directions, weighted by the antenna's directional sensitivity. The desired part of the signal used for science purposes is the TB, which is the part of the antenna temperature only within the antenna's main beam. An antenna pattern correction (APC) algorithm attempts to correct for and remove those parts of the signal that are not contained within the main beam and to correct for the diminished sensitivity to the signal in the main beam in order to derive the TB. The APC inverts the following expression in order to get the TB in the desired direction

$$T_A = \int_{4\pi} T_B(\theta, \phi) G(\theta, \phi) d\Omega \tag{1.9}$$

where θ is the elevation angle, ϕ is the azimuthal angle, and G is the gain of the antenna.

1.3.1 On-Board Calibration

The first calibration step, to convert raw counts into TAs, is typically done by measuring an extreme cold and warm reference to characterize how the radiometer performs over all

possible temperatures. This is done to ensure that thermal variations in the instrument are accounted for. These reference temperatures need to be well known and stable in order to create a trustworthy calibration reference and frequent calibration of the radiometer is important to ensure that the measurements are stable over time. The first mechanical conically scanning microwave radiometer, SMMR, used an antenna system that allowed for frequent hot and cold calibration [40]. The antenna scanned over the Earth scene, and when it was not viewing the Earth a switch was used to view a cold reference calibration scene and then a warm calibration target. The cold scene was a horn pointed at the cold sky and the warm target was a termination at ambient temperature. SSM/I improved upon this concept by using warm and cold calibration targets that were viewed directly through the feed horns [22]. Microwave conical scanners today still follow this basic design. The antenna system consists of feed horns sitting in a tray which is illuminated by an offset parabolic dish. As the radiometer scans, the feed horns are first illuminated by the Earth through the antenna dish and then by the two reference points, so that on every scan there is a warm and cold calibration performed. A cold reference is achieved by using a reflector that reflects the cold sky (~2.7 K) into the feed horns and the warm reference is accomplished with a high emissivity target at a stable warm temperature (~300 K). Before launch, the behavior of the radiometer is well characterized at brightness temperatures from about 100 K to 300 K and from this a calibration curve is developed that relates the raw counts recorded by the radiometer to the TAs. Using the on-board calibration targets along with this known calibration curve allows the raw counts to be converted into TAs which then get converted into TBs through the APC.

1.3.2 External Calibration

In addition to on-board calibration, external observations can be used as references to determine calibration errors that lie outside the on-board calibration loop or errors in the on-board calibration references themselves. Four methods that use external observations for radiometer calibration are: (1) averaging over-ocean observations for a long period of time to find scan biases; (2) comparisons with other radiometers using co-located observations; (3) deep space maneuvers; and (4) vicarious calibration using a reference statistic as a virtual 'target'. These methods have been performed on SSM/I [22], TMI [42], the Advanced Microwave Scanning Radiometer (AMSR-E) [43], and WindSat [44]. (1) is a straightforward method to implement; however, it requires averages of the TBs over several months to minimize the sensitivity to geophysical effects and thus washes out time-dependent calibration errors. (2) can be an effective method but it requires that cross-over locations between two radiometers exist and that there is a sufficiently large population of co-located observations. (3) is a very useful method where the spacecraft is rolled or pitched over so that the radiometer views cold space, creating a very stable cold background against which to calibrate. However, a drawback is that the radiometer will experience changes in its thermal environment during the cold space maneuver that can alter (sometimes appreciably) the physical temperature of calibration-related hardware, thereby potentially altering characteristics of the calibration errors being investigated. In addition, not every platform is able to undergo this maneuver so this method cannot be relied upon for every spaceborne radiometer. (4) is a method that relies on deriving a stable statistic of the Earth TB to be used as an external reference point. This is referred to as 'vicarious' calibration since the external reference can serve as a calibration point

instead of the on-board calibration. Three advantages of vicarious calibration are: it has the ability to be applied to a shorter time period of data than averaging over-ocean observations, it does not require cross-over locations between radiometers, and it is not dependent on a spacecraft maneuver. There are two methods of vicarious calibration described here: vicarious cold calibration, which finds a stable cold reference point using cold over-ocean TBs [45], and vicarious warm calibration, which finds a stable warm reference point by using de-polarized regions in the Amazon [46].

1.3.3 Vicarious Cold Calibration

Vicarious cold calibration relies on the fact that the coldest stable TBs a microwave radiometer observes are over the ocean with calm surface winds, no clouds, and minimal water vapor. For every frequency, polarization, and EIA there is a sea surface temperature (SST) at which the TB is at a minimum. Figure 1.4 shows the dependence of TB on SST at various microwave frequencies typical of microwave imagers used for atmospheric remote sensing. Both vertical polarization (V-pol) and horizontal polarization (H-pol) are shown. The upwelling TB at the surface is equal to the product of the emissivity and physical temperature of the ocean, but the relationship between TB and SST is not linear because emissivity is also a function of SST. The emissivity is a function of EIA as well as the dielectric constants of the air and water. Air has a dielectric constant of 1 while water has a higher dielectric constant at microwave frequencies, resulting in a partial reflection at the air/water interface and a corresponding emissivity that is less than 1. As SST increases, the water molecules vibrate more and are able to align with an applied electric field more easily, resulting in a higher dielectric constant. This in turn increases the contrast between the air and water dielectric constants and

further lowers the emissivity, which causes the decrease in TB with SST even though SST is increasing. The decrease in emissivity with respect to SST is not constant, however, and at some point the increase in SST dominates the decrease in emissivity, causing the minimum in the TB and then the increase in TB with respect to SST.

Figure 1.4 is created using the RTM outlined in (1.5)-(1.8) and Figure 1.2. The atmosphere is a U.S. standard atmosphere with the surface water vapor set equal to zero (i.e. no atmospheric water vapor present) and no cloud liquid water. Water vapor is set to zero so that the TOA TB is most heavily influenced by the surface emissivity, which is a function of frequency, EIA, SST, wind speed, and sea surface salinity (SSS). The surface conditions are set with a wind speed of 0 m/s and an SSS of 34 ppt. The EIA is a constant 53° so the emissivity is therefore only a function of frequency and SST.

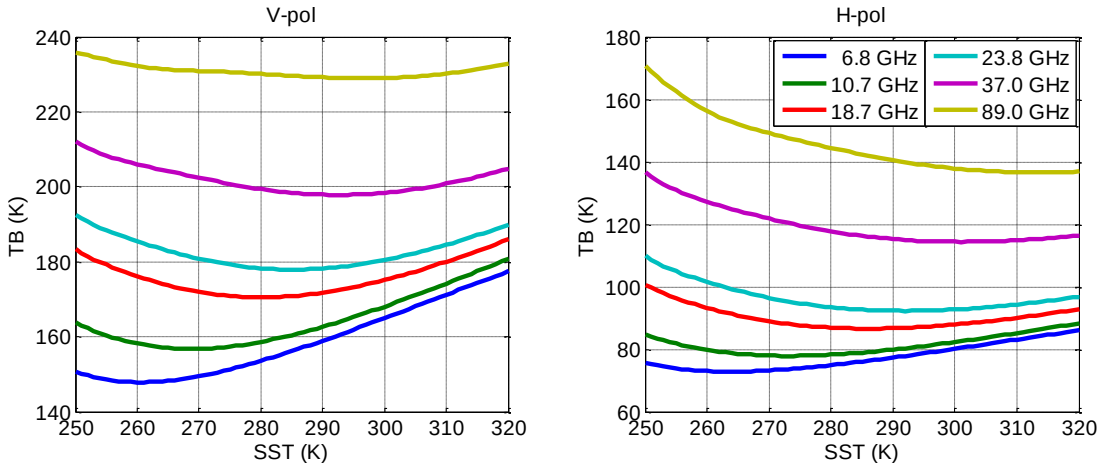

Figure 1.4: TB vs. SST for a clear sky, calm ocean scene at various V-pol (left) and H-pol (right) frequencies typical of microwave imagers at an EIA of 53°.

For some frequencies/polarizations, the minimum TB occurs at an SST value that is below the freezing point of seawater (approx. 271 K). This means that the theoretical minimum TB will not be observed since liquid seawater does not exist at those

temperatures, and frozen seawater has different emissivity properties that cause the TB to no longer be the coldest observed. The impact of this will be discussed in greater detail in Section 2.1.1.

The vicarious cold calibration algorithm is used to find a cold reference TB, referred to as the 'cold cal TB'. This value is derived from histograms of the TB data from over-ocean scenes. A sample histogram of TB data at 18.7 GHz V-pol is shown in Figure 1.5, with the top plot the histogram for all data and the bottom plot just the lower 20 K of the histogram. One month of TB data is binned with a resolution of 0.1 K after the data are filtered for land and sea ice so that only over-ocean data are included. There is a lower bound to the histogram, from which the cold cal TB is derived. Details on how the cold cal TB is calculated are given in Chapter 2.

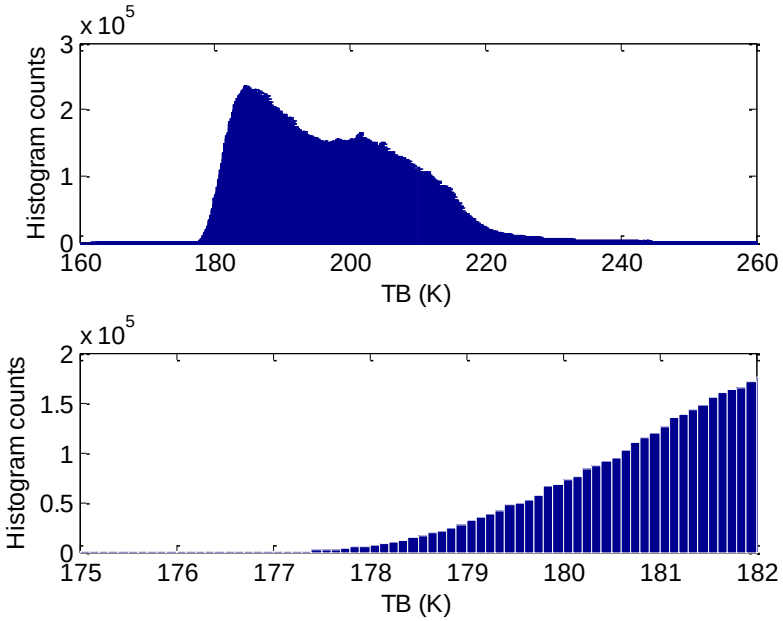

Figure 1.5: Sample TB histogram at 18.7 GHz V-pol for the entire range of over-ocean TBs (top) and just the cold end of the histogram (bottom).

1.3.4 Vicarious Warm Calibration

Vicarious warm calibration uses regions of the Amazon rainforest that are depolarized at microwave frequencies. This means that the regions are near blackbodies with emissivities very close to 1. This does not necessarily mean that these regions produce the warmest TBs observed on Earth. In fact, these TBs are usually about 30 K less than the warmest TBs on Earth. However, the fact that the regions are near blackbodies means that they create a stable and easily modeled reference. Figures 1.6 and 1.7 give examples where depolarized regions in the microwave exist on the globe. The data are from the SSM/I 37 GHz channel. The figures show $|TB_{37V} - TB_{37H}|$, where the green colors indicate the degree of depolarization with the darkest green indicating nearly depolarized regions ($|TB_{37V}-TB_{37H}|$ extremely close to zero). The white areas are regions where $|TB_{37V}-TB_{37H}| > 5$ K and are considered to not be sufficiently depolarized for warm calibration analysis. The best regions to use for warm calibration are in the heavily vegetated rainforests of South America and in Africa. Other areas, such as Indonesia, also show depolarization, but it is desirable to choose large regions in order to have a larger area of usable data that can completely contain the radiometer footprint and near-in sidelobes.

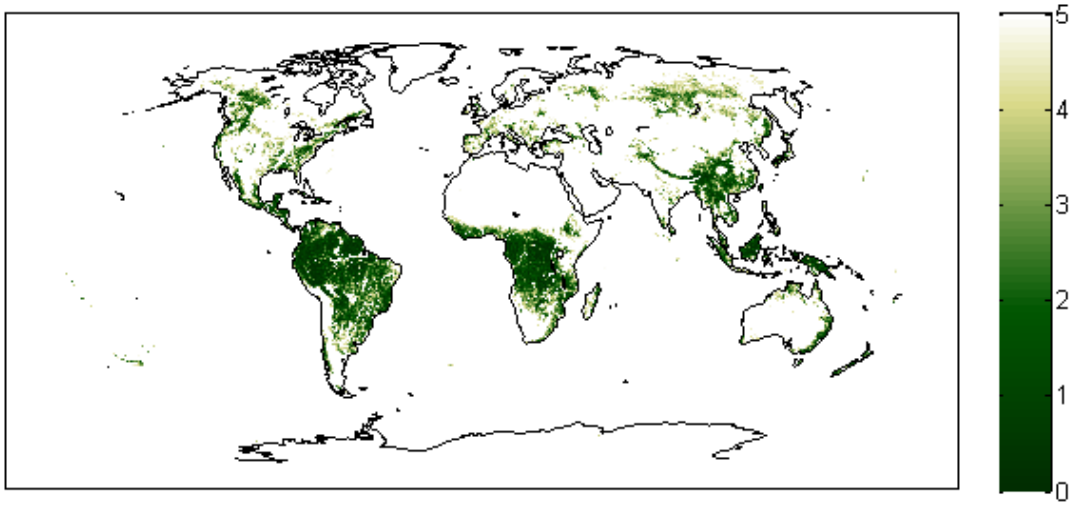

Figure 1.6: SSM/I $|TB_{37V}-TB_{37H}|$. Green colors indicate regions of depolarization, with the darkest green indicating the greatest depolarized regions ($|TB_{37V}-TB_{37H}| = 0$).

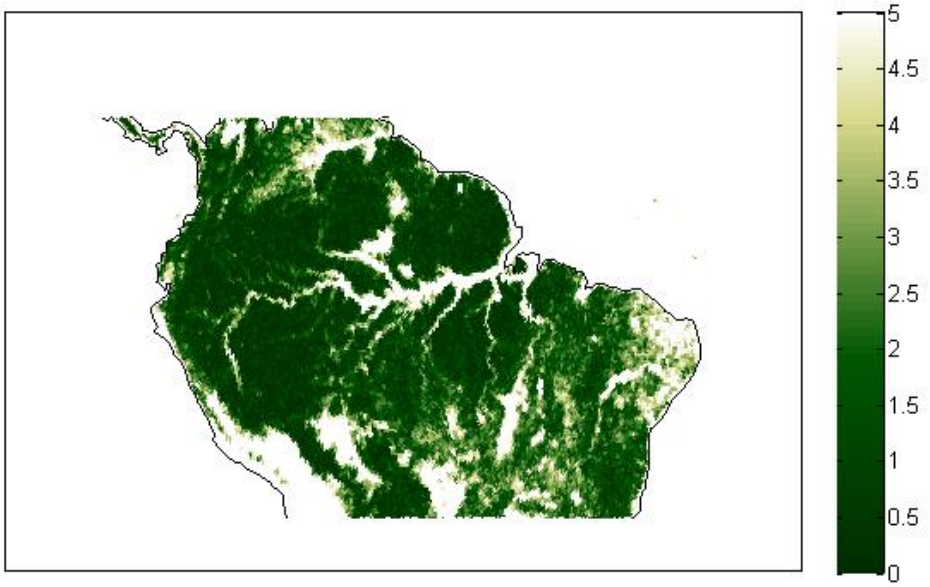

Figure 1.7: SSM/I $|TB_{37V}-TB_{37H}|$ over South America. Green colors indicate regions of depolarization, with the darkest green indicating the greatest depolarized regions ($|TB_{37V}-TB_{37H}| = 0$).

1.3.5 Inter-Calibration

Two of the external calibration methods can be used to derive calibration offsets between two or more radiometers, thereby inter-calibrating the sensors. Specifically, they are: (1) finding cross-over points between radiometers; and (2) deriving a stable reference

statistic with vicarious calibration. Inter-calibration is necessary since the absolute calibration of radiometers cannot be assumed to be the same; additionally, the design of most radiometers is not identical. A robust inter-calibration accounts for design differences and derives a calibration offset that is a result of differences in the individual on-board calibrations.

1.4 Structure of Thesis

This thesis describes the development and application of an inter-calibration algorithm using vicarious cold calibration. This algorithm has been developed for use with the GPM mission but can also be used for inter-calibrating other spaceborne microwave radiometers.

Chapter 2 describes details of the vicarious cold calibration algorithm and how it is used to derive a stable cold reference point, referred to as the 'cold cal TB'. The cold cal TB is calculated for frequencies from 10 to 37 GHz, and the sensitivity of the cold cal TB to geophysical effects as well as instrument characteristics, such as EIA and orbit, is presented. Challenges with extending vicarious cold calibration to higher frequencies around 90 GHz are identified and left to be examined in Chapter 3.

Chapter 3 introduces the single difference as a tool to account for the sensitivities of the cold cal TB to geophysical and instrumental effects. The single difference uses simulated TBs from an RTM to model what the radiometer observes to account for geophysical effects and the EIA, frequency, and viewing time of the radiometer. The single differences are calculated using radiometer data for 10 to 37 GHz and shown to greatly reduce seasonal variability in the cold cal TB. Next, the challenges associated with extending vicarious cold calibration to frequencies around 90 GHz are revisited and the single difference is shown to be able to mitigate these challenges. Finally, the single difference is shown to be useful in calculating the attitude (pitch and roll) offsets of a satellite using the microwave radiometer on-board.

Chapter 4 describes the inter-calibration algorithm that uses the cold cal TB with the single difference to calculate a cold-end calibration offset between two radiometers.

Inter-calibration offsets between two radiometers are calculated for frequencies from 10 to 90 GHz, using a sun-synchronous orbiter and a low inclination, non-sun-synchronous orbiter. Challenges with inter-calibrating two radiometers in orbits with different local viewing times are identified and shown whether they have an impact on the inter-calibration.

Chapter 5 assesses the impact of inter-calibration on rain accumulation using two rain retrieval algorithms that will be used for GPM. Using the TMI and SSM/I instruments as examples, rain accumulations are calculated first using the TBs from each radiometer's absolute calibration, and then the rain accumulations are calculated after the radiometers have been inter-calibrated. It is shown that inter-calibration has a positive impact on improving the consistency in retrieved rain from TMI and SSM/I, confirming that inter-calibration is a necessary aspect of the GPM mission, as well as any study that seeks to combine measurements from various radiometers into a cohesive data set.

Chapter 6 summarizes the work in the thesis and presents future research to be done.

Chapter 2
Vicarious Cold Calibration: Application to Microwave Radiometers

2.1 Introduction

2.1.1 Vicarious Cold Calibration Theory

Vicarious cold calibration uses histograms of TB data from over-ocean scenes to derive a stable cold reference TB, referred to as the 'cold cal TB'. The cold cal TB is derived from the lower bound on the total TB histogram. This lower bound only includes those TBs with minimal atmospheric water vapor and little to no wind. It is not practical to simply take the minimum TB of a given set of observations since this may not be a stable value. This section will describe how the cold cal TB is calculated as well as some of its properties.

The SSTs that produce the coldest TBs vary as a function of both frequency and polarization, as seen in Figure 1.4. This implies that the cold cal TB should be associated with specific regions on the globe where these SSTs occur. Figures 2.1 and 2.2 give examples of the regions where the SSTs occur that produce the coldest TBs for 19 GHz V-pol (19V) and 37 GHz H-pol (37H), respectively. These maps are created using SSTs from the Global Data Assimilation System (GDAS) [47] averaged over one month (January 2006). The colors indicate SSTs that are within +/- 5 K of the SST that produces the theoretical minimum TB, which is 280 K for 19V and 301 K for 37H. The grey areas are land and sea ice.

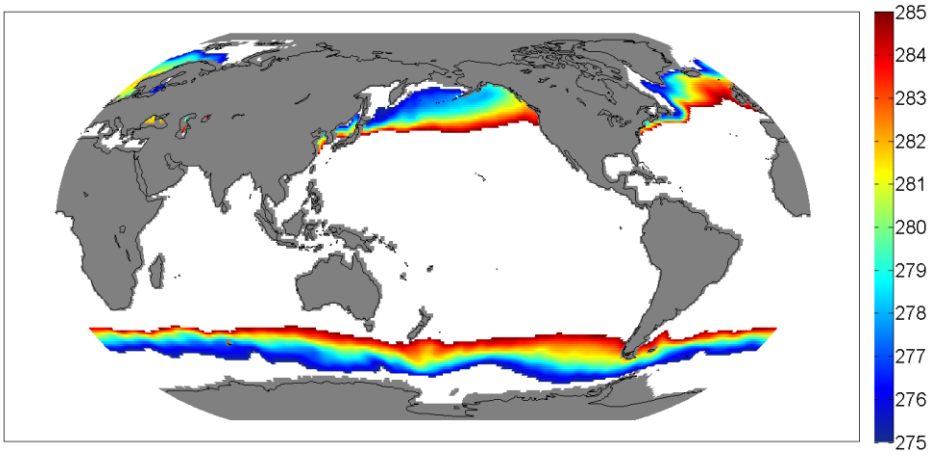

Figure 2.1: Regions of SSTs associated with the coldest TBs for 19 GHz V-pol. The colors indicate the SSTs within +/- 5 K of 280 K, where the theoretical minimum TB for 19V occurs.

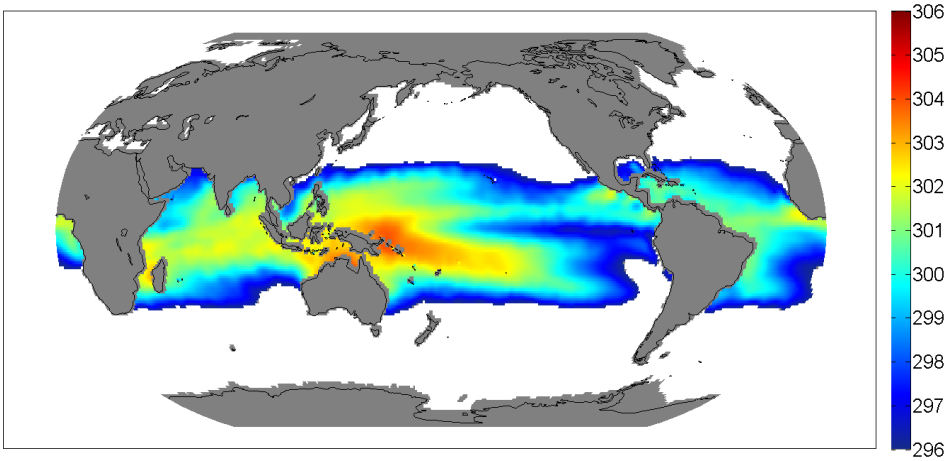

Figure 2.2: Regions of SSTs associated with the coldest TBs for 37 GHz H-pol. The colors indicate the SSTs within +/- 5 K of 301 K, where the theoretical minimum TB for 37H occurs.

These channels each present different challenges for deriving the cold cal TB. 37H appears to have a large region from which the coldest TBs are produced. However, this region has high concentrations of water vapor. Water vapor increases the TOA TB, therefore the coldest TBs that are actually observed will happen closer to the poles where the water vapor content is not as high even though the SSTs there may not be what produces the theoretically coldest TBs. In contrast, the 19V SSTs exist in regions where water vapor is at a minimum. However, these latitudes are higher than what a radiometer

in a low inclination orbit, such as TMI, would see. Since TMI is not able to observe the regions where the theoretical coldest TBs occur, it will derive a cold cal TB from the TBs closer to the equator which may not be as stable since it will now depend more on the exact latitude coverage of the sensor.

The regions that produce the coldest observed TBs for these two channels can be identified by analyzing a radiometer's observed TBs. Figures 2.3 and 2.4 show the areas where the coldest observed TBs occur for the Advanced Microwave Scanning Radiometer (AMSR-E) 18.7 GHz V-pol (18.7V) and 36.5 GHz H-pol (36.5H), respectively. Each black point on the map represents a TB that falls in the coldest 10% of TBs from the total histogram for one month of radiometer data. The SST regions that produce the theoretically coldest TBs for each channel are also shown on the maps for comparison. The 18.7V observed TBs all fall near these SST regions. The 36.5H observed TBs, on the other hand, lie mostly outside the SST region for that channel. This is due to the high concentration of water vapor around the equator, causing many of the coldest TBs for 36.5H to occur closer to the poles.

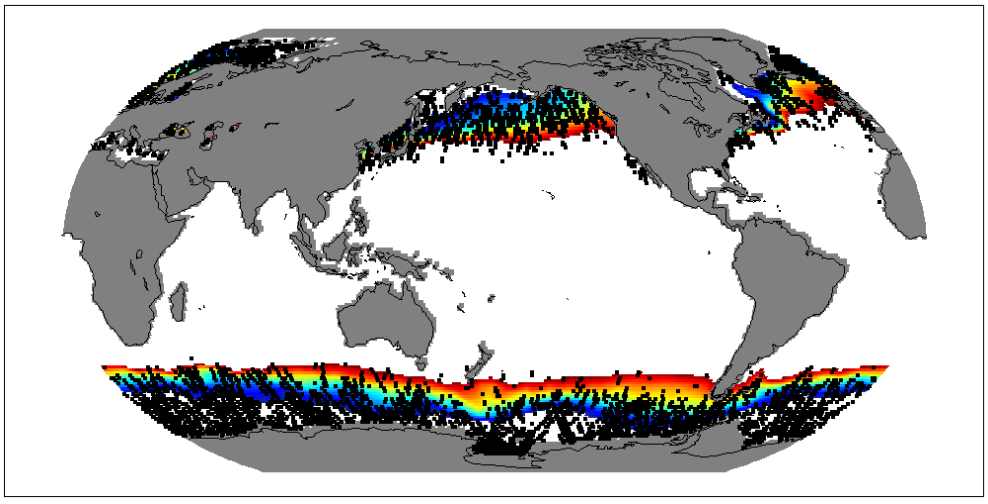

Figure 2.3: Occurrence of TBs from the lower 10% of the histogram for AMSR-E 18.7V, overlayed on the SST regions that produce the theoretically coldest TBs.

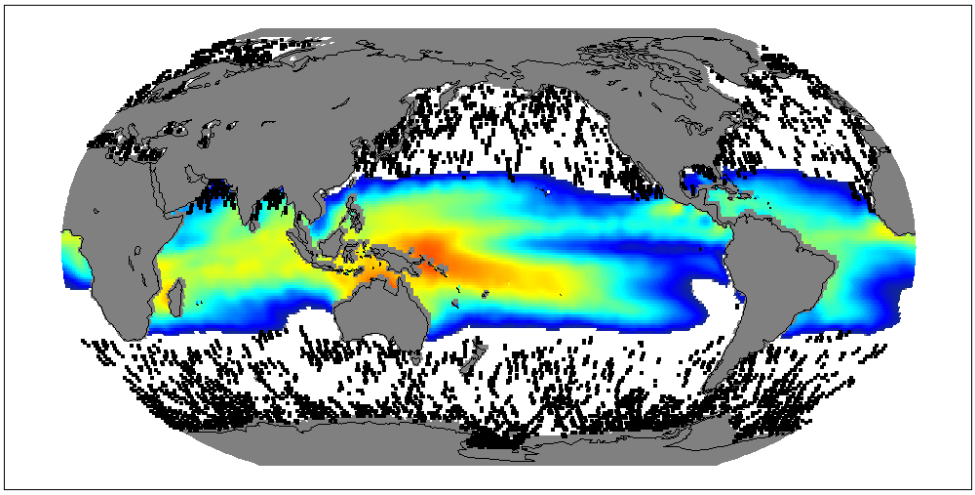

Figure 2.4: Occurrence of TBs from the lower 10% of the histogram for AMSR-E 36.5H, overlayed on the SST regions that produce the theoretically coldest TBs.

The other AMSR-E V-pol channels show similar behavior to 18.7V and the H-pol channels show similar behavior to 36.HV. The V-pol channels tend to have cold TBs that cluster close to the poles, while the H-pol channels have clusters close to the poles but also have points that are scattered closer to the equator, like 36.5H in Figure 2.4. This analysis shows that SST has a very minor impact on vicarious cold calibration. This implies that for some frequencies that have a theoretical minimum TB that occurs at an unphysical SST, such as 10V, the SST distribution is not critical in determining the cold cal TB. Instead, water vapor appears to play a much bigger role in determining the regions where the coldest TBs occur. Another geophysical factor that may affect the location of the coldest TBs is wind speed. To analyze what values of SST, water vapor, and wind speed contribute to the coldest TBs, histograms are created of these geophysical variables that are associated with the 10% coldest TBs. The geophysical variables are taken from GDAS, using the closest grid point in space and time to the radiometer observations.

Figures 2.5 – 2.7 show the geophysical variable histograms associated with the TBs from an entire month of data (Total histogram) along with the geophysical variable histogram associated with the coldest 10% TBs (10% CDF histogram). These figures give some important insights into the geophysical variables that impact vicarious cold calibration. First, Figure 2.5 confirms that SST plays a very minor role in determining the cold cal TB. The 10% CDF histograms show no bias towards the SST that produces the theoretically lowest TBs for the channels (SST of 280 K for 19V and 301 K for 37H). Second, Figure 2.6 confirms that the cold cal TB is derived from regions with minimal water vapor. The 19V and 37H channels do show a slight difference in the 10% CDF histogram. It appears that the 37H channel allows the water vapor to be slightly higher than for 19H. This can most likely be explained by Figure 2.7 that shows the wind speed histograms. 37H has a 10% CDF histogram with a mean wind speed that is slightly lower than 19V, most likely indicating that the 37H coldest TBs are allowed to have a little more water vapor in favor of having a lower wind speed.

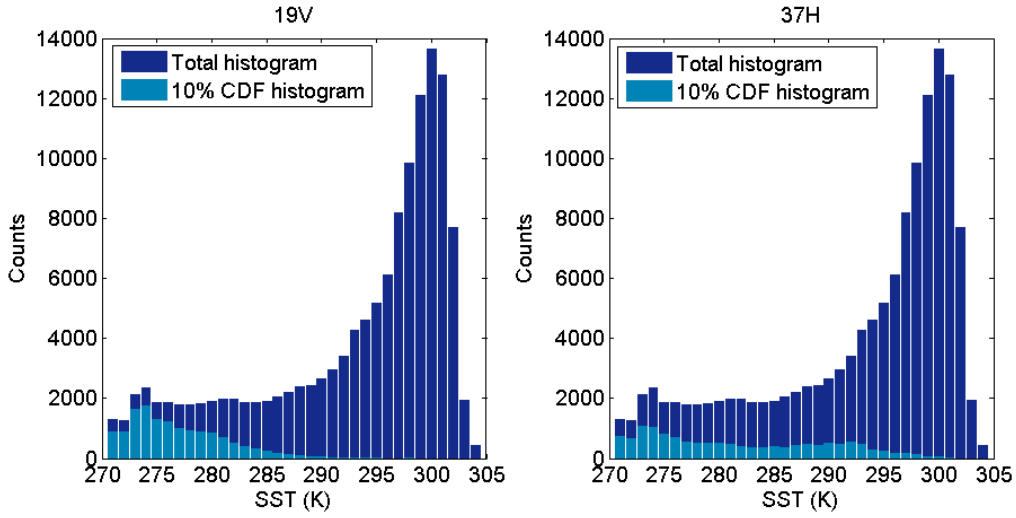

Figure 2.5: Histograms of SST for AMSR-E 18.7V (left) and 36.5H (right) associated with all the TB observations for January 2006 (Total histogram) and the SSTs associated with the TBs in the coldest 10% of the TB histogram CDF.

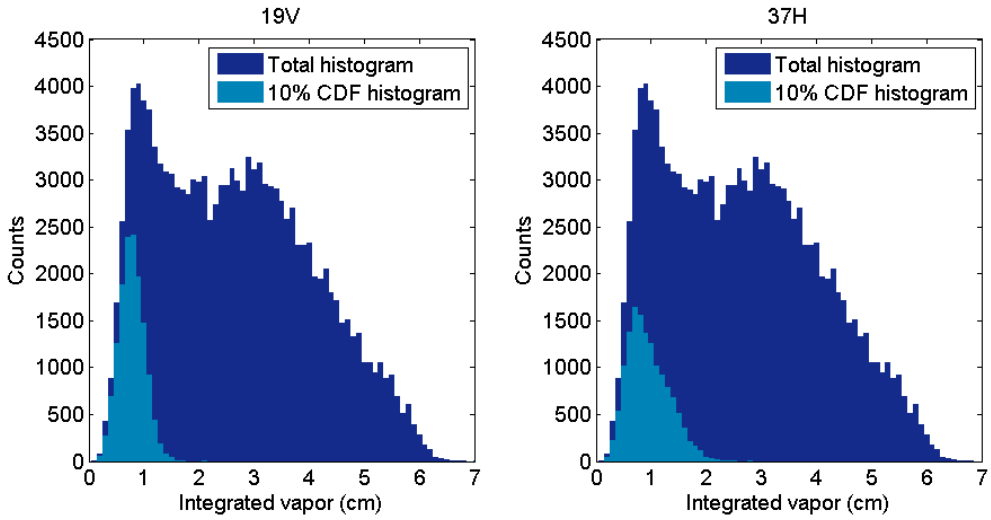

Figure 2.6: Histograms of integrated water vapor for AMSR-E 18.7V (left) and 36.5H (right) associated with all the TB observations for January 2006 (Total histogram) and the SSTs associated with the TBs in the coldest 10% of the TB histogram CDF.

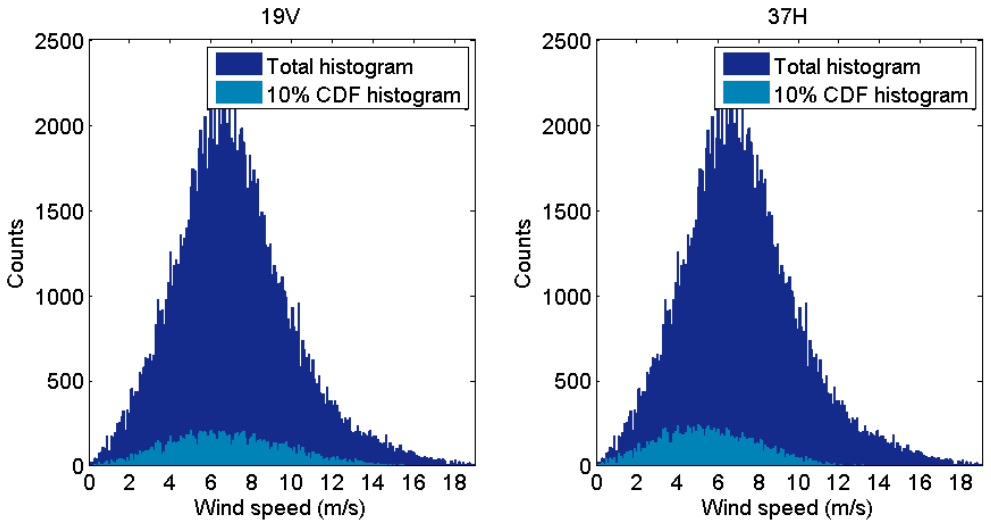

Figure 2.7: Histograms of wind speed for AMSR-E 18.7V (left) and 36.5H (right) associated with all the TB observations for January 2006 (Total histogram) and the SSTs associated with the TBs in the coldest 10% of the TB histogram CDF.

Table 2.1 gives the mean SST, water vapor, and wind speed values for the total histogram and the 10% CDF histogram for all AMSR-E channels. This shows that all V-pol and H-pol channels show similar results to the 18.7V and 36.5H histograms, respectively. The cold cal TB is derived from areas of minimal water vapor compared

with the total histogram. The wind speed for the coldest 10% TBs is less than the mean wind speed for the total histogram for H-pol, which indicates that the H-pol cold cal TB is more sensitive to changes in wind speed than V-pol.

		10.65V	**18.7V**	**23.8V**	**36.5V**	**89.0V**
SST (K)	Total mean	293.0	293.0	293.0	293.0	293.0
	10% mean	275.9	276.8	276.8	279.9	277.5
Water Vapor (cm)	Total mean	2.6	2.6	2.6	2.6	2.6
	10% mean	0.9	0.8	0.7	0.8	0.8
Wind Speed (m/s)	Total mean	7.1	7.1	7.1	7.1	7.1
	10% mean	6.6	6.9	7.5	8.0	8.5
		10.65H	**18.7H**		**36.5H**	**89.0H**
SST (K)	Total mean	293.0	293.0		293.0	293.0
	10% mean	279.8	278.5		281.8	278.4
Water Vapor (cm)	Total mean	2.6	2.6		2.6	2.6
	10% mean	1.0	0.8		0.9	0.8
Wind Speed (m/s)	Total mean	7.1	7.1		7.1	7.1
	10% mean	5.0	5.8		5.5	7.0

Table 2.1: Mean of the geophysical variables (SST, integrated water vapor, and wind speed) associated with the TBs for the total histogram and the 10% CDF histogram for AMSR-E channels.

2.1.2 Vicarious Cold Calibration Algorithm Details

The vicarious cold calibration algorithm was originally developed for a nadir viewing spaceborne radiometer at 19, 21, and 37 GHz [45]. However, the application here is for conical scanning radiometers that view at EIAs between 50 and 55 degrees. This difference in EIA, as well as the introduction of vertically and horizontally polarized TBs with a non-zero EIA, causes the TB histograms to be different. Therefore, the details of the algorithm may need to be modified to ensure that the most stable cold reference TB is being derived.

The value of the cold cal TB, as well as the shape of the histogram, varies considerably depending on whether the radiometer is viewing at nadir or an angle offset

from nadir. Figure 2.8 gives example histograms at 19 GHz for a spaceborne radiometer observing at nadir and an EIA of 53° for both V- and H-pol. The nadir-viewing radiometer displays the smallest range of TBs while the H-pol TB histogram has the highest range of TBs. Since the derivation of the cold cal TB is only dependent on the lower end of the histogram, the shape beyond the first initial increase of histogram counts with TB will not affect the cold cal TB. This initial increase in the histogram is due to ocean scenes with relatively small amounts of water vapor, and these are the TBs that are included in the cold cal TB derivation. These TBs are associated with regions close to the poles. The V-pol histogram has two peaks: the first is associated with cold TBs close to the poles, while the second peak is due to water vapor near the equator.

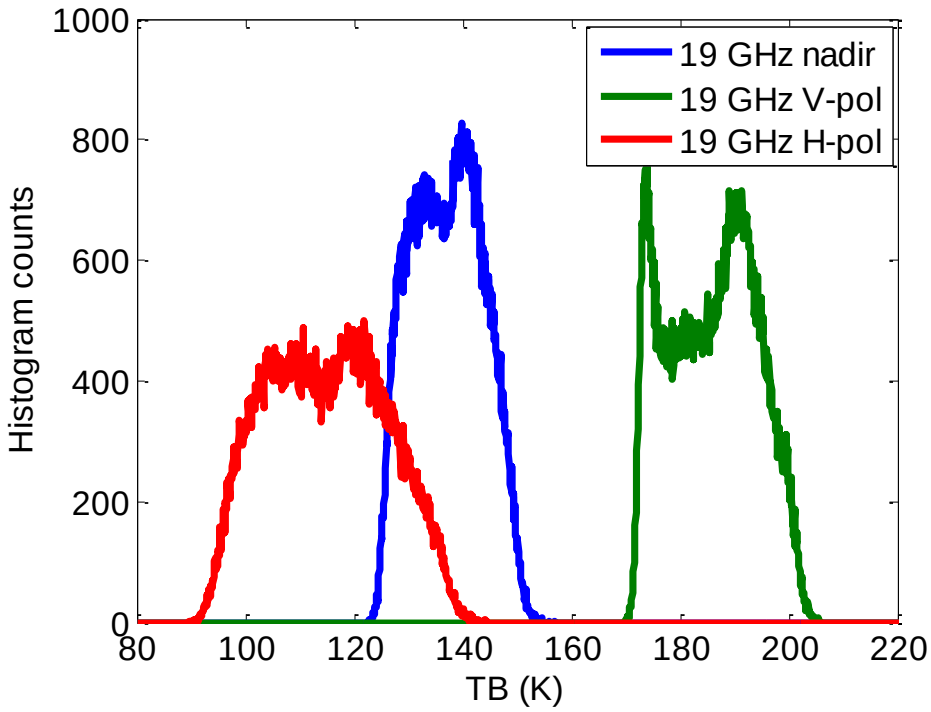

Figure 2.8: Example modeled TB histograms for 19 GHz viewing nadir (blue), 53° V-pol (green), and 53° H-pol (red).

The vicarious cold calibration algorithm for nadir-viewing radiometers uses a subset of the TB histogram at the coldest 20 K range. A 3rd degree polynomial is fit to the inverse cumulative distribution function (CDF) of the data between 3% and 10% of this 20 K range subset histogram. The polynomial is extrapolated down to 0%, and the TB value at this point is the cold cal TB [45]. The cold calibration algorithm was modified slightly for application to conically scanning microwave imagers. The CDF of the entire TB histogram is found and the CDF between 2% and 10% is used. A 2nd degree polynomial is fit to the inverse CDF of this portion of the total histogram and extrapolated down to 0%. The TB at the 0% CDF is called the 'cold cal TB'. Figure 2.9 gives a graphical description of this process. This algorithm gives a statistically derived cold TB point that is more stable than just taking the minimum value.

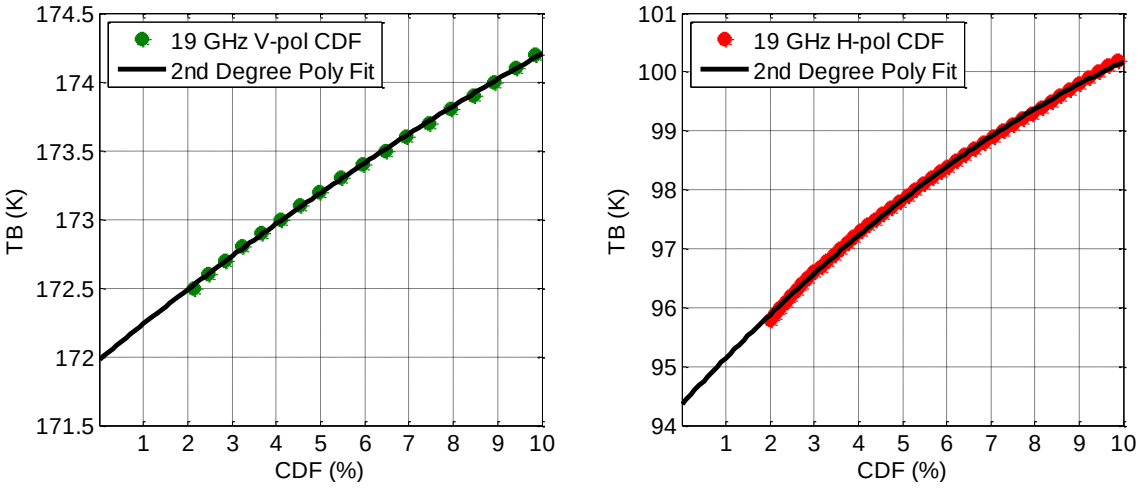

Figure 2.9: 2nd degree polynomial fit to the inverse CDF from 2% to 10% of the TB histogram for 19 GHz V-pol (left) and H-pol (right). The cold cal TB is the value of the 2nd degree polynomial at 0% CDF.

2.2 Vicarious Cold Cal TB for Microwave Imagers from 10 to 37 GHz

2.2.1 TB Histograms

The cold cal TB is computed from histograms of the TB population for a given time period and geographic region. The radiometer TB data are sampled by month, hemisphere (Northern and Southern), and orbit of the satellite (ascending and descending). Only data over ocean are used as inputs to the vicarious cold calibration algorithm so a land flag and sea-ice flag are used to filter the TBs. The quality flag given in the radiometer data is also used to filter the TBs. After filtering, the TBs are binned into histograms with dimensions of month, hemisphere, orbit, scan position, and channel. This is the total histogram that is input to the vicarious cold calibration algorithm. The vicarious cold calibration algorithm then derives the cold cal TB from this histogram based on the method described in Section 2.1.2. A cold cal TB is calculated for each dimension of the histogram, i.e. there is a cold cal TB value for each month, hemisphere, orbit, scan position, and channel.

To minimize the uncertainty in the cold cal TB caused by an insufficient data population size, the TBs from an entire month of radiometer data are used rather than from a shorter time period. Also, since the location of the cold cal TB can change seasonally as a result of water vapor fluctuations, the histograms are split into hemispheres to ensure that the coldest TBs are input to the algorithm while still giving a sufficient data population size.

2.2.2 Cold Cal TB Seasonal Variation

For purposes of evaluating instrument calibration biases, the presence of a seasonal cycle in the calibration is undesirable. The cold cal TB as shown in Section 2.1.1 is derived from regions with minimal water vapor and low wind speeds. The dominant source of geophysical variability in this TB population comes from water vapor. Water vapor in the atmosphere naturally varies throughout the year due to seasonal changes. While the cold calibration algorithm minimizes the impact of water vapor, it does not completely eliminate it. This shows up most readily on the water vapor channels of microwave radiometers.

One way to quantify the seasonal variation in the cold cal TB is to take the difference between the yearly maximum and minimum cold cal TB values, i.e. the amplitude of the seasonal cycle. The greater this difference, the greater the impact of natural geophysical variability on the calibration. The amplitude of the annual cycle provides a performance metric that characterizes an important property of a calibration method.

The annual cycle of the cold cal TB for AMSR-E 23.8 GHz V-pol is shown in Figure 2.10. Since this is the water vapor channel on AMSR-E, the cold cal TB should show the greatest sensitivity to atmospheric water vapor fluctuations compared to the other channels. The cold cal TB is sampled into three regions: the Northern Hemisphere (NH), the Southern Hemisphere (SH), and the globe (average of the NH and SH). Each point in the figure represents a cold cal TB value calculated using one month of TB data. The amplitudes of the seasonal cycle for the NH, the SH, and the global cold cal TB are 9.08 K, 1.85 K, and 4.36 K, respectively. The NH has a stronger water vapor seasonal

cycle compared to the SH, and water vapor is at its maximum in the summer and minimum during the winter [48]. This is reflected in the cold cal TB since the NH seasonal cycle of the cold cal TB is greater than the cold cal TB in the SH, and the maximum and minimum of the cold cal TB occur in the corresponding hemisphere's summer and winter, respectively.

In contrast, the AMSR-E 10.65 GHz V-pol channel has the least seasonal variation because the TB at that frequency is the least sensitive to atmospheric water vapor. Figure 2.11 shows 10.65 GHz V-pol for the same data sample as in Figure 2.10. There is still a small seasonal cycle that could be due to water vapor. The variation may also be a result of small SST variations since the TB at 10.65 GHz is more sensitive to SST than at higher frequencies. For this channel, the amplitudes for the NH, the SH, and the global cold cal TB seasonal cycle are 1.17 K, 0.65 K, and 0.69 K, respectively.

Table 2.2 gives the values of the seasonal cycle amplitude for the global cold cal TB for the AMSR-E channels. The amplitude appears to be largest for those channels nearest the water vapor line, indicating that the variation in the cold cal TB is most likely associated with seasonal water variability. This analysis shows that the cold cal TB by itself is not a useful calibration tool for these channels when monitoring the stability of an instrument's calibration over time.

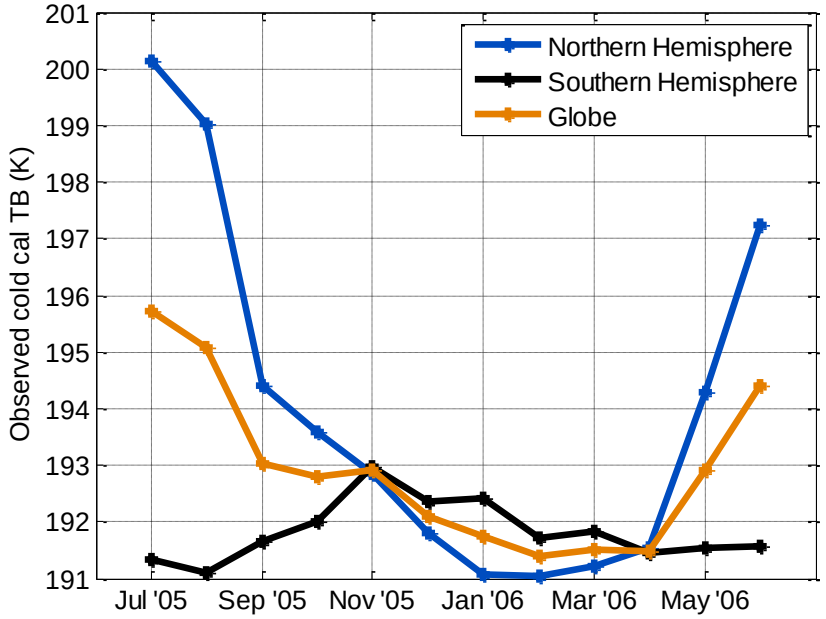

Figure 2.10: AMSR-E 23.8V GHz observed cold cal TB over a year for the globe, NH, and SH. The NH cold cal TB shows a strong seasonal cycle, which is attributed to the large variation in water vapor throughout the year.

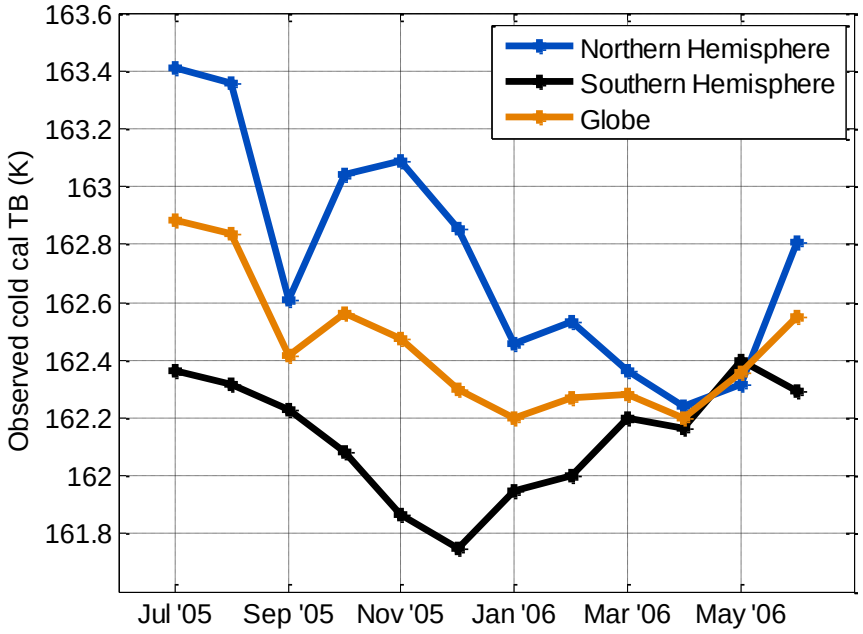

Figure 2.11: AMSR-E 10.65V GHz observed cold cal TB over a year for the globe, NH, and SH. This channel has a smaller seasonal cycle than 23.8 GHz since it is not as sensitive to atmospheric water vapor.

	10.65V	10.65H	18.7V	18.7H	23.8V	36.5V	36.5H
Seasonal Cycle Amplitude (K)	0.81	0.69	1.98	3.22	4.29	1.57	2.66

Table 2.2: AMSR-E seasonal cycle amplitudes for the global cold cal TB.

Since there is a noticeable seasonal cycle in the cold cal TB, one good analysis to do for this is to look where the coldest TBs occur regionally throughout the year. Similar to Figures 2.3 and 2.4, Figures 2.12 and 2.13 show the location of the coldest TBs, where each point on the map represents a TB that falls in the coldest 10% of TBs from the total histogram for one month of radiometer data using AMSR-E 18.7V. Figure 2.12 shows July 2005 and Figure 2.13 shows January 2006. The regions where the coldest TBs occur are largely determined by sea ice extent and water vapor. In July, the regions in the NH shift to the north where the sea ice has melted, while the SH regions have to shift north because of the sea ice. The opposite happens in January, and the months in between July and January show this trend happening. These figures show that the regions from where the cold cal TB is calculated changes throughout the year, which may account for some of the variation noticed in Figures 2.10 and 2.11.

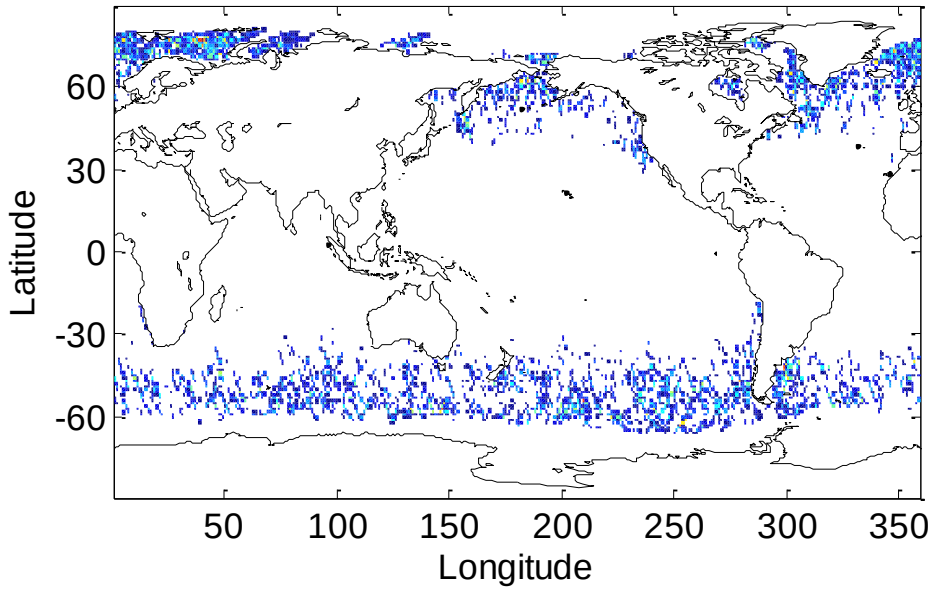

Figure 2.12: Occurrence of TBs from the lower 10% of the histogram for AMSR-E 18.7V for July 2005. The regions of the coldest TBs shift to the north in both the NH and SH due to sea ice extent.

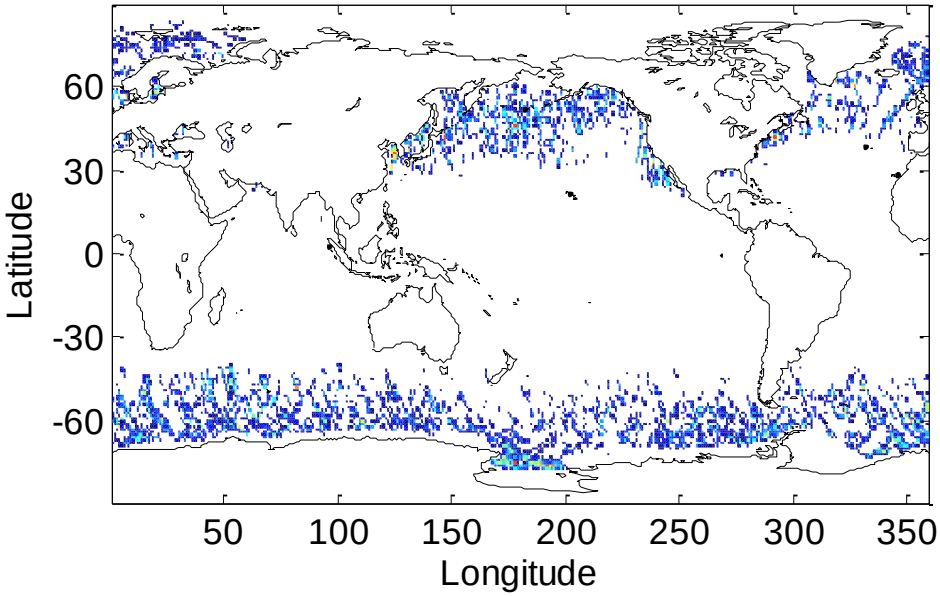

Figure 2.13: Occurrence of TBs from the lower 10% of the histogram for AMSR-E 18.7V for January 2006. The regions of the coldest TBs shift to the south in both the NH and SH due to sea ice extent.

2.2.3 Cold Cal TB EIA Variation

The cold cal TB is derived from regions with minimal atmospheric and surface wind speed contribution to the brightness. In these conditions, the TB is largely dominated by the surface signal which is a strong function of EIA over the ocean. Figure 2.14 shows the dependence of TB on EIA for V-pol and H-pol channels typical of microwave imagers. The TB is modeled using the same RTM as used in Figure 1.4. The dependence of TB on EIA is nearly linear, with V-pol having a positive slope and H-pol a negative slope. The dependence for V-pol is approximately 2.2 K per degree EIA while H-pol is approximately -1.1 K per degree EIA.

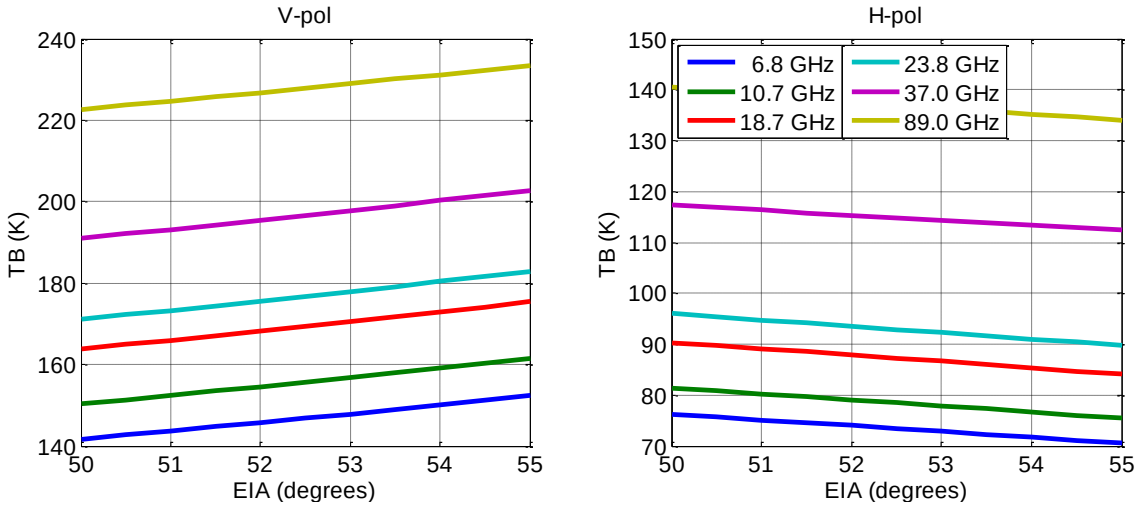

Figure 2.14: Dependence of TB on EIA for V-pol (left) and H-pol (right) channels.

Conical scanning microwave radiometers have a nominal EIA at which they view the Earth due to the fixed off-nadir angle of the reflector. However, the true EIA is not always equal to this nominal EIA. EIAs can vary across the scan if the conical scan axis of rotation is not aligned with the local vertical. This results from satellite attitude offsets in roll or pitch. The EIAs can also change throughout the orbit due to the oblateness of the Earth as well as eccentricity in the satellite orbit. Deviation from the nominal EIA

impacts the cold cal TB as seen in Figure 2.14, so it is important to be able to characterize this in the calibration.

Figure 2.15 gives the cold cal TB across the scan for AMSR-E 10.65 GHz V-pol. SH and NH descending orbits are shown to compare the cold cal TB for the different hemispheres. The 10.65 GHz frequency is chosen in order to have minimal TB contribution from the atmosphere and V-pol is selected to minimize the effect of surface roughness from wind. Also, the V-pol channels exhibit the greatest dependence of TB on EIA. Figure 2.16 is the corresponding EIA across the scan. The EIAs are given in the radiometer data for each scan position as well as for each scan line. The EIAs in this figure are those associated with the latitude regions that produce the coldest TBs, from approximately -50° to -70° for the SH and 50° to 70° for the NH. The cold cal TB variation across the scan for both SH descending and NH descending orbits show similar behavior as the EIA across the scan for the respective orbits. For example, the cold cal TB for the SH descending orbit varies by about 0.8 K across the scan. According to Figure 2.14, a change of 0.8 K in the cold cal TB should be accompanied by a change of approximately 0.36° in EIA. Figure 2.16 shows that the actual change in EIA is about 0.31°, very close to what is expected. This EIA dependence of the cold cal TB should be removed from the calibration so that it is not included as an error in the calibration when in fact it is instrumental in nature. The process of doing this is discussed in Section 3.2.

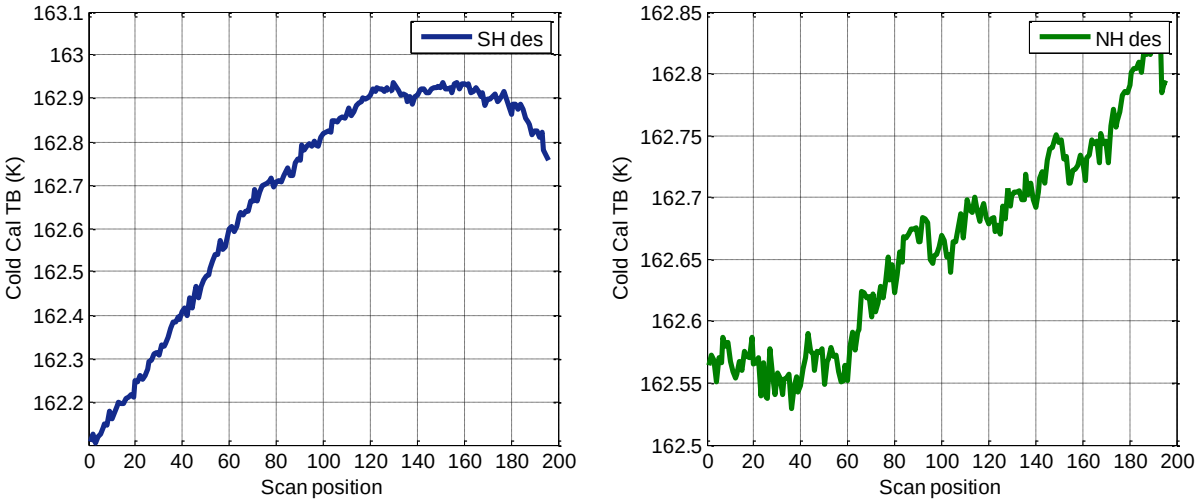

Figure 2.15: Cold cal TB across the scan for AMSR-E 10.65 GHz V-pol for SH descending (left) and NH descending (right) orbits

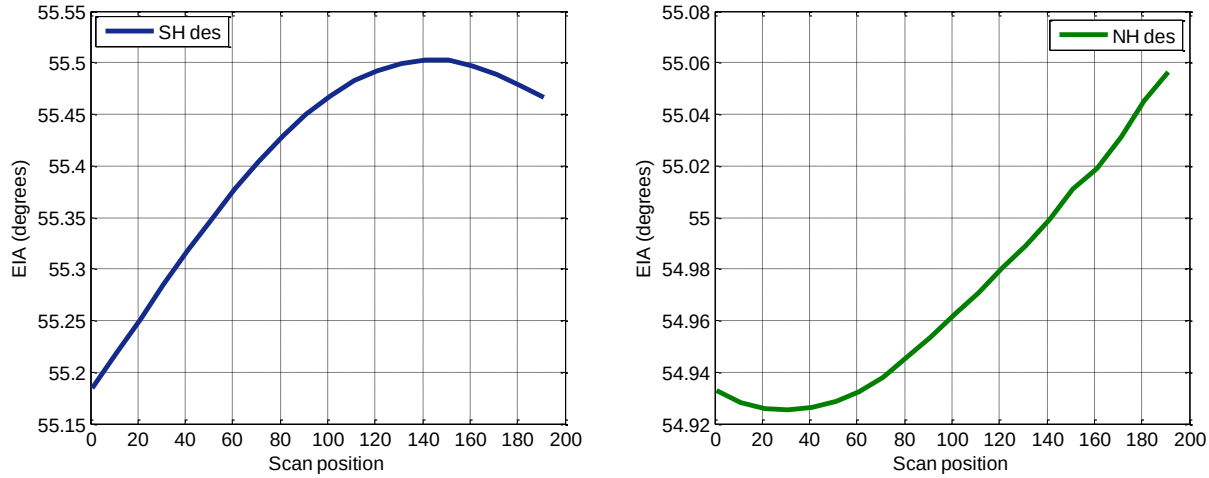

Figure 2.16: Scan dependent EIAs for AMSR-E SH descending (left) and NH descending (right) orbits. The EIA is the same for all low resolution AMSR-E frequencies and polarizations.

2.3 Extension of Vicarious Cold Calibration to Higher Frequencies

2.3.1 Challenges with High Frequency Range: 85 – 92 GHz

The vicarious cold calibration discussion has so far been limited to the frequency range 10 – 37 GHz, but many microwave imagers also include a high frequency channel in the range 85 – 92 GHz. Using vicarious cold calibration at 85 – 92 GHz introduces a few challenges that are not present at the lower frequencies. First, the theoretical SST at which the H-pol 90 GHz TB is at a minimum does not physically exist. According to Figure 1.4, this SST is approximately 314 K for H-pol. Since SSTs rarely exceed 310 K [49], the coldest TBs will not come from the SSTs around the theoretical 90 GHz H-pol minimum. Instead, the vicarious cold calibration statistic will use the coldest 90 GHz H-pol observations possible. However, according to the analysis in Section 2.1.1, the SST distribution was determined to not play a factor in finding regions where the cold TBs are produced, so the unphysical SST where the theoretical TB is at a minimum should not be a large concern here.

A second concern with vicarious cold calibration at the high frequencies is the sensitivity to water vapor. As noted previously, vicarious cold calibration minimizes the impact of atmospheric water vapor but does not completely eliminate it from the cold cal TB. This slightly affects the lower frequencies from 10 to 37 GHz, most noticeably for those channels around the water vapor absorption line. Since the higher frequencies around 90 GHz are more sensitive to water vapor (see Figure 1.3), the cold cal TB will also be more sensitive to the water vapor distribution in the sample population.

A final concern with calibrating the 90 GHz channel that needs to be addressed is the TB depression caused by hydrometeor scattering [50]-[53]. Over an ocean

background, the presence of water vapor serves to increase the TB through absorption. However, a decrease in the upwelling TB can occur through scattering. At 90 GHz, the scattering cross section of ice and liquid water is greater than at lower frequencies, which results in more scattering and a greater TB depression. In many cases, the TBs can be lower than the theoretical cold TB from the surface. Wilheit et al. [51] observed TBs as low as 140 K at 92 GHz V-pol that were associated with heavily precipitating regions and attributed them to scattering by ice lifted above the rain by convective updrafts. This TB is much lower than the coldest TBs produced from the ocean surface (about 230 K at 90V). If these cold TBs are included in vicarious cold calibration, the derived cold cal TB will not be associated with the cold surface TBs but instead with the highly variable ice content. This introduces further variability into the vicarious cold calibration statistic that needs to be removed.

2.3.2 Cold Cal TB at 89 GHz

Ideally, the TBs that make up the lower bound on the histograms are from cold ocean scenes with minimal atmospheric attenuation and calm winds. However, if the lower bound TBs are due to less stable conditions, e.g. hydrometeor scattering, it is difficult to derive a stable statistic since the scattering is highly variable. This is the case for the high frequency range of 85-92 GHz. Figure 2.17 shows a sample TB histogram for AMSR-E 89 GHz V-pol (top) alongside 10.65 GHz V-pol (bottom). The 89V TB histogram has a long cold tail due to hydrometeor scattering (see Section 3.3 for a more detailed discussion). Deriving a cold cal TB from this histogram would result in a cold cal TB that is dependent on the highly variable hydrometeor scattering and not the stable ocean background. In contrast, the 10.65V TB histogram has a sharp lower bound. Under

extreme conditions hydrometeor scattering can occur at 10.65 GHz, but the TB depression is not large enough to cause TBs to be as cold as those generated from the surface. Therefore, the TBs that make up the lower bound of the 10.65V histogram are attributed to the ocean surface.

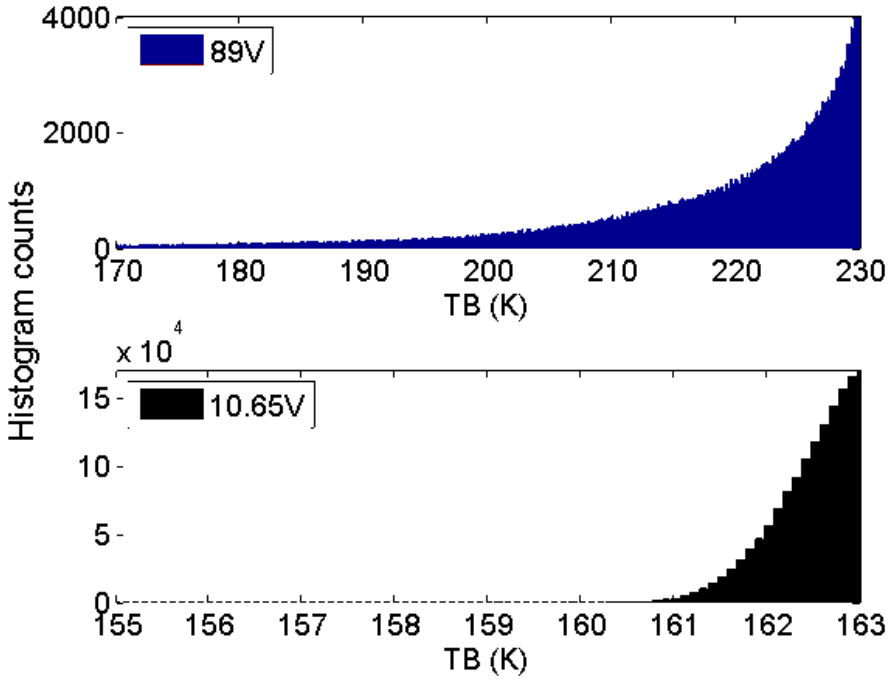

Figure 2.17: Comparison of AMSR-E 89 GHz V-pol TB histogram (top) with the 10.65 GHz V-pol TB histogram (bottom) for January 2006. The long cold tail present for 89V is due to hydrometeor scattering, while 10V has a much sharper lower bound and a restricted cold tail primarily due to additive noise. The long cold tail can destabilize the vicarious cold calibration statistic if not properly filtered.

Seasonal variation of the AMSR-E 89 V- and H-pol cold cal TB is illustrated in Figure 2.18, shown for the globe (average of NH and SH). The dataset used here is the same as in Figure 2.10. The 89V channel has small variations in the cold cal TB throughout the year, while the seasonal variation is very apparent at 89H. Note that the scales for V-pol and H-pol are different in order to highlight the seasonal variation for each polarization. A possible reason for the greater seasonal variability in the H-pol cold cal TB is that the relative contrast in TB between the atmosphere and surface is greater

for horizontally polarized TBs compared to vertically polarized TBs. Small changes in the atmospheric TB therefore have a greater effect on the overall TOA TB for H-pol, causing the cold cal TB at H-pol to be more sensitive to atmospheric variability.

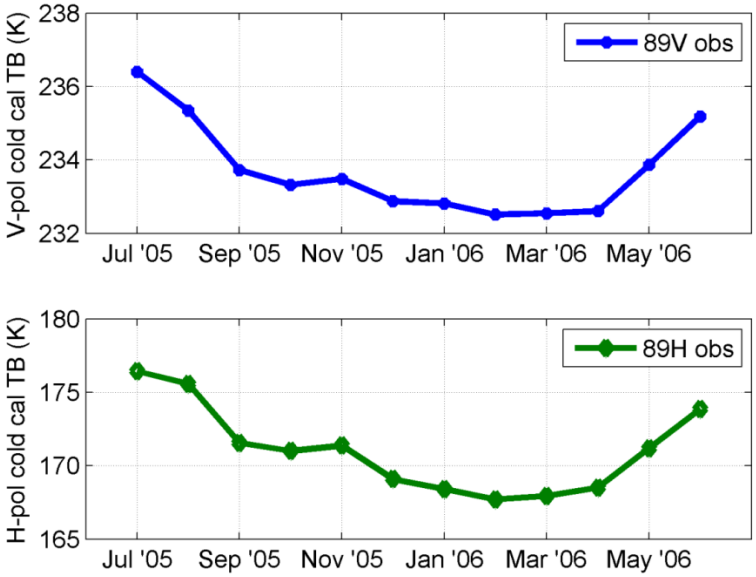

Figure 2.18: Cold cal TB for AMSR-E 89V (top) and 89H (bottom). A seasonal cycle in the cold cal TB is present for both polarizations, but stronger for H-pol. The range of variation over the year is approximately 4 K for V-pol and 9 K for H-pol.

2.3.3 TB Filters for Hydrometeor Scattering

The very cold TBs that contribute to the long cold tail in the 89V histogram are most likely due to hydrometeor scattering. It is therefore necessary to find one or more filters that can remove data in which scattering occurs. It is not reasonable to simply remove any TBs below a given threshold in the histogram, since some of those cold TBs could be due to the surface signal.

One possible filter is to use the lower frequencies on the microwave radiometer to flag areas of precipitation. High rain rates tend to be correlated with areas of strong convection, which lead to the formation and lifting of ice. Using the other channels of the

radiometer to filter the high frequency TBs allows filtering without use of ancillary data. Stogryn et al. [54] developed four precipitation filters for SSM/I that can be applied to AMSR-E as well. The data are flagged as precipitation if the following conditions occur:

$$TB_{37V} - TB_{37H} > 50K \quad (2.1)$$

$$TB_{19V} > TB_{37V} \quad (2.2)$$

$$TB_{19H} > 185K \quad (2.3)$$

$$TB_{37H} > 210K \quad (2.4)$$

In addition to these low frequency flags, a set of high/low frequency combinations can be used to flag the data for precipitation [55],[56]. For application here with AMSR-E, filters can be developed by examining 2D TB histograms of the various combinations of 89 GHz vs. 18.7, 23.8, and 36.5 GHz with similar polarizations. These histograms are shown in Figure 2.19 for one month of data. The black dashed line in each plot is the 1:1 line where the TBs at each frequency are equal. For both polarizations, it is apparent that there is a correlation between low TBs at 89 GHz with high TBs at 18.7, 23.8, and 36.5 GHz. This is expected since higher amounts of water vapor and precipitation will increase the TBs observed at the lower frequencies, while at the same time decreasing the TBs at 89 GHz through scattering.

If there were no atmosphere on top of the ocean background, a higher frequency would result in a higher TOA TB due to the increase of surface emissivity with frequency. Therefore, all the TBs below the black dashed line should be from regions where there is a significant amount of atmospheric contribution which decreases the 89 GHz TB relative to the lower frequency channels, as would be expected from atmospheric scattering. For all frequency combinations, many of the very cold TBs at 89

GHz can be filtered from the data by removing TBs below the black dashed line. The effectiveness of this filter will be analyzed in Chapter 3.

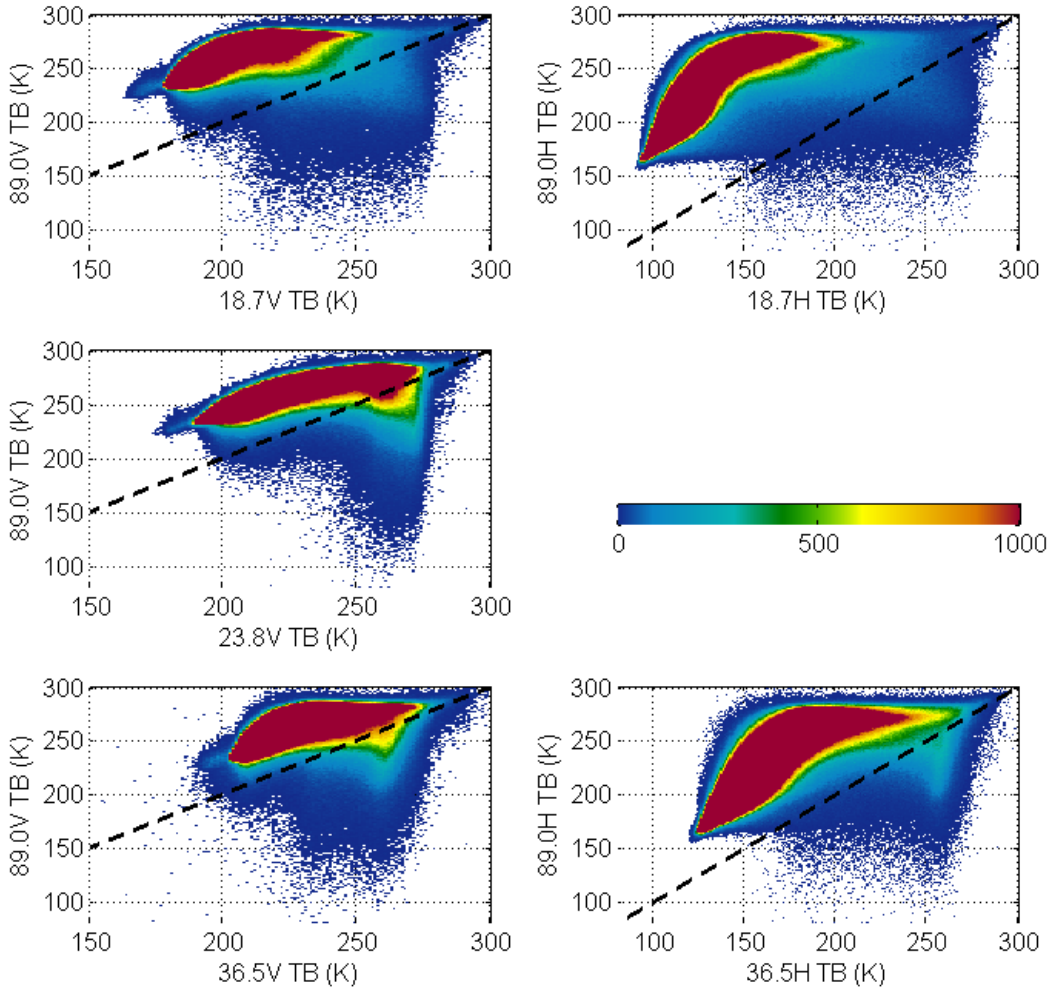

Figure 2.19: 2D histograms of 89 GHz vs. 18.7 GHz (top), 23.8 GHz (middle), and 36.5 GHz (bottom). The left column shows V-pol and the right shows H-pol. Colors indicate number of TB counts. Low 89 GHz TBs tend to be correlated with high TBs at the lower frequencies.

2.4 Summary

The vicarious cold calibration algorithm was described and applied to microwave imager brightness temperature data. The algorithm uses TB histograms to derive a stable reference statistic, referred to as the cold cal TB. The cold cal TB was calculated for one year of AMSR-E data for the frequencies between 10 and 37 GHz. The challenges with extending vicarious cold calibration to the higher frequencies around 90 GHz were presented and left to be analyzed in Chapter 3.

The cold cal TB was calculated for AMSR-E as a function of channel, month, and scan position. The cold cal TB was shown to be sensitive to geophysical variability and EIA variation, with the water vapor channel showing the greatest geophysical variability. The cold cal TB was also shown to vary across the radiometer's scan due to the EIAs not being constant across the scan. These sensitivities should be reduced in order for vicarious cold calibration to be used as a stable reference statistic for externally calibrating a spaceborne radiometer. Chapter 3 discusses how these sensitivities can be minimized by using simulated TBs generated using an RTM.

Chapter 3
The Vicarious Cold Calibration Single Difference

3.1 Introduction

The vicarious cold calibration single difference provides a way to calibrate a spaceborne microwave radiometer that significantly reduces the dependence of the cold cal TB on geophysical variability as well as on instrument characteristics such as EIA and frequency. The single difference makes use of the cold cal TB calculated from a radiometer's observations (obs) and compares it to a cold cal TB calculated from simulations (sims). The simulations are TOA TBs that are generated using an RTM with ocean surface properties and atmospheric profiles taken from ancillary data. Since the coldest TBs usually occur for calm ocean scenes with no clouds and minimal water vapor, these conditions are relatively straightforward to simulate. Observed TBs over land and sea-ice are not used in vicarious cold calibration so it is unnecessary to model the TOA TB over these surfaces.

The RTM uses the model described in (1.5)-(1.8). It is composed of surface emissivity and atmospheric absorption models, as well as geophysical inputs from ancillary data. The surface emissivity is found using a combination of models that includes the Meissner and Wentz ocean dielectric model [57], along with the Hollinger surface roughness [58], Stogryn foam [59], Wilheit wind speed [60], and Elsaessar surface [61] models. Although vicarious cold calibration finds the coldest TBs that occur with calm winds, it is still necessary to have a surface emissivity model that accounts for

wind. This is because the cold cal TB is found by extrapolating to the coldest TB point using slightly warmer TBs that might include surface wind effects. The effect of wind direction on emissivity is ignored here as this should be a small, zero-mean perturbation. The additive effect of wind direction scales with wind [62] and vicarious cold calibration uses only TB data with light wind, usually less than 10 m/s as seen in Figure 2.7. The geophysical inputs from the ancillary data include SST and wind speed data. The SSS is taken to be 34 ppt for the entire globe, since the small changes in SSS do not strongly impact the microwave frequencies simulated here.

Absorption in the atmosphere is accounted for by the Rosencrantz 1998 model for water vapor [10], the Liebe 1991 model for liquid water [63], and the Liebe 1992 model for oxygen absorption [11]. The RTM also requires geophysical inputs that include atmospheric and surface parameters such as SST, surface wind speed, and profiles of temperature and relative humidity. GDAS [47] is one example of ancillary data that gives these parameters. GDAS also gives a field for total integrated cloud liquid water (CLW) content. Since it is difficult to simulate CLW properly, only those pixels where GDAS gives CLW equal to zero are simulated. This still gives a sufficient sample size of TBs to perform vicarious cold calibration. The input parameters are provided every six hours over the entire globe at 1° latitude/longitude intervals. The simulated TBs from the RTM are created using the center frequencies, polarization, and EIAs that correspond to the radiometer of interest at the closest grid point in space and time. EIAs are given in the radiometer data file for each pixel observation and these are used in the simulations, since they are more accurate than using a nominal EIA for all pixels. The Noise Equivalent Delta Temperature (NEDT) calculated for the radiometer at each channel is also used in

the simulations. The NEDT is added to the TOA TBs using a random distribution with a mean of zero and standard deviation equal to the NEDT.

An illustration of how well the simulated TBs match the observed TBs is shown in Figure 3.1. The left panel is 23.8 GHz V-pol TB data from part of an AMSR-E orbit. The latitude, longitude, scan time, and EIA at each pixel from the orbit are input to the RTM, which finds the closest point in space and time from GDAS and simulates the TOA TB as shown in the right panel. The RTM has a coarser resolution than the observations, but it does a relatively good job at simulating key atmospheric features in the observed TBs.

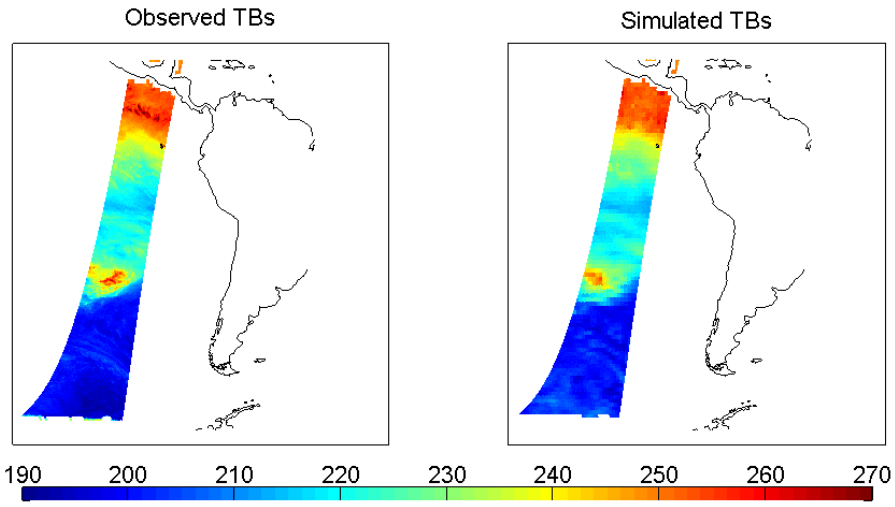

Figure 3.1: AMSR-E observed 23.8V TBs (left) and simulated 23.8V TBs (right). The simulated TBs are generated for every pixel location.

A comparison between observed and simulated TB histograms for AMSR-E 36.5 GHz V-pol is shown in Figure 3.2. The TBs are from one month using global data at a single scan position. Only the TBs at the coldest part of the histogram will impact the derivation of the cold cal TB, so the key feature of interest is the shape of the histogram at the cold end which is very similar between the observed and simulated TBs. On the other hand, the warm end histogram shapes are quite different and this can be attributed

to the simulations not including rain. The long tail at the warm end of the observed histogram is due to rain, while those pixels in the simulations are just modeled as areas with high amounts of water vapor. Another interesting feature to note is that the TB histogram minima are not the same between the observations and simulations. It is not possible to determine whether this difference is from errors in the absolute calibration of the radiometer or because the simulations incorrectly model reality.

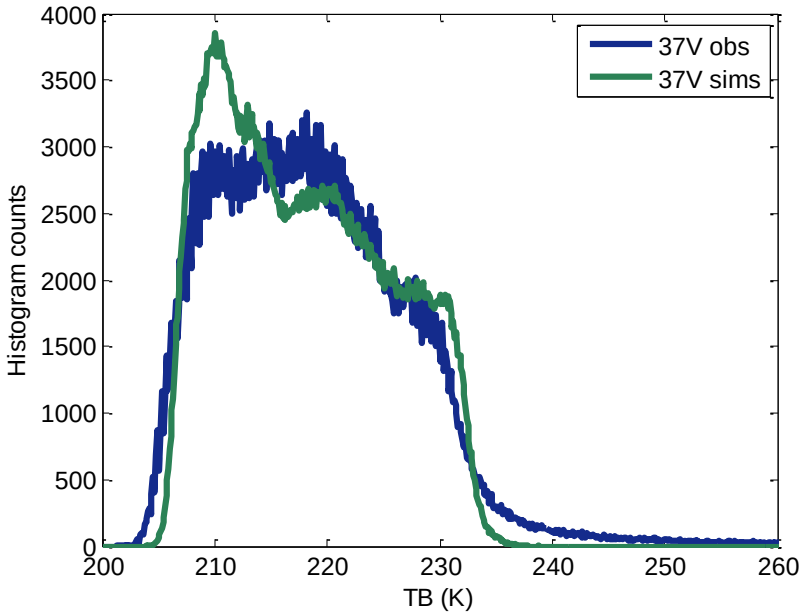

Figure 3.2: Example of the observed TB histogram (blue line) and simulated TB histogram (green line) for AMSR-E 36.5 GHz V-pol. Although the overall shapes of the histograms differ, the shape at the cold end is similar which is what factors into vicarious cold calibration.

One concern with incorporating simulated TBs to compare with observed TBs through vicarious cold calibration is how the global distribution of the coldest TBs compares between the simulations and observations. If the location where the coldest TBs come from is different between the observations and simulations, it may not be realistic to say that the simulations accurately model the radiometer TBs. It is important that the simulations do model the observations accurately, at least for the coldest TBs that

are input to the vicarious cold calibration algorithm. A similar analysis as that done in Section 2.1.1 is done here for the observations as well as the simulations, showing the regions of the globe where the coldest 10% TBs originate. Figure 3.3 shows the regions of the globe where the coldest 10% TBs originate for AMSR-E 18.7V observations (top) and simulations (bottom) for January 2006. The observations and simulations show very similar locations for the coldest TBs.

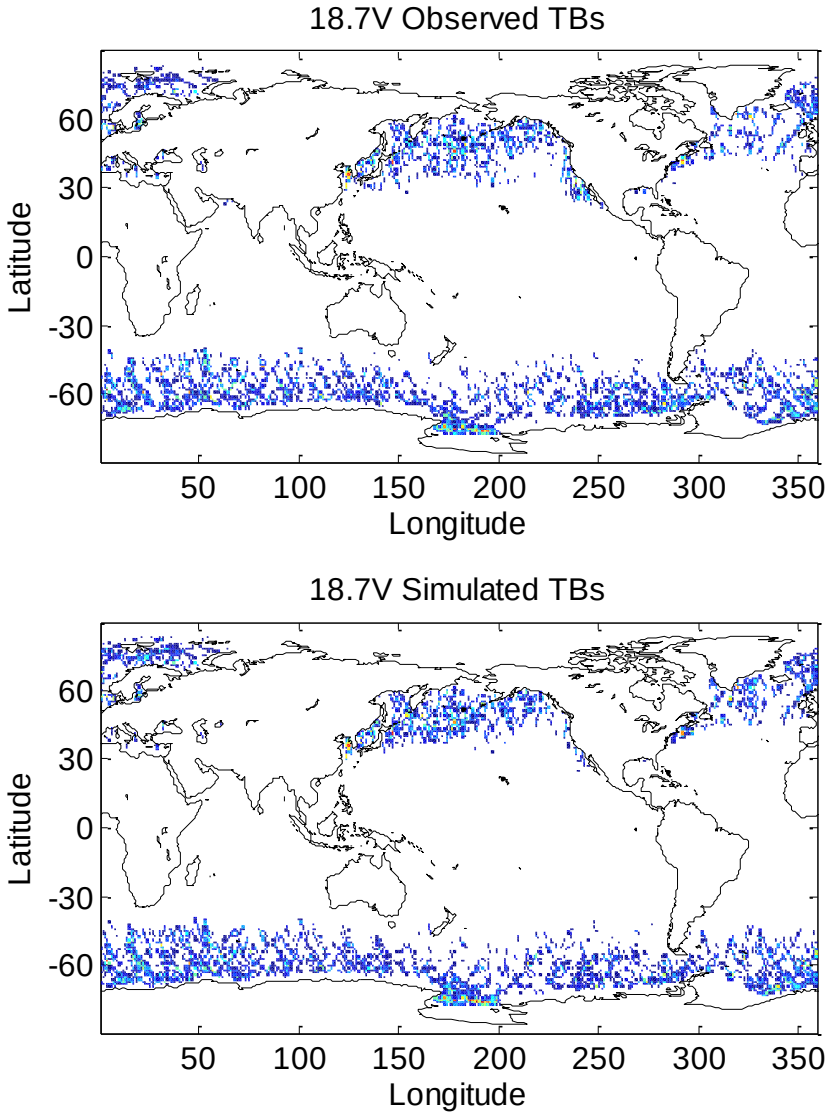

Figure 3.3: AMSR-E 18.7V observed (top) and simulated (bottom) TBs for the coldest 10% CDF of the total TB histogram for January 2006.

3.2 Single Difference for Microwave Imagers from 10 to 37 GHz

Section 2.2.2 showed that the cold cal TB displays a seasonal cycle which is undesirable in a calibration reference. Since the RTM simulates what the radiometer should observe, the geophysical variability can be characterized and reduced in the single difference. Figure 3.4 gives an example of this by showing the value of the single difference and cold cal TB over one year for AMSR-E 23.8 GHz V-pol. Only the NH is shown since it displays the strongest seasonal cycle as seen in Figure 2.10. The seasonal cycle amplitude for the observed cold cal TB is 9.08 K, while for the single difference the amplitude is reduced to 1.56 K.

Table 3.1 summarizes the results for the observed cold cal and single difference seasonal cycle amplitudes. For comparison, both AMSR-E 10.65V and 23.8V GHz channels are given for the globe, NH, and SH. In all cases, the single difference reduces the seasonal cycle in the observed cold cal TB. For example, the AMSR-E 23.8V channel displays a 4.35 K seasonal cycle amplitude in the observed cold cal TB for the globe. The inclusion of the simulated TBs in the single difference decreases this amplitude to 0.97 K. It does appear that the simulations slightly over-estimate the seasonal cycle, as seen by the single difference in Figure 3.4. However, the seasonal cycle amplitude is still drastically reduced by incorporating the simulations. Another concern with the single difference is that it still leaves an amplitude of around 1 K in the seasonal cycle for both 10.65V and 23.8V in the NH. This will be discussed in Section 4.3 as an uncertainty in the calibration.

The single difference (average of the 12 months) for all AMSR-E channels is shown in Table 3.2. The value of the SD appears to scale with frequency (36.5V

excluded), and the H-pol channels have a higher SD than their respective V-pol channels. The likely reason for the increase in SD with respect to frequency is an error associated with simulating water vapor, while the higher SD in the H-pol channels is most likely due to errors in simulating wind speed. One way to see the impact of simulating the wind speed on the SD is to set the wind speed equal to 0 m/s (rather than using the GDAS wind speed) and re-calculate the cold cal TB using these simulated TBs. The resulting SD is shown in Table 3.3. This analysis shows that the wind speeds have a significant impact on the simulated cold cal TB for the H-pol channels but hardly any impact on the V-pol channels. The SD increased for the H-pol channels when the wind speed was reduced to 0 m/s, so it is necessary to include the ancillary data for wind speeds in the simulations. The single difference is only concerned with achieving relative accuracy, rather than absolute accuracy, so the value of the single difference is less of a concern compared to achieving stability. The best way to achieve stability in the single difference is to use ancillary data for geophysical inputs to the RTM, even though they may not be completely accurate.

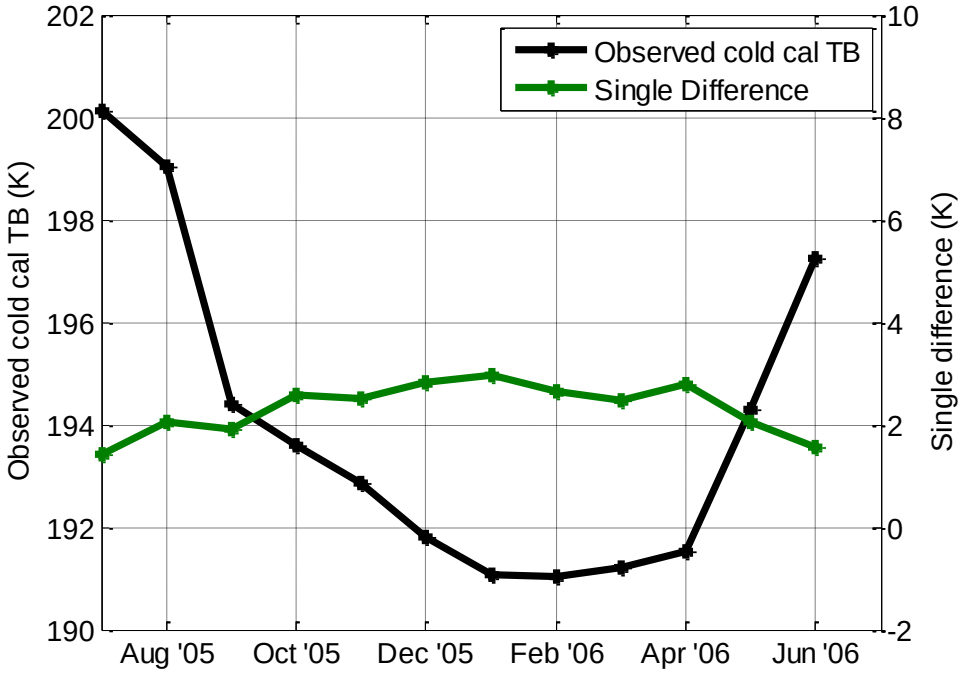

Figure 3.4: Comparison of AMSR-E observed cold cal TB (black line) and single difference (green line) for the NH. The simulated TBs are able to model the geophysical variability and reduce the seasonal cycle.

Seasonal cycle amplitude (K)		**Globe**	**NH**	**SH**
AMSR-E 10.65V GHz	***Observed cold cal TB***	0.69	1.17	0.65
	Single Difference	0.56	1.12	0.44
AMSR-E 23.8V GHz	***Observed cold cal TB***	4.35	9.08	1.85
	Single Difference	0.97	1.56	0.81

Table 3.1: Summary of results for the observed cold cal TB and single difference seasonal cycle amplitude. The single difference has a smaller seasonal cycle amplitude than the observed cold cal TB, most notably for the 23.8 GHz water vapor channel.

	10.65V	**10.65H**	**18.7V**	**18.7H**	**23.8V**	**36.5V**	**36.5H**
Single Difference (K)	0.41	1.23	0.98	3.02	2.05	-1.53	3.15

Table 3.2: Single difference for AMSR-E channels, averaged over July 2005 - June 2006.

	10.65V	10.65H	18.7V	18.7H	23.8V	36.5V	36.5H
Single Difference (K)	0.55	3.89	1.11	1.04	2.21	-1.40	7.80

Table 3.3: Single difference for AMSR-E channels, averaged over July 2005 - June 2006 using simulated TBs that use a wind speed of 0 m/s for all pixels instead of the GDAS wind speed.

Since the cold cal TB also varies as a function of EIA as shown in Figure 2.15, the single difference needs to be able to remove any EIA variation so it is not included in the calibration. The best way to illustrate how the single difference accounts for EIA variation is to consider the cold cal TB across the scan. Figure 3.5 shows the observed cold cal TB (blue line) and the single difference (green line) for AMSR-E 10.65 GHz V-pol for the SH descending orbits. The single difference shows that the simulations are able to model the observations and reduce the effect of EIA variation on the cold cal TB to approximately 0.1 K across the scan.

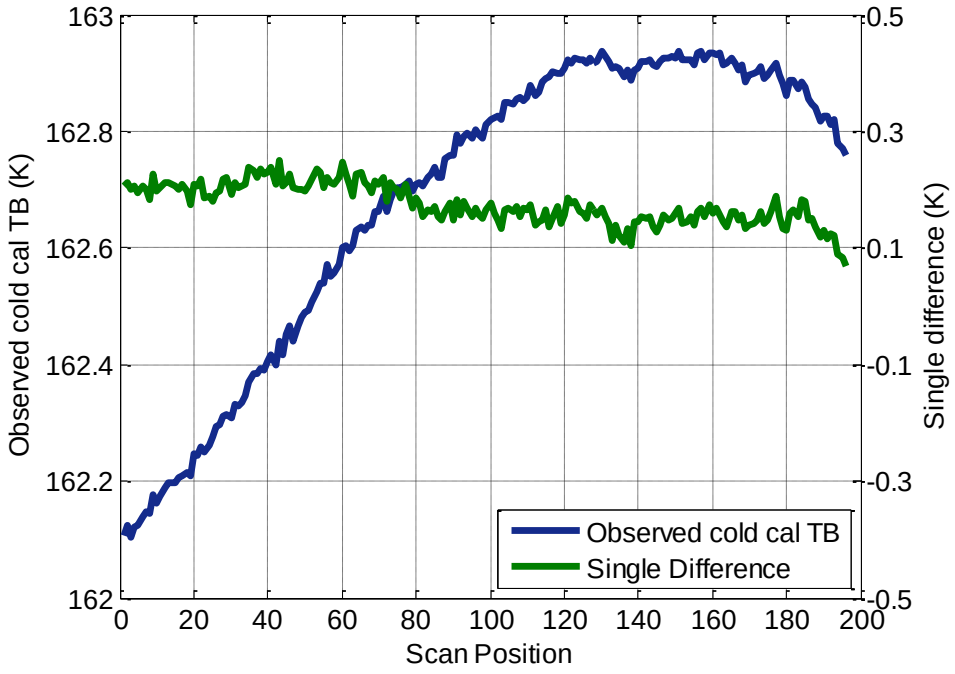

Figure 3.5: Observed cold cal TB and single difference across the scan for AMSR-E 10.65V SH descending orbits. The simulations are able to model the EIA variation across the scan and reduce the variation for the single difference.

3.3 Extension of Single Difference to High Frequency Range 85 – 92 GHz

3.3.1 Introduction

As discussed in Section 2.3, extending vicarious cold calibration to higher frequencies introduces several challenges. The single difference can be used to mitigate these challenges by using the simulated TBs to determine adequate filters. This section will analyze various filters that can help remove the cold TBs due to hydrometeor scattering.

One concern with extending vicarious cold calibration to the higher frequency range is the greater sensitivity to geophysical variability. The 89V channel shows a variation of about 4 K over a year while the 89H channel has a larger variation of about 9 K (see Figure 2.18). The single difference is effective at minimizing this variation for the AMSR-E 23.8V channel (see Figure 3.4) and should also help at the higher frequencies. One concern with extending the RTM to higher frequencies is the possibility of greater errors in the simulated TBs due to atmospheric water vapor and CLW errors in the RTM input fields. However, since vicarious cold calibration only uses the coldest TBs in the histogram when deriving the cold cal TB, these TBs only include minimal amounts of water vapor as confirmed in Figure 2.6. CLW is mitigated by not simulating those pixels where GDAS says there are clouds. This should help to minimize errors associated with water vapor and CLW. Figures 3.6 and 3.7 compare the observed and simulated cold cal TB and illustrate the ability of the simulations to model the observations through the single difference for 89V and 89H. The reduction of the seasonal cycle is most evident in the 89H channel.

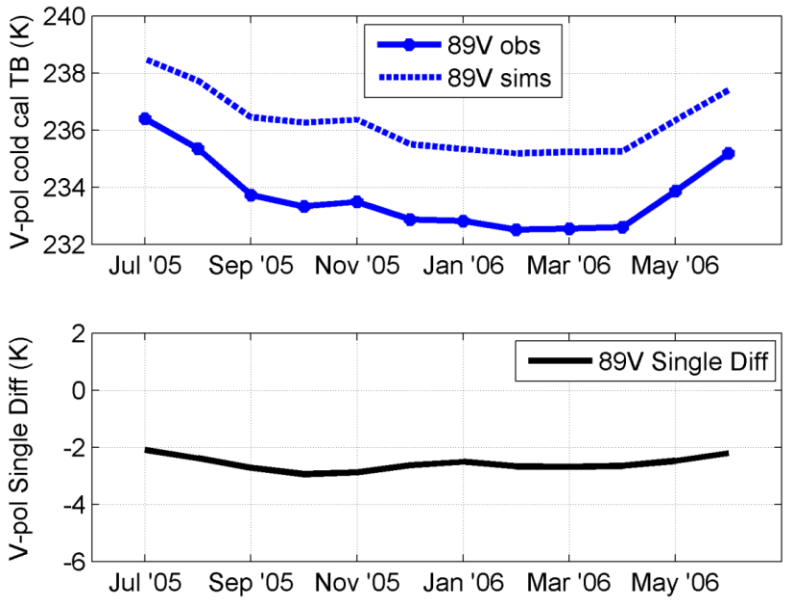

Figure 3.6: Cold cal TB for AMSR-E 89V observed and simulated TBs (top) and single difference (bottom) by month for July 2005 - June 2006. The simulations are able to model the seasonal variation in the cold cal TB and reduce it in the single difference.

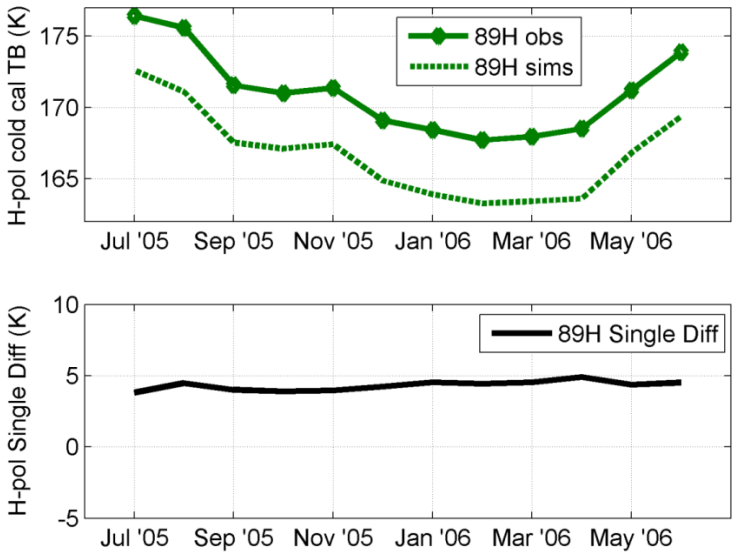

Figure 3.7: Cold cal TB for AMSR-E 89H observed and simulated TBs (top) and single difference (bottom) by month for July 2005 - June 2006. The simulations are able to model the seasonal variation in the cold cal TB and reduce it in the single difference.

While the simulations appear to improve the calibration by minimizing the seasonal signal, they do not solve the problem of the long cold tail due to hydrometeor scattering. The RTM only accounts for absorption in the atmosphere and does not include

the effects of scattering. Clouds are filtered by removing those pixels where GDAS has CLW greater than zero, however this is not a sufficient filter to remove all areas of hydrometeor scattering. Further filtering of the TBs needs to be done to reduce the cold tail observed in the TB histogram in Figure 2.18. The next sections will discuss potential filters that can be used to remove the cold TBs due to hydrometeor scattering and will use the single difference to analyze the effectiveness of the filters.

3.3.2 Identification of Filters to Remove TBs Associated with Hydrometeor Scattering

One potentially useful filter for hydrometeor scattering that requires ancillary data is cloud top temperature (CTT). CTT products can be derived from thermal IR sensors. Cold CTTs are correlated with areas of strong convection, so knowledge of the CTTs could greatly help in reducing the hydrometeor scattering signature in the TB data. The Aqua platform which has AMSR-E onboard also has a visible/IR imager, the Moderate Resolution Imaging Spectroradiometer (MODIS). MODIS Level 2 products contain a CTT field [64] that can be used to filter AMSR-E TB data. The MODIS swath is wide enough to cover the entire AMSR-E scan, with a small time difference of approximately two minutes separating the MODIS observations from the AMSR-E observations.

The relationship of CTT to cold observed TBs that are a result of hydrometeor scattering can be seen by taking the difference between observed TBs and simulated TBs at the same pixel and plotting it against CTT. Since the simulations do not include scattering effects, the simulated TB will be warmer than the observed TB in regions of hydrometeor scattering. The result of this analysis is shown as a 2D histogram for 89V in Figure 3.8, where the colors indicate counts. The CTT fields from MODIS are re-gridded

to the AMSR-E observations using a linear interpolation. The 2D histogram has an asymmetric shape, showing a large region of data at cold CTTs where the observed TB is less than the simulated TB. This indicates that the magnitude of the scattering increases with decreasing CTT.

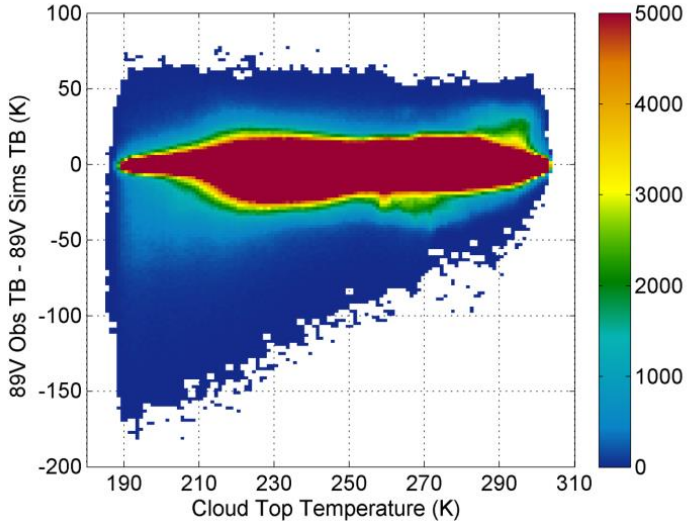

Figure 3.8: 2D histogram of 89V observed TBs minus simulated TBs vs. cloud top temperature for January 2006. Colors indicate number of counts. The magnitude of the scattering increases with decreasing CTT.

Another useful application of the CTT fields is to identify a relationship between SSTs and CTTs, so that an SST filter can be applied to the data. This would allow a filter using ancillary data that is already being used for the simulations (e.g. GDAS), rather than co-locating CTT data with radiometer data. A 2D histogram can also be used to compare CTT to SST, as shown in Figure 3.9. The SST fields are taken from GDAS and are shown for one month of data (January 2006). The coldest CTTs are associated with warm SSTs and therefore the warm SSTs are associated with a relatively high probability of hydrometeor scattering. If the SSTs were restricted for vicarious cold calibration, it might help eliminate much of this scatter effect on the cold cal TB.

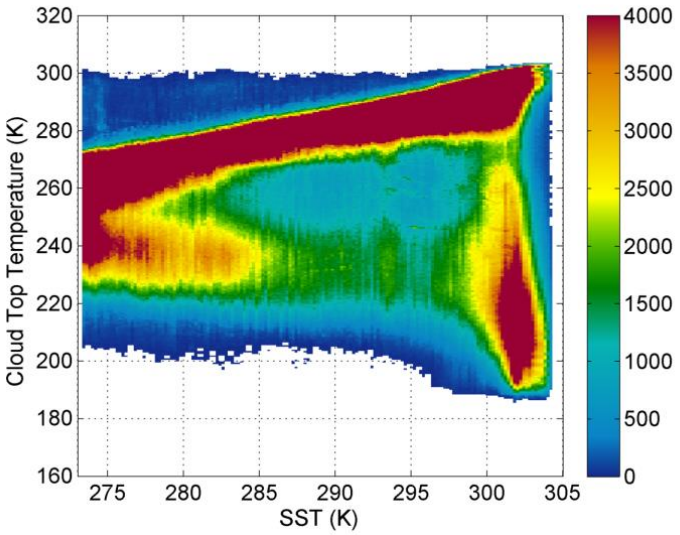

Figure 3.9: Cloud top temperature vs. SST 2D histogram for January 2006. Colors indicate number of counts. Most of the very cold CTTs occur at high SSTs.

Using CTT fields as well as SST fields give two more potential filters to use to reduce hydrometeor scattering, in addition to the high/low frequency combinations identified in Section 2.3.3. These three filters are analyzed in the next section for their effectiveness at removing the cold TBs due to hydrometeor scattering.

3.3.3 Application of TB Filters

The three filters applied to the TB data are a precipitation filter (high/low frequency combinations), a CTT filter using MODIS data, and an SST filter using GDAS data. Each of these filters is analyzed to determine what threshold value is appropriate to stabilize the vicarious cold cal TB. The 'threshold value' refers to a cut-off point, for instance, filtering out all TBs with an SST greater than 300 K. This threshold is varied and the effect on the single difference is observed.

The filter in (2.1) uses the difference between V and H polarizations at 37 GHz to look for the polarization signature from precipitation. The threshold of 50 K in this equation is analyzed to determine whether this is the appropriate value to use in a high

frequency TB filter. This threshold value is varied from 0 to 70 K and the filter is applied to the 89 GHz observed and simulated TBs. The vicarious cold calibration algorithm is then performed on both the observed and simulated TBs and the results are shown in Figure 3.10 for 89 GHz V-pol. A sign that the filter is properly removing cold TBs due to scattering and not the surface signal is that the observed cold cal TB is warming while the simulated cold cal TB (which does not include scattering) remains unchanged.

Figure 3.11 shows the single difference as well as the derivative of the single difference with respect to the precipitation filter threshold. The objective of this analysis is to determine the optimal threshold value to remove scattering effects. As the threshold value is increased, more TBs are filtered out which in turn affects the derived cold cal TB. At some point, increasing the threshold further destabilizes the single difference as the sample size becomes too small. This effect can be seen by looking at the derivative of the single difference with respect to the threshold. In Figure 3.11, this transition occurs around 50 K. Below 50 K, the single difference increases at a constant rate. This increase is due to the warming of the observed cold cal TB while the simulated cold cal TB remains unchanged (see Figure 3.10) since the filter is removing only those regions of high scattering. Above 50 K, the single difference and its derivative increase rapidly with increasing threshold indicating relative instability of the vicarious cold calibration statistic. Therefore, a precipitation flag threshold of 50 K can be used which supports the findings of [54]. The AMSR-E data used in this analysis are from July 2005 only; however, the other data follow the same general pattern.

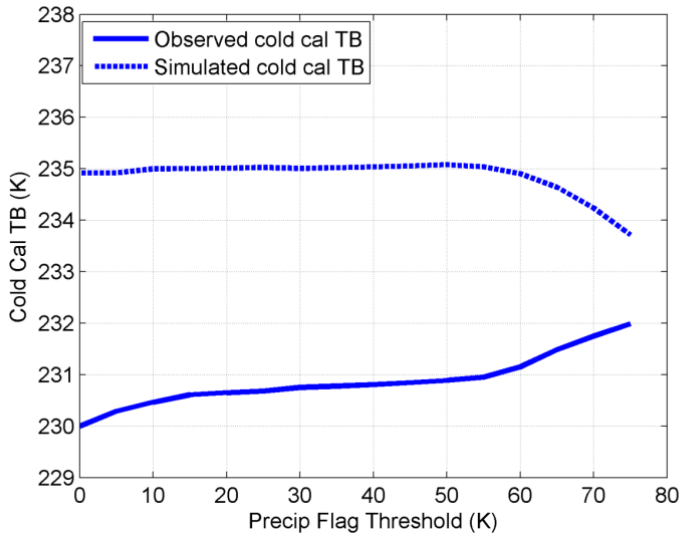

Figure 3.10: Observed and simulated cold cal TB using different filter thresholds for 37V – 37H.

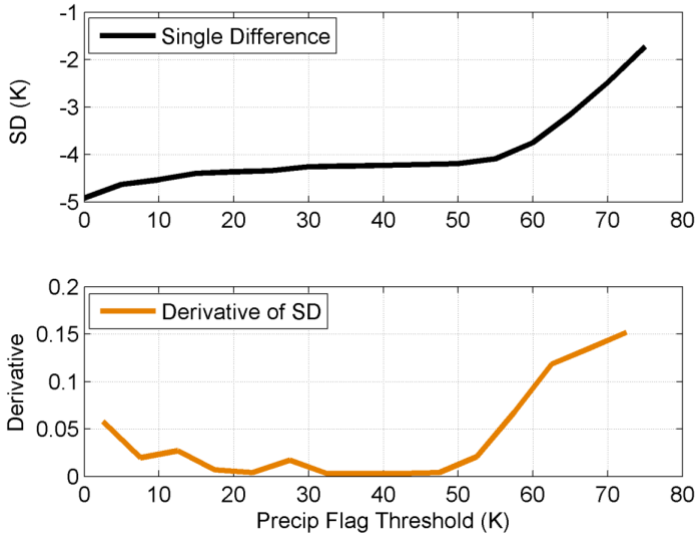

Figure 3.11: Single difference and the derivative of the single difference with respect to the TB threshold. A threshold of 50 K is a reasonable value for the filter.

The other filters that make use of the radiometer's lower frequencies are those combinations shown in Figure 2.19. A similar analysis to the one for 37V/37H above is performed for these five combinations to derive the filters given in (3.1)-(3.5). These five combinations as well the 37V/37H combination above are collectively used as the precipitation filter.

$$TB_{89V} > TB_{19V} + 10K \quad (3.1)$$

$$TB_{89H} > TB_{19H} + 30K \quad (3.2)$$

$$TB_{89V} > TB_{22V} \quad (3.3)$$

$$TB_{89V} > TB_{37V} \quad (3.4)$$

$$TB_{89H} > TB_{37H} + 10K \quad (3.5)$$

The CTT and SST filters are also analyzed according to the method described above. It is found that a filter which removes all pixels with CTT below 230 K is effective at eliminating hydrometeor scattering. The scattering is also mitigated by a filter that removes regions where the SST is greater than 300 K for both polarizations. These three filters are applied to both the V-pol and H-pol 89 GHz TBs in the following analysis to determine how the filters impact the cold cal TB. The impact of the filters on the cold cal TB can be seen by plotting the cold end of the TB histogram for each filter to see how each does at removing the cold tail. Also, by looking at the yearly single difference, the variation in the single difference over a year gives a good indication of how well the filters remove the hydrometeor scattering.

3.3.3.1 Vertical Polarization

The single difference for AMSR-E 89V is calculated using the three filters previously described. The results are shown in Figure 3.12. Each of the three filters improves the single difference; however, it does not appear necessary to use the SST filter since the precipitation filter shows greater improvement in the single difference. Also, since the CTT filter and precipitation filter give approximately the same improvement to the cold cal TB, it is not necessary to use both of them. It is far more convenient to use the precipitation filter rather than the CTT filter since it does not require co-located thermal IR data.

The effectiveness of the filters at removing the cold tail in the TB histogram is shown in Figure 3.13. The TB histogram uses one month of AMSR-E 89V observations. The SST filter removes part of the tail while the CTT and precipitation filters remove more of the tail. This gives a lower bound to the TB histogram that is associated with the cold surface TBs and not hydrometeor scattering, leading to a more stable cold cal TB. There is the possibility that not all areas of hydrometeor scattering are removed, so there may be some very cold TBs that are still being included in the cold calibration algorithm. These should have a very minimal impact since the tail is no longer as pronounced with the precip filter.

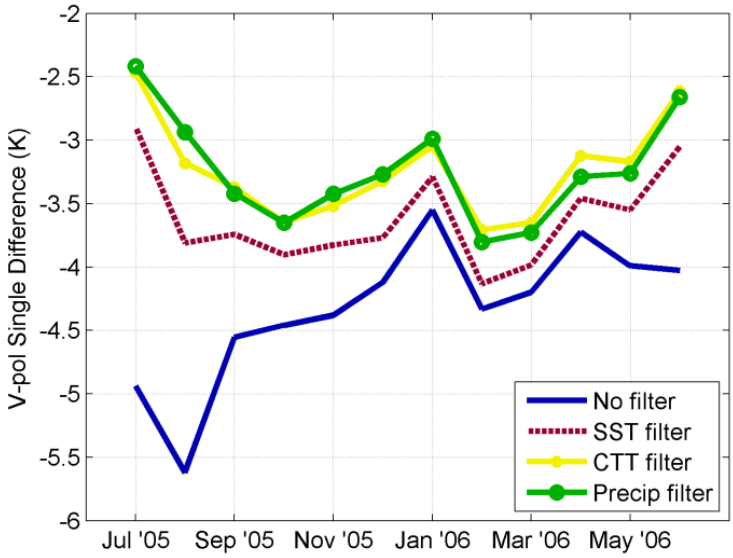

Figure 3.12: Single difference for AMSR-E 89V with various filters applied. The precipitation filter and CTT filter give the best performance.

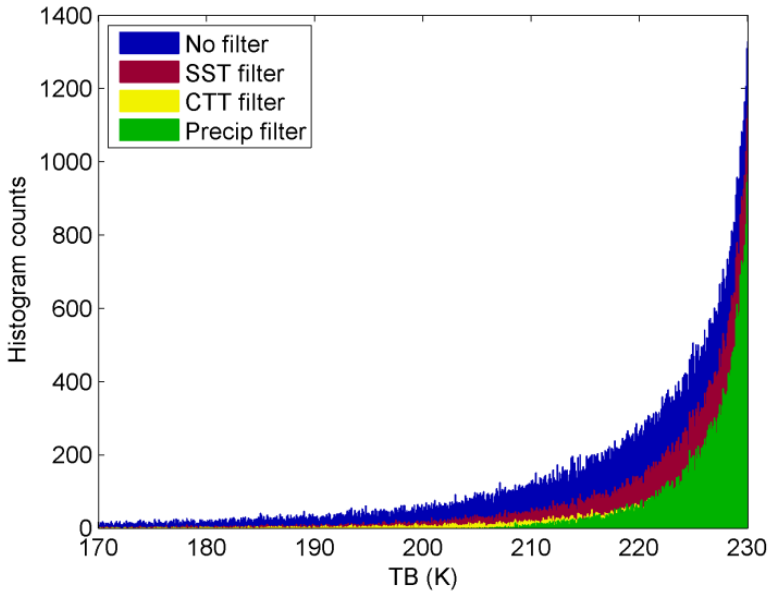

Figure 3.13: TB histograms for 89V with various filters applied. The precipitation filter removes the largest percentage of the cold tail.

3.3.3.2 Horizontal Polarization

The single difference for AMSR-E 89H is also calculated using the three filters previously described and the results are shown in Figure 3.14. The filters have a less significant impact at H-pol than they do at V-pol. One reason for this could be that H-pol does not have as large a cold tail in the histogram due to scattering. Since the H-pol cold cal TB is much lower than that at V-pol (about 165 K at H-pol compared with 230 K at V-pol), there are not as many cold TBs from hydrometeor scattering that are colder than the H-pol cold cal TB relative to V-pol. This can be seen in the TB histograms for H-pol shown in Figure 3.15. While there is a slight cold tail in the histogram, it is not nearly as substantial as the tail at V-pol (see Figure 3.13). The bottom plot in Figure 3.15 shows the same histogram as the top, with a smaller TB range to better observe the cold tail. What little tail does exist in the H-pol TB histogram is removed by the precipitation filter.

Unlike V-pol, no one filter appears to perform better than any of the other filters. Since the precipitation filter is the best for V-pol and is shown to be the filter that best removes the H-pol histogram cold tail as seen in Figure 3.15, it will be the filter implemented for the H-pol TBs.

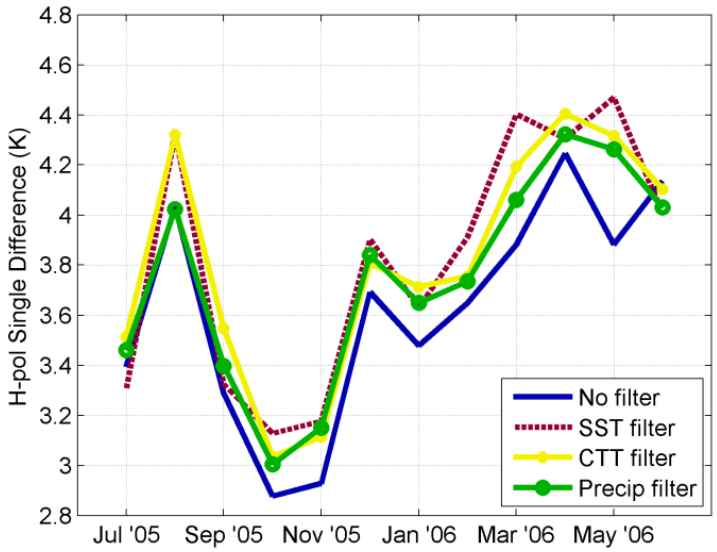

Figure 3.14: Single difference for AMSR-E 89H with various filters applied. The filters do not have as significant an impact on the cold cal TB for H-pol as they do for V-pol.

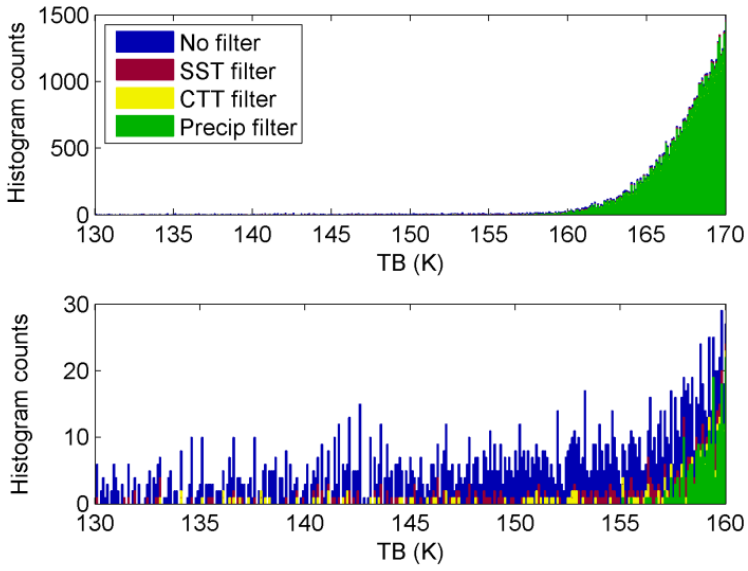

Figure 3.15: TB histograms for 89H with different filters applied. The bottom plot has a smaller TB range to highlight the cold tail. H-pol does not have a significant cold tail, but the precipitation filter removes what little tail there is.

3.4 Application of the Single Difference: Satellite Attitude Analysis

3.4.1 Introduction

Measurements made by spaceborne microwave radiometers are sensitive to the EIA, as shown in Figure 2.14 for conical scanning radiometers. The change in EIA that is reflected in the cold cal TB across the scan is due to small variations in the attitude of the satellite. Satellites have onboard attitude control systems; however, a satellite can have small offsets in its pitch, roll, or yaw. These small offsets noticeably affect the TB measured by the radiometer onboard the satellite and must be accounted for when analyzing the data. The single difference was shown to effectively model the effect of EIA on the TBs across the scan and to minimize this variation. This analysis was performed with knowledge of the EIAs at every pixel of the radiometer; however, if the EIAs are not known, the single difference can be used to back out the EIAs of the radiometer. This section will discuss how to derive a radiometer's EIAs using the vicarious cold calibration single difference.

Conical scanning microwave radiometers have a reflector antenna that is offset from nadir and kept at a constant angle as they scan. The observed TB is a function of the EIA, which is the angle the reflector projects onto the surface of the Earth as measured from zenith. Due to the curvature of the Earth, the EIA is not simply equal to the off-nadir angle of the reflector antenna. It is instead a function of the altitude of the satellite as well as the radius of the Earth as shown in Figure 3.16. The spin axis of the radiometer is oriented vertically with respect to the Earth's surface if there is no pitch or roll of the satellite. On a spherical Earth, the path the radiometer traces out on the surface would be a circle, resulting in a constant EIA over the scan. However, the Earth is slightly oblate,

meaning that the radius of the Earth changes with latitude. This will have a small effect on the EIA across the scan as well as throughout the orbit. Also, if the satellite orbit is not perfectly circular, the altitude of the satellite will change throughout the orbit and affect the EIA. Accounting for the oblateness of the Earth and the altitude of the spacecraft allows a nominal EIA to be calculated for a 0° pitch and roll offset. When a pitch or roll offset of the satellite is introduced, the spin axis of the radiometer is no longer oriented vertically. The true off-nadir angle is no longer equal to the off-nadir angle of the reflector and will change as the radiometer scans. This will cause the EIA to change as a function of the scan position with respect to the nominal EIA. This deviation from the nominal EIA can be used to calculate the pitch and roll offset of the satellite.

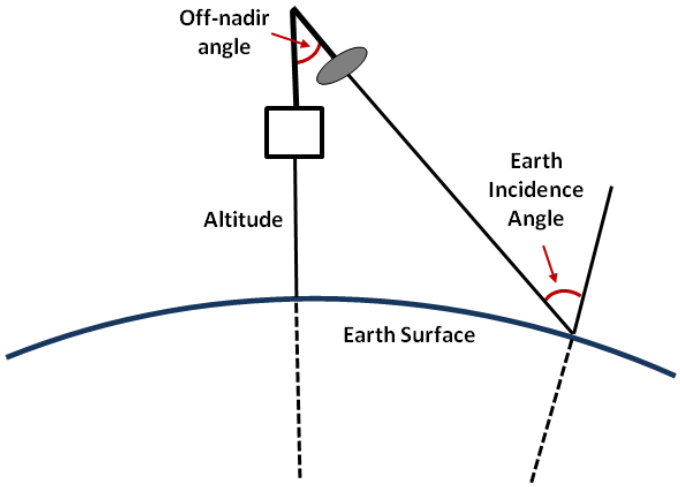

Figure 3.16: Geometry of the EIA for a spaceborne microwave radiometer.

Typical methods for obtaining the pitch and roll offset of a satellite using the microwave radiometer onboard include geolocation analysis and over-ocean scan biases. Examples of these methods applied to the WindSat radiometer and the Special Sensor Microwave Imager/Sounder (SSMIS) are described in [66]-[68]. Vicarious cold

calibration will be used here to show that a similar pitch and roll offset can be calculated using the single difference.

3.4.2 Pitch/Roll Retrieval Algorithm

A least squares retrieval method is used to compute the pitch and roll offsets of the satellite from the cold cal TB across the scan. This is done by minimizing the squared difference between the observed cold cal TB and the simulated cold cal TB, i.e. the single difference, until the retrieved pitch and roll converge to within an acceptable error, which is taken here to be 0.01°. The simulated TBs are created by assuming that the satellite has a pitch and roll offset that are both 0°. In order to calculate the EIA that is input to the RTM, it is necessary to know the altitude of the satellite as well as the radius of the Earth. The altitude of the satellite is obtained from satellite telemetry. The Earth can be modeled as an oblate spheroid with the radius of the Earth changing as a function of latitude [69]. This generates a modeled cold cal TB at the nominal EIA that includes altitude and Earth oblateness effects, from which a pitch and roll offset that matches the observed cold cal TB can be found.

The rotational transformations that are required to derive the true off-nadir angle as a function of the scan position for a given pitch and roll are given in [70]. These transformations calculate the true off-nadir angle given a pitch, roll, yaw, elevation angle, and azimuth angle. The elevation angle and the azimuth angle describe the pointing of the radiometer instrument with respect to the satellite coordinate system. The elevation angle is the off-nadir angle of the radiometer reflector measured from vertical and the azimuth angle describes the scan position. The sign convention for pitch and roll angles is shown

in Figure 3.17. A positive pitch is upward and a positive roll is clockwise rotation (when looking in the forward direction of the satellite). The yaw of the spacecraft is assumed to be 0°. A downside of using vicarious cold calibration for satellite attitude analysis is that a yaw offset cannot be retrieved. On a spherical Earth, a yaw offset does not affect the EIA since the EIA is constant for all latitudes. On the real Earth, a yaw offset will cause the EIA to change slightly due to Earth's oblateness; however, this EIA change is too small to be detected by the cold cal TB.

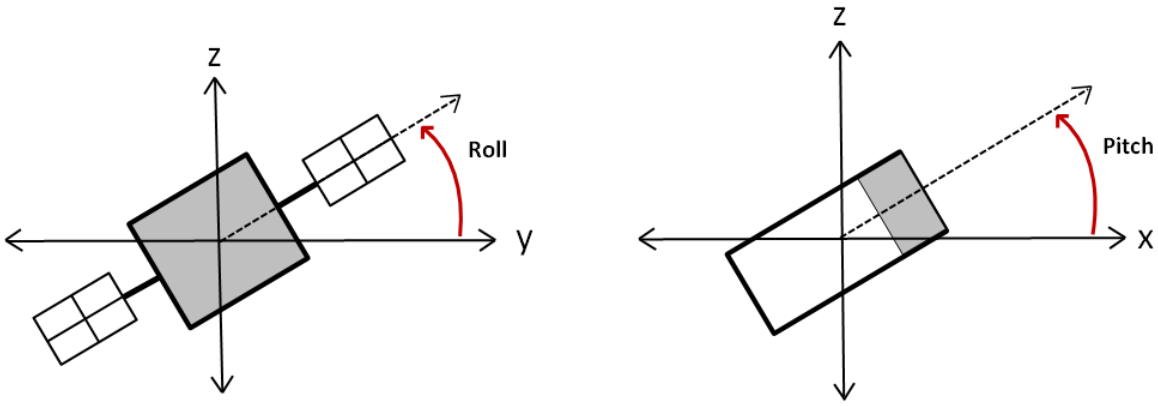

Figure 3.17: Positive roll and pitch angles of a satellite. The grey shaded area indicates the front of the satellite, i.e the forward-looking side of the satellite.

3.4.3 Application to the WindSat Radiometer

The pitch/roll retrieval algorithm is applied to the WindSat radiometer [71] to analyze the performance of the algorithm. Pitch and roll values have been calculated for WindSat using the geolocation method and over ocean scan biases [66],[67], providing a means by which to evaluate this method.

The cold cal TB across the scan as derived from WindSat observations over a year of data from July 2005 – June 2006 for the 10.7 GHz V-pol channel is given in Figure 3.18. The 10.7 GHz channel is chosen due to the minimal contribution from the atmosphere relative to the remaining channels. Furthermore, V-pol is chosen since it is

more sensitive to EIA changes than H-pol (see Figure 2.14). There is a clear scan bias of approximately 0.5 K in the cold cal TB shown in Figure 3.18, which can be attributed to EIA variability across the scan.

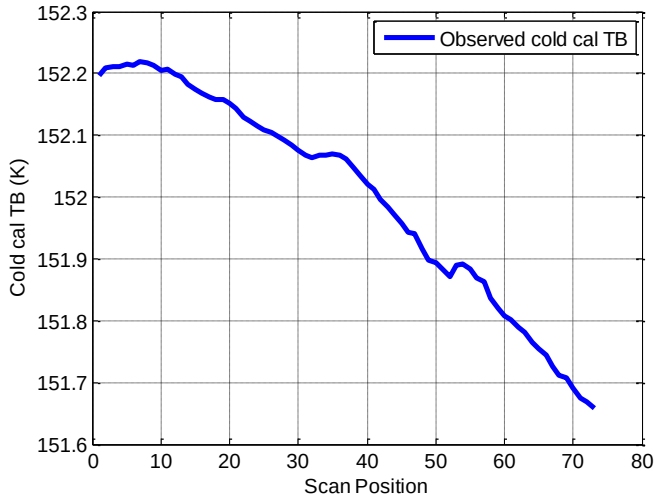

Figure 3.18: Observed cold cal TB across the scan for the WindSat 10.7V GHz channel.

The pitch/roll retrieval algorithm is used to derive a simulated cold cal TB across the scan using EIAs calculated from a given pitch and roll offset. Figure 3.19 shows the results of this analysis, including the simulated cold cal TB with the derived pitch and roll offset (green line) along with the observed cold cal TB (blue line) and the nominal EIA simulated cold cal TB (black line). The retrieved pitch and roll offsets that give the best-fit simulated cold cal TB are 0.18° and -0.21°, respectively. WindSat scans from right to left and is located on the forward-looking side of the satellite, so the sign convention for the azimuth angle is +34° at scan position 1 and -34° at scan position 80. The negative roll offset implies that the EIAs should be higher on the right side of the scan compared to the left side, as can be seen in Figure 3.20.

The EIA variability is due primarily to pitch and roll offsets. The oblateness of the Earth contributes <0.01° to changes in the EIA across the scan, which is insignificant

when compared to the contribution of pitch and roll offsets to the EIA variability. It is still important, however, to include the Earth oblateness in the model because the changing radius with latitude affects the EIAs throughout the satellite orbit.

The derived pitch and roll offsets found here closely agree with independent pitch and roll offsets of 0.18° and -0.16°, respectively, found using a geolocation technique [67].

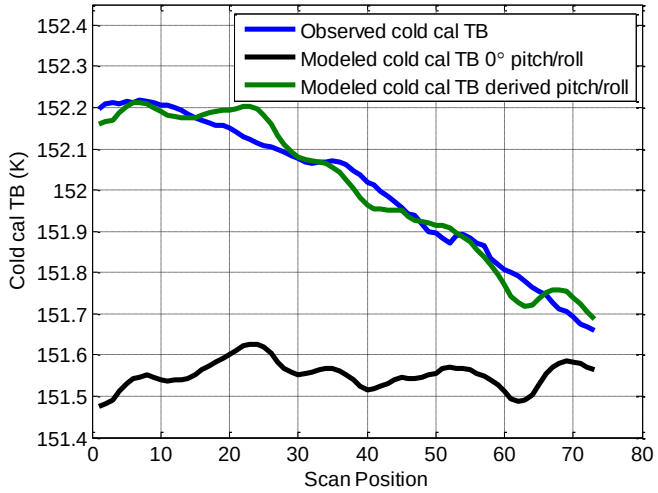

Figure 3.19: Modeled cold cal TB at 0° pitch/roll with modeled cold cal TB at a pitch of 0.18° and roll of -0.21° compared with the observed cold cal TB for the WindSat 10.7V GHz channel.

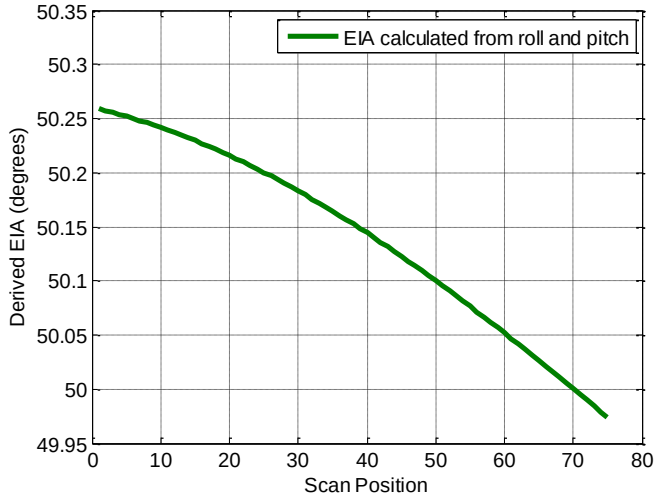

Figure 3.20: EIA across the scan for a derived pitch of 0.18° and roll of -0.21° for the WindSat 10.7V GHz channel at an altitude of 830 km.

3.5 Summary

The vicarious cold calibration single difference was introduced. The single difference takes the difference between the cold cal TB derived from a radiometer's observations and the cold cal TB derived from simulated TB data generated with an RTM. The single difference was shown to reduce the dependence of the cold cal TB on geophysical and EIA variability, thereby creating a more stable calibration reference.

Challenges associated with using vicarious cold calibration at frequencies near 90 GHz were mitigated by using the single difference to develop filters to remove TBs associated with hydrometeor scattering. Filters using combinations of high/low frequencies were determined the easiest and most suitable to implement.

The single difference was shown to be useful in determining the pitch and roll offsets of a satellite with a radiometer onboard. This method was validated by showing that it gives similar pitch and roll offsets as a different method that uses geolocation.

Chapter 4
Vicarious Cold Calibration Double Difference Method for Inter-Calibration of Spaceborne Microwave Imagers

4.1 Introduction

An accurate inter-calibration of microwave radiometers is desirable if data from several different radiometers are to be combined in careful scientific studies. Inter-calibration provides a way to compare the measurements of one radiometer to another and adjust the absolute calibration of the instruments so that they agree. This is done by determining the calibration differences between two radiometers, one referred to as the 'reference' sensor (the instrument being compared to) and the other referred to as the 'target' sensor (the instrument being inter-calibrated). This chapter will introduce the vicarious cold calibration double difference method for use with microwave radiometer inter-calibration and show the effectiveness of the method. Examples of inter-calibration values for current spaceborne microwave radiometers will be presented, and this method will be validated by comparing the results to other inter-calibration methods.

4.1.1 Previous and Current Inter-Calibration Studies

One of the useful applications of inter-calibration is to provide long-term climate data records, since the lifetime of a single satellite is not long enough to produce these records. There are now readily available data from many microwave radiometers dating back several decades that can be used for climate studies. Having the ability to inter-calibrate these data will enable much longer climate data records than just using single

satellites without inter-comparing them.

One natural candidate for inter-calibration is the series of SSM/I instruments. The first SSM/I was launched in 1987 and, following that instrument, there have been six other SSM/I sensors launched on different platforms. The instrument design for all the sensors is identical. However, it is possible that the sensors have slightly different absolute calibrations so it is still necessary to inter-calibrate them. There have been many efforts to combine data from the various SSM/I platforms over the years into a coherent data set, e.g. [72]-[74]. One advantage of inter-calibrating data from identical instruments on different platforms is that the center frequencies are the same. However, a major disadvantage of inter-calibrating SSM/I data is that the instruments all fly on sun-synchronous satellites with different equatorial crossing times. Yan and Weng [74] used a method for inter-calibration called simultaneous conical overpasses. It relies on finding cross-over points between the different platforms, which only occur near the poles for sun-synchronous orbiters. This greatly limits the amount of available data that can be used for inter-calibration.

Inter-calibrating a sun-synchronous orbiter with a radiometer in a non-sun-synchronous, low inclination orbit, as was done by Wentz et al. [75], creates a larger potential data set of cross-over points. This is referred to as the match-up method for inter-calibration. Wentz et al. used TMI along with various SSM/I platforms and performed an inter-calibration between TMI and SSM/I. While the number of potential data points is increased using this approach, it still restricts the inter-comparison to cross-over points only.

The most recent effort to inter-calibrate the entire series of SSM/I instruments was

done by Sapiano et al. [76]. Inter-calibration offsets for the SSM/I series of instruments were calculated using SSM/I on the F13 platform as the reference radiometer. Sapiano et al. incorporate several different methods of inter-calibration including simultaneous conical overpasses as in [74], match-ups using cross-over points with TMI as in [75], and vicarious cold calibration, which is described here.

Another effort to inter-calibrate several radiometers and create a cohesive data set is the GPM mission [36]. Unlike creating a climate data record using similar SSM/I instruments, GPM uses several radiometers with differing design details that are built by many different manufacturers. These radiometers make up what is called the GPM constellation. Since the radiometers are all different, they have unique performance and absolute calibration characteristics. Each radiometer in the constellation will be used to derive rain rates. The rain rates should be consistent across all the radiometers in the constellation, and the best way to ensure that consistent rain rates are derived is to inter-calibrate the radiometers. The reference radiometer will be GMI which is scheduled to be launched on the GPM Core Observatory satellite in February 2014. This satellite will fly in a non-sun-synchronous orbit, allowing many more cross-over points with other radiometers in the constellation in order to perform the match-ups for inter-calibration.

4.1.2 Spaceborne Microwave Imagers for Inter-Calibration

The radiometers that have been used to develop inter-calibration algorithms for the GPM mission are conical scanning microwave imagers. These radiometers use frequencies from 6 to 92 GHz, with both vertical and horizontal polarization for most channels. Since TMI (and later GMI) is used as the reference radiometer for the GPM constellation, only

those channels on other radiometers that correspond to the ones on TMI/GMI are used for inter-calibration.

Typical spaceborne microwave imagers that are used for atmospheric and surface remote sensing have similar channels, but vary slightly in frequency and EIA. Table 4.1 shows the frequencies, EIAs, and orbital characteristics of past, current, and future conically scanning radiometers that have been or will be used for GPM. When inter-calibrating two radiometers, similar frequencies/polarizations are compared. The inter-calibrated channel is referred to with the following notation: 10V, 10H, 19V, 19H, 22V, 37V, 37H, 90V, and 90H.

Radiometer	**Frequency (GHz)**					**Nominal EIA (degrees)**	**Orbital Inclination (degrees)**	**Local Crossing Time (asc)**
WindSat [71]	10.7V 10.7H	18.7V 18.7H	23.8V 23.8H	37.0V 37.0H		49.9-55.3	98.7	6:00pm
TMI [26]	10.65V 10.65H	19.35V 19.35H	21.3V	37.0V 37.0H	85.5V 85.5H	53.3 (post-boost)	35	--
AMSR-E [77]	10.65V 10.65H	18.7V 18.7H	23.8V 23.8H	36.5V 36.5H	89.0V 89.0H	55	98	1:30pm
SSM/I [22]		19.35V 19.35H	22.235V	37.0V 37.0H	85.5V 85.5H	53.1	98.8	6:00pm – 9:00pm
SSMIS [78]		19.35V 19.35H	22.235V	37.0V 37.0H	91.655V 91.655H	53.1	98.9	6:00pm – 8:00pm
AMSR2 [79]	10.65V 10.65H	18.7V 18.7H	23.8V 23.8H	36.5V 36.5H	89.0V 89.0H	55	98	1:30pm
MADRAS [80]		18.7V 18.7H	23.8V	36.5V 36.5H	89.0V 89.0H	53.5	20	--
GMI [37]	10.65V 10.65H	18.7V 18.7H	23.8V 23.8H	36.5V 36.5H	89.0V 89.0H	52.8	65	--

Table 4.1: Past, current, and future conical scanning microwave radiometers used for inter-calibration. The radiometers have similar channels, but vary slightly in frequency, EIA, and orbits. The '--' symbol in the local crossing time column indicates a radiometer in non-sun-synchronous orbit which views all local times.

4.1.3 Vicarious Cold Calibration Double Difference Method

One of the inter-calibration algorithms developed for the GPM mission is the vicarious cold calibration double difference method, which is presented in this chapter. The algorithm uses vicarious cold calibration (as described in Chapter 2) along with the single difference method (as described in Chapter 3) to estimate calibration offsets between two radiometers. To estimate the vicarious cold calibration double difference, the single differences for each radiometer are first computed. The single difference is found by taking the difference between the cold cal TB (TB_{cold}) observed by the radiometer and the cold cal TB simulated using an RTM, as described in Chapter 3. Given the single differences for two radiometers A and B, where A is the target sensor and B is the reference sensor, the double difference (DD) can be computed from the difference of these two single differences according to

$$DD = \left(TB_{cold}^{A,obs} - TB_{cold}^{A,sims}\right) - \left(TB_{cold}^{B,obs} - TB_{cold}^{B,sims}\right) \tag{4.1}$$

There are two main advantages to using the vicarious cold calibration double difference method over other inter-calibration algorithms. One is that it does not require coincident or near-coincident cross-over points between the two radiometers. The simulated TBs are able to model the natural variability in the observed TBs over time and location, creating a stationary statistic through the single difference. It is therefore not necessary to match the data by time when comparing one radiometer to another with the double difference method. Another advantage is that it is less sensitive to errors in the RTM and modeled atmosphere inputs. For example, if the surface emissivity model has an error associated with calculating the contribution of surface wind to the emissivity, this error would be smallest with light wind which is what the vicarious cold calibration

algorithm uses. Also, the algorithm uses data where the atmospheric contribution to TB is minimal, so this decreases the error associated with the absorption model as well as the input water vapor and cloud liquid water fields to the RTM.

A flow diagram of the vicarious cold calibration double difference processing is shown in Figure 4.1.

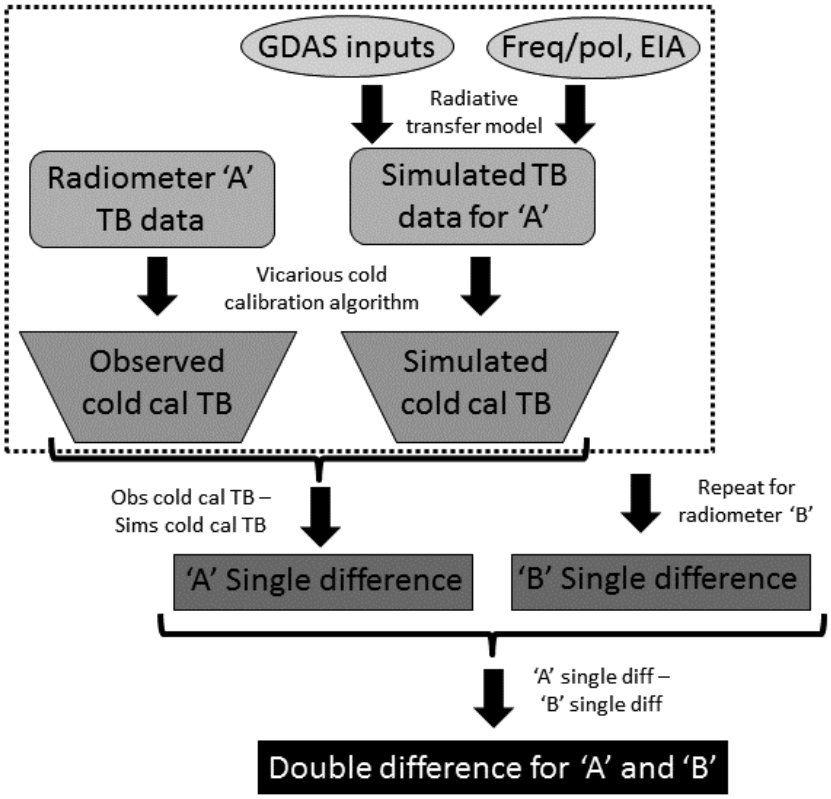

Figure 4.1: Flow diagram of the vicarious cold calibration double difference method.

4.2 Vicarious Cold Calibration Double Difference: Application to Microwave Imagers

The vicarious cold calibration double difference method is used to calculate inter-calibration offsets between two spaceborne microwave radiometers. AMSR-E data were used to calculate the cold cal TB and single difference in Chapters 2 and 3, respectively, and are used here considering it as the target radiometer to show the performance of the vicarious cold calibration double difference method. AMSR-E is inter-calibrated to TMI, the reference radiometer, since TMI is currently being used as the reference radiometer for GPM inter-calibration algorithm development.

There are nine similar channels between AMSR-E and TMI that will be inter-calibrated: the frequencies near 10, 19, 22, 37, and 90 GHz. Each includes both vertical and horizontal polarization except for 22 GHz, which only has vertical polarization. The 90 GHz channels require further filtering of the data so that the highly variable cold TBs produced from hydrometeor scattering are not included in the inter-calibration (see Section 3.3). The precipitation filter was shown in Section 3.3 to be the most effective and convenient filter so it is applied here to inter-calibrate the AMSR-E 89 GHz channel with TMI 85.5 GHz. Based on analysis of TMI data sensitivity to precipitation flag thresholds, the same TB thresholds for the AMSR-E precipitation filter as given in (2.1) and (3.1)-(3.5) are used for TMI.

One concern with inter-calibrating AMSR-E with TMI is that the two radiometers are on satellites in very different orbits. TMI is in a non-sun-synchronous low inclination orbit (35° inclination) so the radiometer only observes those latitudes between approximately 40°S and 40°N. The AMSR-E inclination, on the other hand, provides global coverage. Furthermore, since TMI is in a non-sun-synchronous orbit, it observes

all local times. AMSR-E is in a sun-synchronous orbit so its observations are all made at nearly the same local time. The match-up method of inter-calibration accounts for the differences in orbits by using near simultaneous and co-located cross-over points between two radiometers. Ideally, the vicarious cold calibration double difference method of inter-calibration does not need to filter the data to be matched either temporally or spatially, since it relies on finding a stable cold point that should be stable regardless of spatial or temporal sampling. This hypothesis will be analyzed here.

This section will first apply the vicarious cold calibration double difference method to inter-calibrate AMSR-E with TMI without accounting for any differences in orbits between the two instruments. An analysis is then performed to determine whether the differences in orbits have to be accounted for, which means that further filtering of the data needs to be done, or if the vicarious cold calibration double difference method is able to account for these differences without the need to filter the data spatially or temporally.

4.2.1 Inter-Calibration of AMSR-E with TMI

There are nine channels to be inter-calibrated for AMSR-E and TMI: the 10, 19, 37, and 90 GHz channels which include both V- and H-pol and the 22 GHz channel with just V-pol. The TMI single difference is calculated and the double difference is found using the AMSR-E single difference from Chapter 3. The result of this is shown by month for all nine channels in Figure 4.2, V-pol on the left and H-pol on the right. The double difference is calculated as AMSR-E minus TMI. Assuming that the single difference is able to account for discrepancies in frequency, EIA, and orbits between the two

radiometers as well as geophysical effects present in the cold cal TB, the values for each channel shown in Figure 4.2 should then just be the calibration offset between ASMR-E and TMI. However, it appears that there is a slight seasonal cycle in the double difference. For purposes of evaluating calibration offsets between radiometers, the presence of a seasonal cycle is undesirable. This cycle most likely suggests that some geophysical effect is not being properly accounted for in the simulations and the underlying reason must be evaluated.

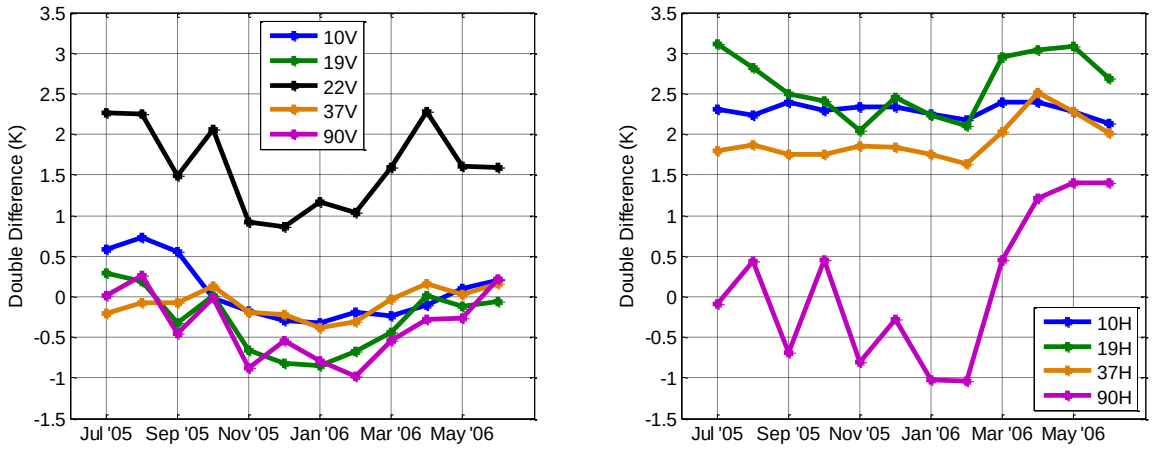

Figure 4.2: AMSR-E - TMI double difference by channel and month for July 2005 - June 2006.

Another way to look at the double difference is to separate it into ascending (asc) and descending (des) orbits for the sun-synchronous target radiometer. This helps to determine if the simulations properly account for diurnal variability. As a sun-synchronous orbiter, AMSR-E only observes two local times: 13:30 on the ascending node and 01:30 on the descending node. As stated before, TMI is in a non-sun-synchronous orbit and observes all local times. The cold cal TB is calculated separately for the ascending and descending orbits of AMSR-E but both orbits of TMI data are used to calculate the cold cal TB. The double difference as shown in Figure 4.2 is then just the

average of the ascending and descending double differences for AMSR-E. By taking the difference between the ascending and descending double differences, it can be seen if the single difference properly accounts for the fact that AMSR-E does not observe all local times. Figure 4.3 shows the difference between the ascending and descending DD for each channel, averaged over the 12 months of DDs.

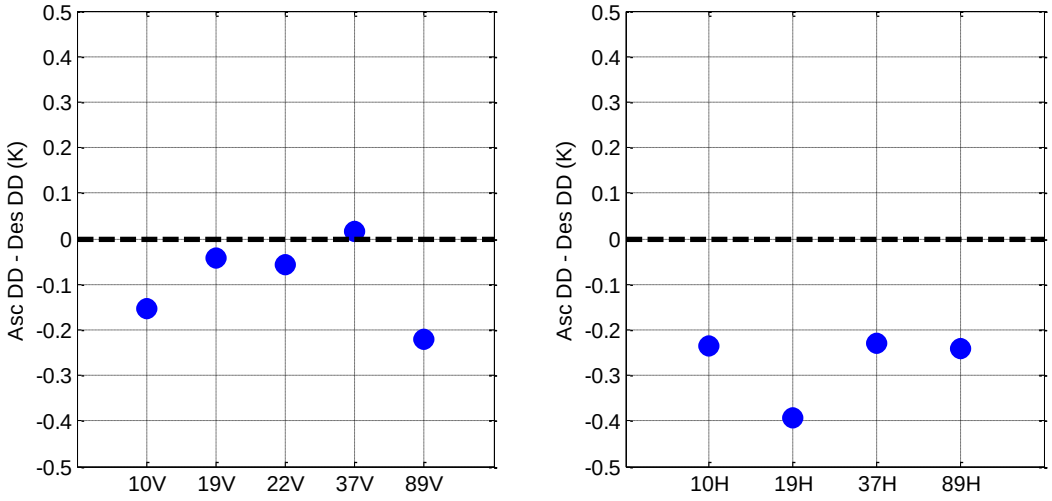

Figure 4.3: Ascending - descending double differences for AMSR-E - TMI. The descending orbits give a slightly higher double difference value than the ascending orbits for most channels, especially H-pol.

One reason for a difference between the asc and des DDs is that the simulations are not able to account for diurnal variability. A deviation from zero would then indicate that the RTM is not able to properly model the diurnal variability in the cold cal TB. A second reason for a difference in the asc and des DD is that the environment of the radiometer may change as the satellite goes in and out of eclipse. This change would be reflected in a difference in the cold cal TB between the ascending and descending orbits.

From this analysis alone, it is not possible to determine whether the discrepancy in the asc and des DDs is a result of an instrumental or geophysical effect. The difference between asc/des orbits is not constant among all channels and appears to be larger for the

H-pol channels. H-pol is the more sensitive polarization to wind speed variability, so this may suggest that the difference is a result of improper accounting for any diurnal variability in wind speed. If this discrepancy is instrumental in nature, then it should be included in the inter-calibration. However, if it is geophysical in nature, then it should be removed (for further discussion, see Section 4.3).

Ideally, the simulations should account for geophysical variability in the cold cal TB. This is necessary so that geophysical effects are not included in the final inter-calibration value and taken as a calibration difference. If the simulations are not able to account for diurnal or seasonal variability, this should either be corrected, or included as an error in the inter-calibration. The following analyses determine if there is a way to remove the two apparent effects of geophysical variability on the double difference: the seasonal cycle and the diurnal variability.

4.2.2 Double Difference Seasonal Cycle Analysis

The first analysis to improve the double difference is to discover the source of the seasonal cycle and attempt to remove it. Since the 22V channels on both AMSR-E and TMI are impacted the most by water vapor fluctuations and a seasonal cycle was noticed in 22V, this channel will be used as an example. A comparison of the 22V single differences for each radiometer is shown in Figure 4.4. The AMSR-E single difference has a slight seasonal cycle, while the TMI single difference for the water vapor channel has a very apparent seasonal cycle. One hypothesis for this discrepancy in the shapes of the single differences is that the GDAS inputs (i.e. the geophysical field inputs) to the RTM, especially the water vapor burden, are inaccurate. Therefore, the simulated TBs are not able to exactly model the geophysical variability in the observed cold cal TB. This

causes a problem for TMI since it is in a low-inclination orbit. AMSR-E's TB population includes the whole globe, so it is able to find the coldest TBs that lie outside ±40° latitude where the water vapor is minimal and the simulations are better able to model the observations. The TMI TB population is limited to the tropics where the water vapor burden is greatest and varies the most, which can cause instability in the cold cal TB. As identified in Chapter 2, the lower inclination of TMI could lead to a less stable cold cal TB statistic since the locations where the coldest TBs exist are outside the TMI observed latitudes. It was shown in Chapter 3 with the global AMSR-E data that the impact of geophysical effects, such as the seasonal water vapor cycle, can be reduced by using simulated TBs to model what a radiometer observes. The discrepancy in the single difference seasonal cycles presents the problem that either the TMI simulations need to be improved or the AMSR-E single difference needs to be modified to model the trend of the TMI single difference. When the AMSR-E data are filtered to match the latitudes observed by TMI (40°S to 40°N), the result is a seasonal cycle in the AMSR-E single difference that closely matches the TMI single difference trend, as seen in Figure 4.5. This improves the quality of the double difference, as seen in Figure 4.6.

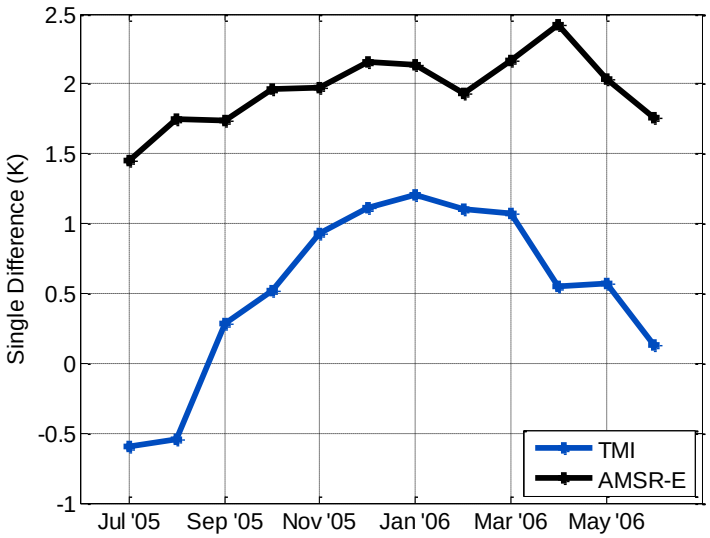

Figure 4.4: Single difference for 22V channel by month for TMI and AMSR-E. AMSR-E single difference has a slight seasonal cycle while TMI has a cycle that is a greater by a factor of two.

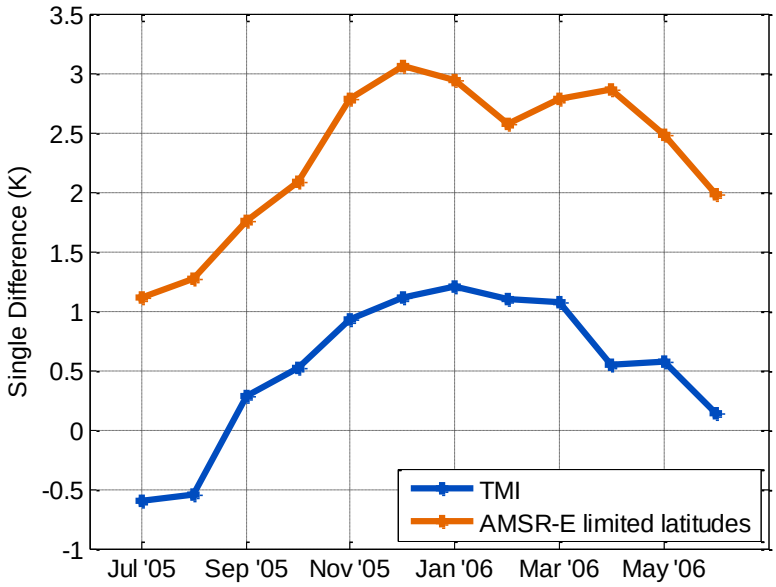

Figure 4.5: Single difference for 22V channel by month for TMI and AMSR-E using data with latitudes limited to TMI observed latitudes (40°S to 40°N). Limiting the latitudes of AMSR-E produces a seasonal cycle in the single difference similar to TMI.

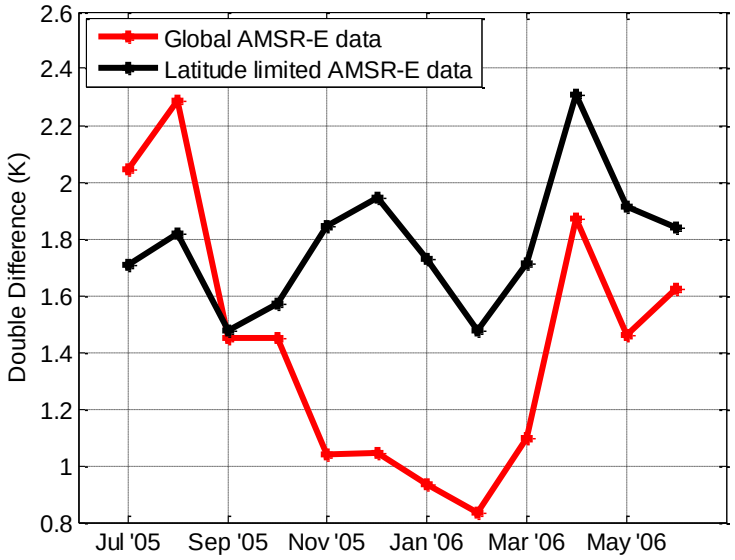

Figure 4.6: Double difference AMSR-E - TMI using all AMSR-E data (globe) compared with using AMSR-E data with latitudes limited to TMI observed latitudes. Limiting the AMSR-E data to TMI latitudes decreases the seasonal cycle of the double difference by about a factor of two.

One concern with limiting the latitudes is that the global regions change from which the cold cal TB is derived. A similar analysis as what was done in Section 2.1.1 showing the location of the 10% coldest TBs and the histograms of the wind speed, water vapor, and SSTs that contribute to the coldest 10% TBs is shown again here for limiting the latitudes of AMSR-E to ± 40°. Figures 4.7 and 4.8 show the locations of the coldest 10% TBs for 19V and 37H, respectively. The two channels show very similar locations of the coldest TBs when the latitudes of AMSR-E are limited to ± 40°. Table 4.2 gives the mean SST, water vapor, and wind speed values for the total histogram and the 10% CDF histogram for all AMSR-E channels when the latitudes are limited. The means of the SST and water for the 10% CDF histogram are slightly higher here compared with those shown in Table 2.1 using all AMSR-E latitudes, but this is because the colder SSTs and lower water vapor values do not exist in the limited latitude range. Instead, the cold

cal TB finds the lowest SST and water vapor values possible. The mean wind speed shows similar results to Table 2.1, so limiting the latitudes most likely does not change the cold cal TB sensitivity to wind speed.

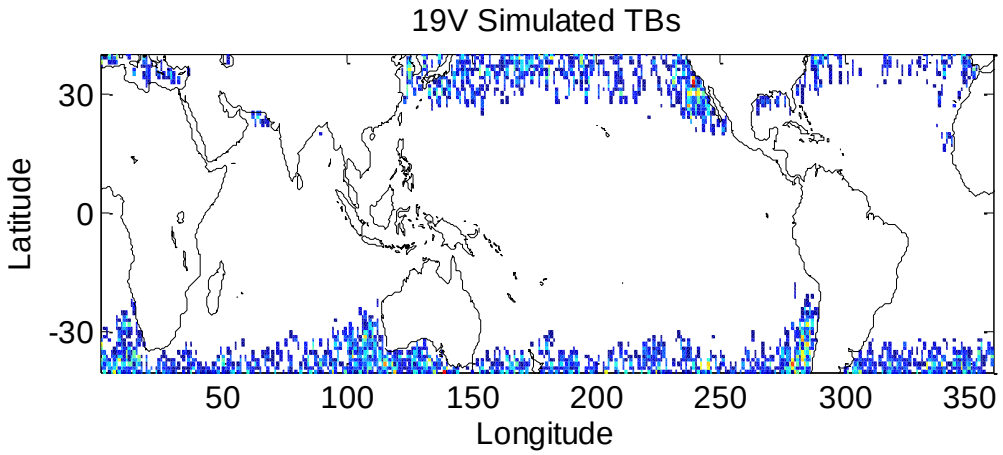

Figure 4.7: Occurrence of TBs from the lower 10% of the histogram for AMSR-E 18.7V for July 2005, limiting the latitudes to ± 40°.

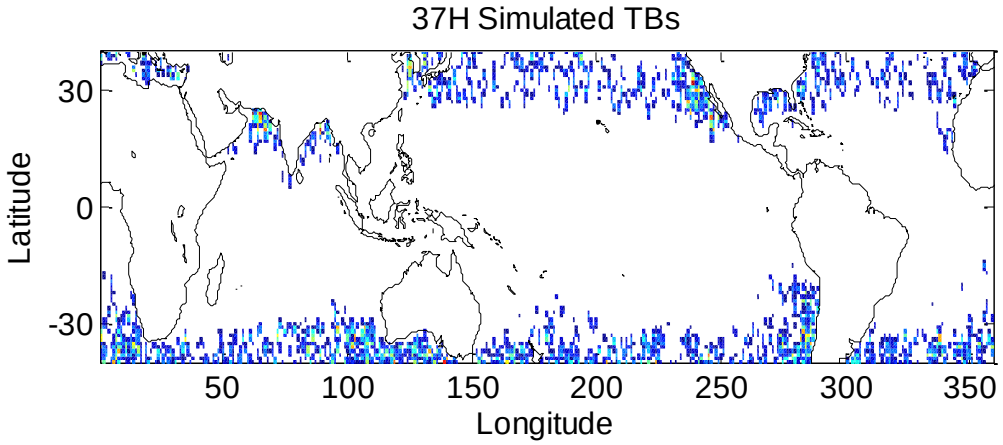

Figure 4.8: Occurrence of TBs from the lower 10% of the histogram for AMSR-E 36.5H for July 2005, limiting the latitudes to ± 40°.

		10.65V	**18.7V**	**23.8V**	**37.0V**	**89.0V**
SST (K)	Mean	297.5	297.5	297.5	297.5	297.5
	10% mean	290.4	291.2	291.6	291.6	291.4
Water Vapor (cm)	Mean	3.2	3.2	3.2	3.2	3.2
	10% mean	1.6	1.3	1.3	1.3	1.3
Wind Speed (m/s)	Mean	6.7	6.7	6.7	6.7	6.7
	10% mean	7.2	7.5	7.7	7.5	7.6

		10.65H	18.7H		37.0H	89.0H
SST (K)	Mean	297.5	297.5		297.5	297.5
	10% mean	292.7	292.0		292.5	291.7
Water Vapor (cm)	Mean	3.2	3.2		3.2	3.2
	10% mean	1.8	1.4		1.4	1.3
Wind Speed (m/s)	Mean	6.7	6.7		6.7	6.7
	10% mean	4.0	5.9		5.4	6.7

Table 4.2: Mean of the geophysical variables (SST, integrated water vapor, and wind speed) associated with the TBs for the total histogram and the 10% CDF histogram for the AMSR-E channels, limiting the latitudes to ± 40°.

The double difference for all low frequency channels is shown in Figure 4.9, using limited latitudes for AMSR-E. Table 4.3 gives a comparison between the standard deviation of the twelve month AMSR-E DDs with limited latitudes versus DDs using the full latitude range. The standard deviation gives a measure of how much the DD varies over the year, which incorporates variation due to a seasonal cycle. In all channels the double difference calculated by limiting the AMSR-E latitudes has a smaller standard deviation.

The premise of the double difference is that it should be able to remove any errors in the simulations, e.g. the water vapor fields not being accurate. However, this analysis shows that the double difference is only able to account for those errors if the radiometers being compared are limited to the same latitudes. Using the global TB population for AMSR-E results in a minimal single difference seasonal cycle, but if this single difference is used with the TMI single difference, the result is an undesirable seasonal cycle in the double difference. This means that when performing an inter-calibration of two radiometers with orbits at different inclination angles, data from the radiometer in the higher inclination orbit should be filtered to match the latitudes of the other radiometer. One other concern with TMI is that the density of the TBs are different with TMI and

AMSR-E since TMI is in a low inclination orbit and has a larger fraction of its observations between 30 and 35 degrees latitude. This is accounted for by using the simulations with the same density of TB counts with respect to latitude.

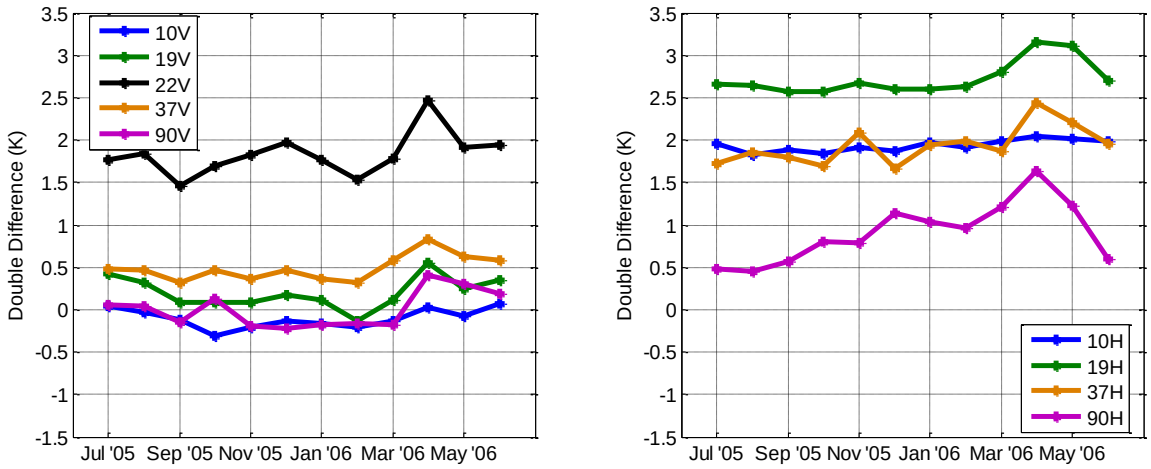

Figure 4.9: Double difference by month and channel for AMSR-E – TMI.

Standard Deviation (K)	10V	10H	19V	19H	22V	37V	37H	90V	90H
DD all data	0.20	0.13	0.35	0.35	0.49	0.17	0.31	0.46	0.68
DD limited latitudes	0.11	0.07	0.18	0.20	0.25	0.15	0.23	0.22	0.36

Table 4.3: Comparison between the AMSR-E and TMI double difference standard deviation with limiting AMSR-E latitudes versus using all AMSR-E data. Limiting the AMSR-E latitudes results in a smaller standard deviation for all channels.

4.2.3 Diurnal Sampling Effect on the Double Difference

The reduction of the seasonal cycle was achieved by filtering the AMSR-E data to include only those latitudes that TMI observes, which might help eliminate the discrepancy in the asc/des double differences in Figure 4.3. The difference between the ascending and descending DD is shown in Figure 4.10 using AMSR-E global data compared with limiting the data to ±40° latitudes.

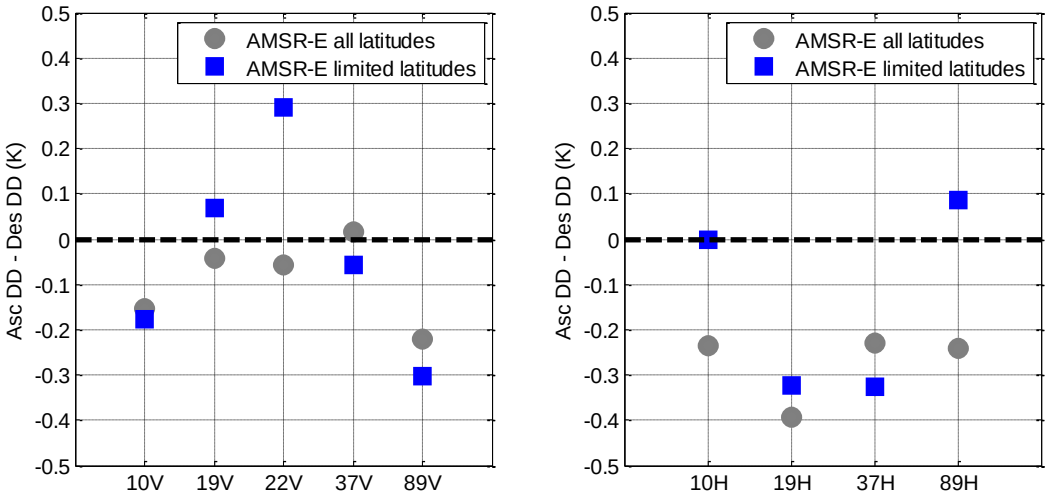

Figure 4.10: Ascending DD - descending DD for AMSR-E - TMI comparing AMSR-E all latitude data versus limiting the AMSR-E latitudes to those observed by TMI.

For some channels (e.g. 22V), limiting the latitudes of AMSR-E actually increases the difference between the ascending and descending DDs. Since it was shown that limiting the latitudes of AMSR-E results in a significant decrease in the seasonal cycle, this analysis does not necessarily mean that global AMSR-E data should be used instead. The goal of this analysis is to determine whether it matters that AMSR-E only views two local times while TMI observes all local times. To this end, TMI data are filtered to match the AMSR-E local time observations. Specifically, TMI TBs are filtered to local times from 00:00 to 03:00 to match AMSR-E descending orbits and from 12:00 to 15:00 to match the AMSR-E ascending orbits. At high latitudes, the observation times of AMSR-E move away from the nominal equatorial crossing times of 01:30 and 13:30. However, since the latitudes are filtered to ±40°, these time windows are sufficient to cover the local times observed by AMSR-E between those latitudes. The three-hour windows are chosen to give a large enough TB population to stabilize the cold cal TB statistic. The result of filtering the TMI TB data to AMSR-E local times is shown in Figure 4.11, along with the previous two results. Once again, for some channels (e.g.

90H) filtering the TMI data appears to increase the asc/des orbit discrepancy. However, for other channels (e.g. 22V and 37H), it decreases the discrepancy. The increase at 90H is most likely a result of the fact that, when the TMI data are filtered to match AMSR-E local times, much of the data are removed from the analysis. This decreases the size of the TB population that is input to the vicarious cold calibration algorithm and increases the statistical uncertainty of the cold cal TB. This would explain why there is now approximately a 0.7 K difference between the ascending and descending orbits.

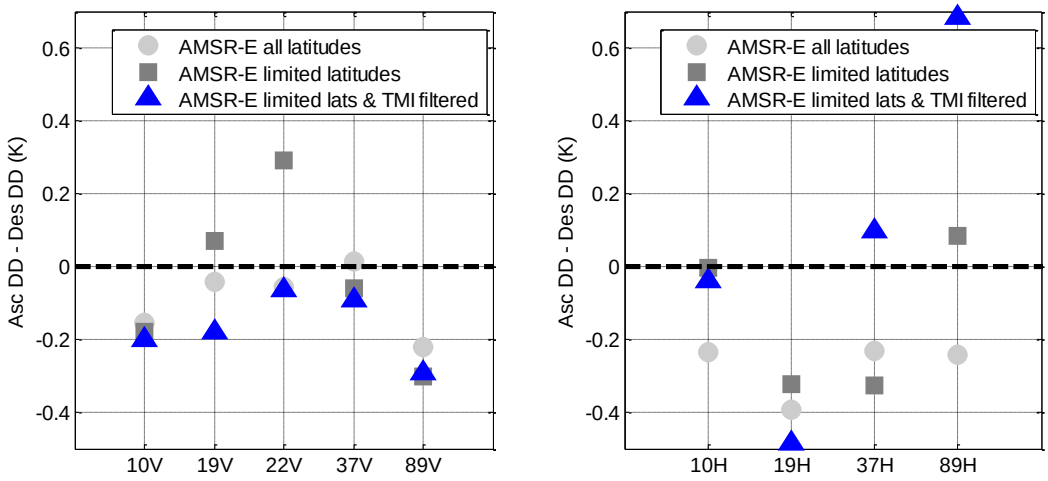

Figure 4.11: Ascending DD - descending DD for AMSR-E - TMI comparing three different filters: TMI filtered to AMSR-E local times with AMSR-E limited latitudes (triangles), AMSR-E limited latitudes to +/- 40° (squares), and AMSR-E and TMI using all data (circles).

The inter-calibration double difference value is calculated as the average of the ascending and descending orbits, which is then averaged over the 12 months. This value is used as the calibration difference between the two inter-calibrated radiometers. The effects of the spatial and temporal sampling of AMSR-E and TMI on the inter-calibration double difference value are shown in Table 4.4 for three cases of sampling. Case 1 uses all data for AMSR-E and TMI, Case 2 limits the latitudes of AMSR-E to only include data from 40°S to 40°N, and Case 3 limits the latitudes of AMSR-E and filters TMI data

to include only local times from 12:00 to 15:00 and 00:00 to 03:00. The largest differences in the DD occur going from Case 1 to Case 2. When going from Case 2 to Case 3, the largest difference is only 0.11 for 22V. Every other channel changes by 0.1 K or less, and anything less than or equal to 0.1 K is considered insignificant for inter-calibration purposes.

Double Difference (K)	**10V**	**10H**	**19V**	**19H**	**22V**	**37V**	**37H**	**90V**	**90H**
Case 1	0.02	2.31	-0.30	2.55	1.47	-0.05	1.87	-0.47	-0.06
Case 2	-0.10	1.94	0.20	2.73	1.83	0.49	1.93	0.00	0.91
Case 3	-0.13	1.84	0.24	2.69	1.94	0.47	1.83	0.02	0.92

Table 4.4: Double differences AMSR-E - TMI for 3 cases of data filtering. Case 1: Using all AMSR-E and TMI data. Case 2: Filtering AMSR-E TBs to include only those data from 40°S to 40°N. Case 3: Filtering the AMSR-E TBs to the latitude range from Case 2 and filtering the TMI TBs to include only local times from 00:00 to 03:00 and 12:00 to 15:00.

Unlike limiting the latitudes of AMSR-E, the TMI local time filter does not have a significant measureable improvement on the inter-calibration double difference value across all channels. The conclusion here is that local time filtering of the TMI data is not necessary. It does appear that there is some error associated with improperly accounting for diurnal variability in the cold cal TB, since the difference in ascending and descending orbits is not small for all channels. The effect of this error on the inter-calibration will be analyzed in the next section.

4.3 Inter-Calibration Uncertainty

One of the main contributors to the uncertainty in the vicarious cold calibration double difference method is potential inaccuracy in the RTM. The use of an RTM for inter-calibration is a key part of the algorithm since the simulated TOA TBs are used to account for differences in frequency, EIA, and orbits between the two radiometers. Two aspects of the RTM can contribute to errors in the inter-calibration: the choice of the surface/atmospheric models and the choice of the reanalysis fields which give the geophysical inputs to the RTM. The effect of the reanalysis field choice will be studied here, leaving the impact of the surface/atmosphere models for a future study.

The geophysical inputs to the RTM are not always accurate and different simulation reanalyses do not treat geophysical fields the same. Incorporating the simulations means that the inter-calibration can become sensitive to certain characteristics of the simulation reanalysis fields such as water vapor, SST, and cloud liquid water. Since the same reanalysis is used to model the TBs for both radiometers being inter-calibrated, most of the errors caused by the choice of reanalysis ideally are removed. However, this is not always the case as will be shown in this section.

The analysis in this section will compare three different simulation reanalyses and characterize the effect that each choice has on the performance of the vicarious cold calibration double difference. The three simulation reanalyses that will be used for this study are GDAS, the European Center for Medium Range Weather Forecasting Interim Reanalysis (ERA-I) [84], and NASA's Modern Era Reanalysis (MERRA) [85]. Two studies will be done here using these reanalyses: (1) how the choice of the reanalysis affects the inter-calibration and (2) how well the simulations account for both seasonal

and diurnal variability. These two factors are not entirely independent since each reanalysis can treat the diurnal water vapor signal differently. As a result, one reanalysis might show a diurnal signal in the double difference while a different reanalysis might not. Seasonal and diurnal variability in the double difference have already been addressed using GDAS as the reanalysis for geophysical inputs to the RTM (see Sections 4.2.2 and 4.2.3), and it was shown that seasonal and diurnal effects are not completely eliminated from the inter-calibration. This section will quantify the uncertainty in the double difference due to the choice of the simulation reanalysis as well as any seasonal and diurnal variability present in the double difference.

4.3.1 Double Difference Comparisons using GDAS, ERA-I, and MERRA

The double difference is calculated using geophysical inputs for the RTM from three different reanalyses: GDAS, ERA-I, and MERRA. This is done for two different radiometers: SSM/I on the F13 platform (referred to as 'F13') and AMSR-E, both using TMI as the reference. F13 and AMSR-E are on sun-synchronous platforms but view different local times. AMSR-E crosses the equator at 01:30 for its ascending node while F13 has an 18:00 ascending node.

The double difference F13–TMI is calculated using GDAS, ERA-I, and MERRA, and the results are shown in Figure 4.12 for each channel. The left plot shows the V-pol channels and the right plot shows the H-pol channels. It is clear that the H-pol channels have a greater spread in the double difference values than the V-pol channels. 22V also has a somewhat significant spread but the other V-pol channels have very little spread. This most likely indicates that there are differences in the water vapor fields among the three simulation reanalyses that the double difference is not able to account for, since

22V and the H-pol channels are most sensitive to water vapor variability in the atmosphere. Table 4.5 gives the DD values for all three simulation reanalyses, as well as the spread in the DDs (maximum DD value among the three values minus the minimum DD). The H-pol channels and 22V show the greatest spread, while the other V-pol channels all have a spread ≤ 0.1 K, which is considered insignificant for the purposes of inter-calibration.

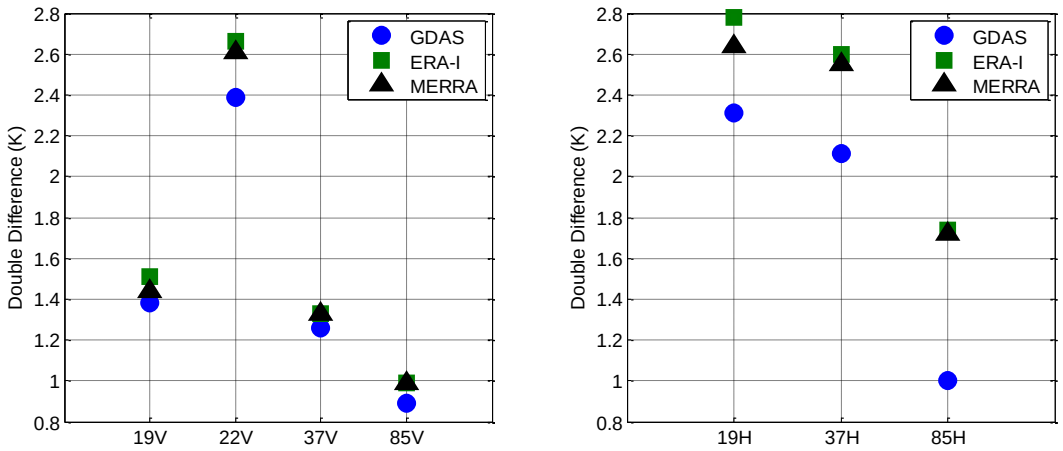

Figure 4.12: Vicarious cold calibration double difference values for F13 - TMI using three different simulation re-analysis field inputs: GDAS, ERA-I, and MERRA. The different re-analysis fields do not all give the same double difference value, implying that the double difference is not able to completely remove errors in the RTM geophysical input fields.

	19V	**19H**	**22V**	**37V**	**37H**	**85V**	**85H**
GDAS	1.37	2.31	2.39	1.24	2.09	0.95	1.02
ERA-I	1.47	2.74	2.59	1.28	2.51	0.99	1.64
MERRA	1.42	2.62	2.57	1.29	2.49	1.00	1.63
Spread	0.10	0.43	0.20	0.05	0.42	0.05	0.62

Table 4.5: Values of the F13 - TMI double difference using GDAS, ERA-I, and MERRA as simulation inputs. The spread (max DD among the three minus the min DD) is also shown. The 22V and H-pol channels show the greatest spread. 19V, 37V, and 85V channels all have a spread <= 0.1 K which is considered insignificant.

Since AMSR-E observes different local times than F13, it might be expected that the simulation reanalyses would affect the AMSR-E DD differently, if the differences

noticed for F13 are diurnal in origin. The same analysis as done for F13 is performed for AMSR-E and the results shown in Figure 4.13 and Table 4.6. Once again, the largest spreads occur for the H-pol channels of 19H, 37H, and 90H.

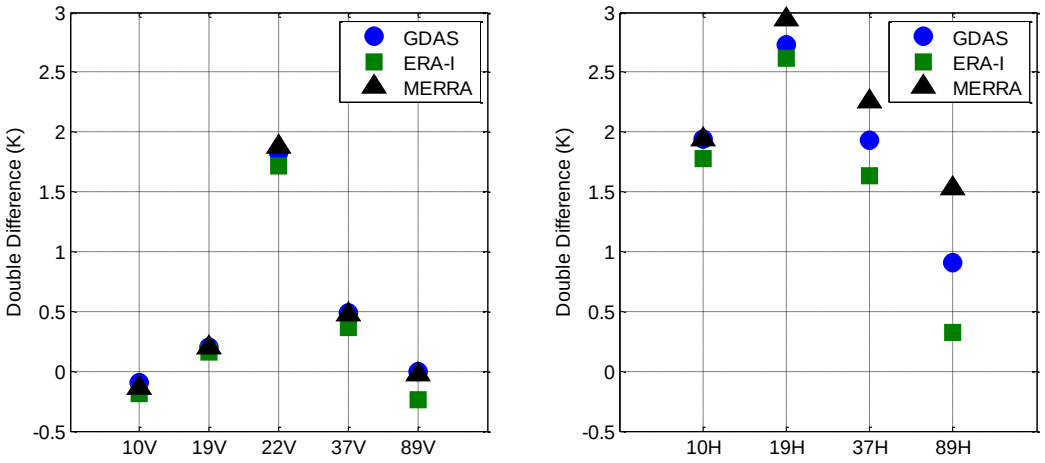

Figure 4.13: Vicarious cold calibration double difference values for AMSR-E - TMI using three different simulation reanalyses for RTM inputs: GDAS, ERA-I, and MERRA.

	10V	**10H**	**19V**	**19H**	**22V**	**37V**	**37H**	**90V**	**90H**
GDAS	-0.10	1.94	0.20	2.73	1.83	0.49	1.93	0.00	0.91
ERA-I	-0.19	1.78	0.16	2.62	1.72	0.36	1.63	-0.24	0.32
MERRA	-0.14	1.94	0.20	2.94	1.88	0.48	2.26	-0.02	1.53
Spread	0.09	0.16	0.04	0.32	0.16	0.13	0.63	0.24	1.21

Table 4.6: Values of the AMSR-E - TMI double difference using GDAS, ERA-I, and MERRA as simulation inputs. The spread (max DD among the three minus the min DD) is also shown.

4.3.2 Seasonal Cycle and Diurnal Variability in the Double Difference

The seasonal cycle present in the double difference when using all TB data for the sun-synchronous orbiter (e.g. AMSR-E) was shown to be greatly reduced when the latitudes are limited to the latitudes of the low inclination orbiter (e.g. TMI) (see Section 4.2.2). The double difference is not constant across all months, showing that there is some noise in the inter-calibration method or a residual seasonal cycle that is not removed by just

limiting the latitudes. The standard deviation of the 12 month double differences (July 2005 – June 2006) is one way to quantify the uncertainty in the inter-calibration. Tables 4.7 and 4.8 show the standard deviation of the double differences for F13 and AMSR-E, respectively, using GDAS, ERA-I, and MERRA as inputs to the simulations.

F13 standard deviation of the DD	**19V**	**19H**	**22V**	**37V**	**37H**	**90V**	**90H**
GDAS	0.19	0.17	0.24	0.14	0.22	0.29	0.26
ERA-I	0.19	0.21	0.25	0.15	0.33	0.27	0.37
MERRA	0.16	0.16	0.26	0.15	0.21	0.30	0.40

Table 4.7: Standard deviation of the F13 DDs for 12 months (July 2005 - June 2006) using the three reanalyses GDAS, ERA-I, and MERRA.

AMSR-E standard deviation of the DD	**10V**	**10H**	**19V**	**19H**	**22V**	**37V**	**37H**	**90V**	**90H**
GDAS	0.11	0.07	0.18	0.20	0.25	0.15	0.23	0.22	0.36
ERA-I	0.14	0.09	0.26	0.27	0.43	0.19	0.29	0.25	0.55
MERRA	0.07	0.07	0.16	0.22	0.35	0.17	0.26	0.29	0.58

Table 4.8: Standard deviation of the AMSR-E DDs for 12 months (July 2005 - June 2006) using the three reanalyses GDAS, ERA-I, and MERRA.

A similar analysis to the one done in Section 4.2.3 can be performed to see if the three reanalyses have different treatments of diurnal variability in the geophysical inputs, e.g. water vapor. It was determined in Section 4.2.3 that the difference between the ascending and descending DDs for AMSR-E and TMI is not zero. The difference between the ascending and descending DD is once again shown here. The DDs for ERA-I and MERRA inputs are shown as well, along with the F13 DD results to incorporate a radiometer with different local time observations. The purpose is to see if the asc/des discrepancy can be reduced with the choice of a different reanalysis for the simulations. Figures 4.12 and 4.13 show the difference between the ascending and descending DD for F13 and AMSR-E, respectively, using GDAS, ERA-I, and MERRA inputs for the

simulations. All channels for F13 except 19H show less than 0.2 K for a spread among the three reanalyses. This shows that the choice of the simulation reanalyses has very little impact on the double difference diurnal variability for F13–TMI. AMSR-E shows fairly good agreement among the three reanalyses except for 90V and 90H, where the MERRA DD appears to be an outlier.

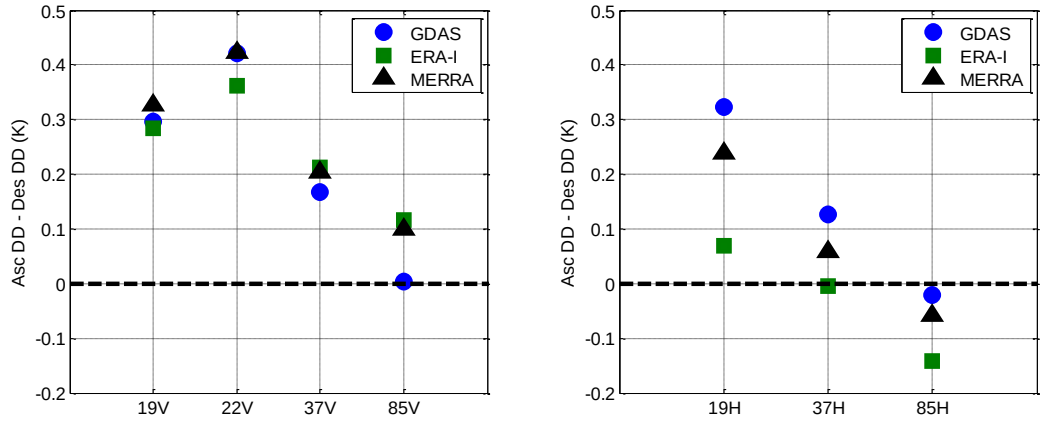

Figure 4.14: Ascending DD - descending DD for F13 – TMI using GDAS, ERA-I, and MERRA as simulation inputs. The only channel to show any significant difference among the three reanalyses is 19H which has a spread of less than 0.3 K.

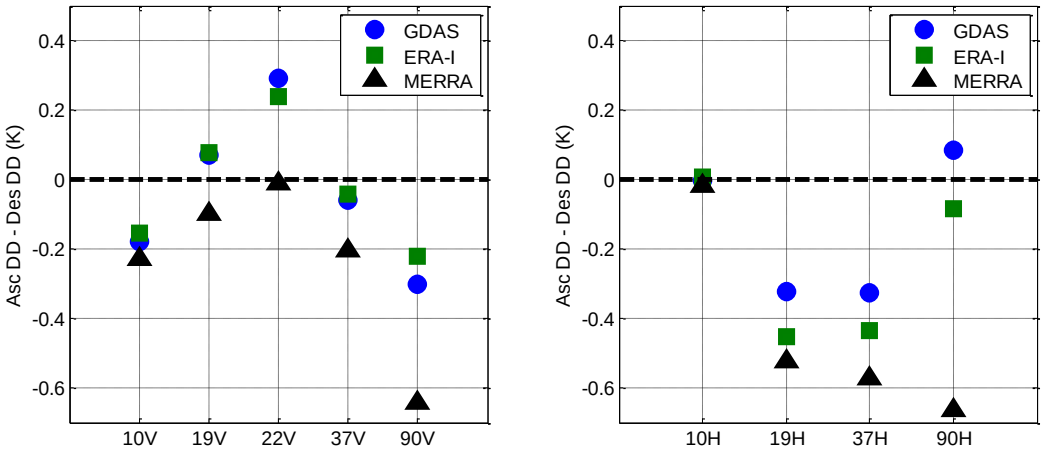

Figure 4.15: Ascending DD - descending DD for AMSR-E – TMI using GDAS, ERA-I, and MERRA as simulation inputs. GDAS and ERA-I show fairly good agreement at all channels while MERRA appears to be an outlier, especially for 90V and 90H.

As seen in Figure 4.11, filtering the TMI data to only include those local times that AMSR-E observes made no significant improvement on the double difference. However, this was done using only GDAS for RTM geophysical inputs and only AMSR-E as the target radiometer. Incorporating ERA-I and MERRA for RTM inputs as well as using F13 for the target radiometer with a different equatorial local time crossing could impact the DDs differently. One way to observe how the various reanalyses model the diurnal signal in the cold cal TB is to filter the TMI data into local times. Since TMI observes all local times, the instrument can be used to analyze the variation in the cold cal TB as a function of local time. Ideally, the simulations should be able to account for diurnal variability, but this is not the case.

TMI data are filtered into local time bins every two hours and a cold cal TB is calculated for both the observations and simulations. The single difference is then calculated for each of the three reanalyses and the results shown in Figure 4.16 for all TMI channels. This analysis is done for July 2005 – June 2006 and the results shown are averaged over the 12 months. The single difference is plotted as a difference from the mean so that the shape of the single differences of GDAS, ERA-I, and MERRA can be easily compared.

It is apparent that the simulations are not able to completely model the diurnal cycle in the cold cal TB since there is a residual signal that appears in the single difference. This diurnal signal is strongest for 22V, while 10V and 10H have no significant diurnal signal. This signal is therefore most likely a result of the simulations improperly modeling the water vapor diurnal signal and is fairly similar among the three reanalyses. Thus, all the reanalyses have approximately the same error associated with

not treating the diurnal water vapor signal properly. One potential contributor to this error is the coarse spatial and temporal resolution of the reanalyses. All three have 1° latitude/longitude spatial resolution, so small-scale water vapor fluctuations would be improperly modeled. The temporal resolution of GDAS and ERA-I is 6 hours, while MERRA gives geophysical inputs every 3 hours. However, it does not appear that having double the temporal resolution with MERRA aids in mitigating the diurnal cycle any more than GDAS or ERA-I.

The TMI local times of 01:30 and 13:30 (AMSR-E observed local times) typically fall near the peak and the minimum of the diurnal cycle. When taking the average of the minimum and maximum value of the diurnal single difference, the result is the same as when taking the average of the TMI single difference over all local times. This helps to explain why filtering the TMI data to only include AMSR-E observed local times did not have a significant impact on the double difference (see Figure 4.11). It can be inferred that filtering the TMI data to only include F13 observed local times would also have an insignificant impact on the F13–TMI double difference. F13 observes local times of 06:00 and 18:00 and the TMI single differences at those local times lie right around zero, falling approximately halfway between the maximum and minimum of the diurnal signal. Since the diurnal water vapor signal has a period of 24 hours and the sun-synchronous orbiters sample this signal every 12 hours, the diurnal signal should always average to zero when taking the average of the ascending and descending orbits. It is therefore not necessary to filter the TMI local times to match those of the sun-synchronous orbiter when performing an inter-calibration and the discrepancy between the ascending DD and descending DD is taken as an error in the inter-calibration method.

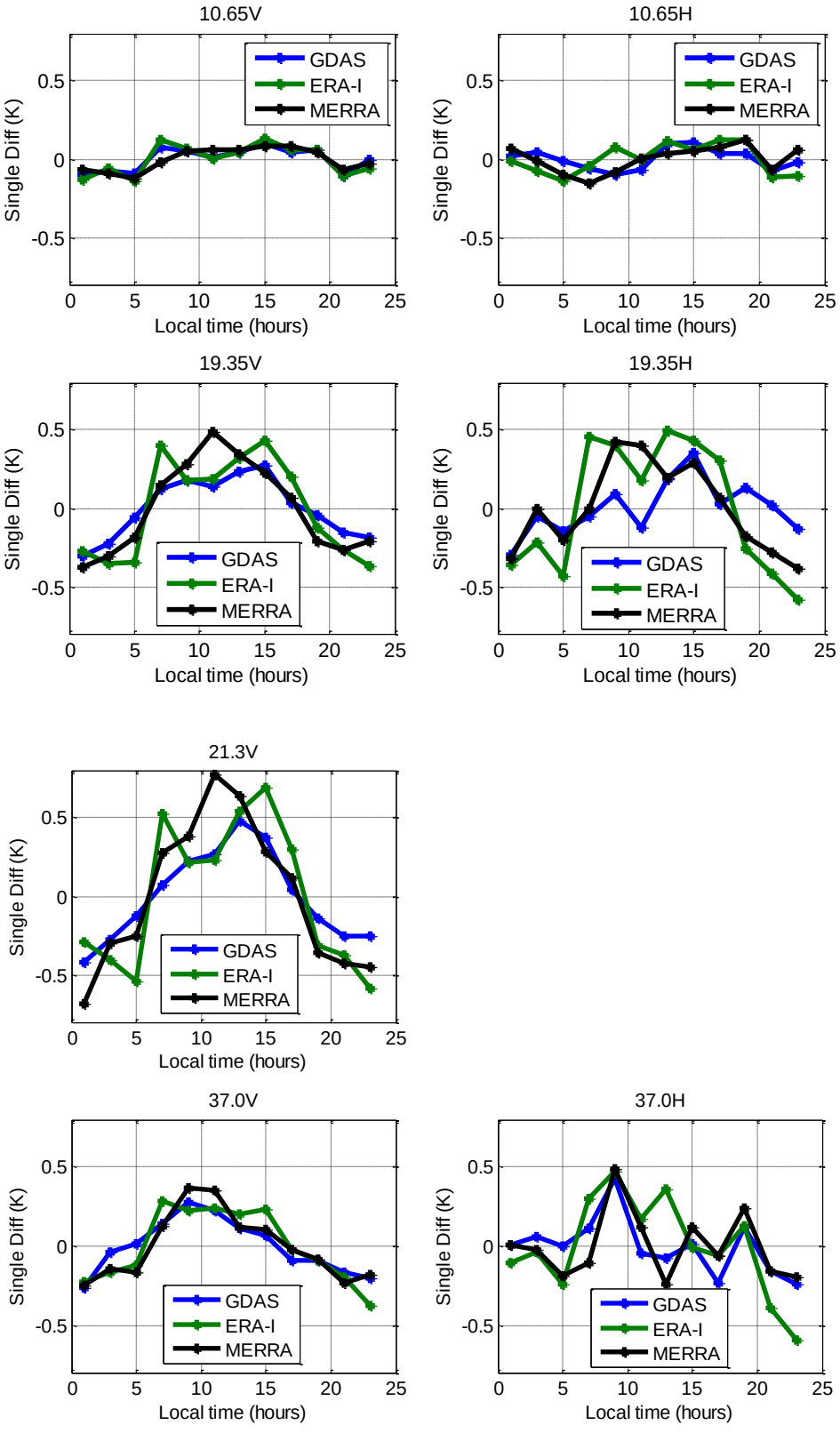
10.65V
10.65H
19.35V
19.35H
21.3V
37.0V
37.0H
GDAS
ERA-I
MERRA
Single Diff (K)
Local time (hours)
0.5
0
-0.5
0
5
10
15
20
25

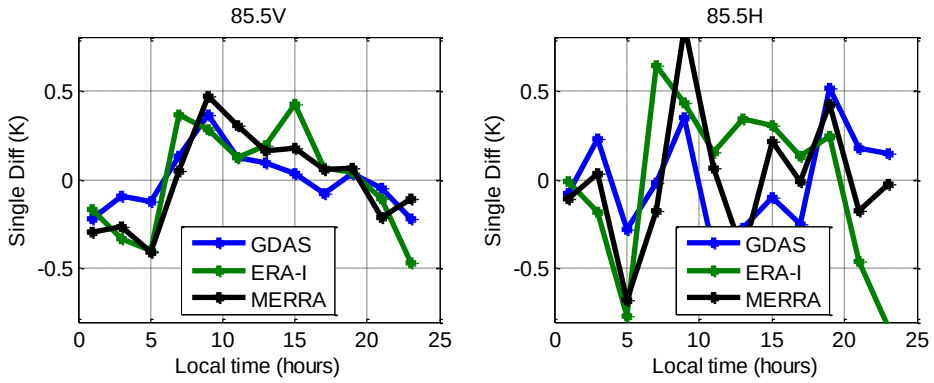

Figure 4.16: TMI single difference by local time using GDAS, ERA-I, and MERRA for geophysical inputs to the RTM. If the simulations are able to correctly model diurnal variation in the cold cal TB, the single difference should be flat across all local times but this is not the case for most channels.

4.3.3 Double Difference Uncertainty Calculation

Error bar calculations for the vicarious cold calibration double difference method should incorporate all the uncertainties identified in Sections 4.3.1 and 4.3.2. These include the variation in the double difference values depending on which simulation reanalysis is used (e.g. see Figure 4.12) as well as any remaining variation in the double difference due to seasonal and diurnal variations in the cold cal TB. The double difference value that is reported as the inter-calibration offset between the target radiometer and reference radiometer is the average of the 12 months of DDs, separated into ascending and descending orbits. This gives 24 DDs to average over. A year of data is used instead of a single month to give better statistics.

The standard deviation of the 24 DDs by channel for 12 months, split into ascending and descending orbits, includes error due to seasonal and diurnal variability that is not removed in the double difference. This is calculated for each simulation reanalysis and shown in Table 4.9.

		10V	10H	19V	19H	22V	37V	37H	90V	90H
F13	**GDAS**	--	--	0.28	0.26	0.36	0.21	0.25	0.33	0.31
	ERA-I	--	--	0.28	0.23	0.36	0.22	0.34	0.32	0.43
	MERRA	--	--	0.25	0.22	0.36	0.22	0.23	0.35	0.46
AMSR-E	**GDAS**	0.19	0.08	0.23	0.29	0.33	0.17	0.30	0.29	0.45
	ERA-I	0.21	0.10	0.29	0.39	0.47	0.22	0.40	0.30	0.61
	MERRA	0.19	0.10	0.21	0.38	0.39	0.22	0.41	0.47	0.75

Table 4.9: Standard deviation of the DD for F13 and AMSR-E using GDAS, ERA-I, and MERRA. The lowest standard deviations occur for 10V, 10H, and 37V, while the highest standard deviations occur for 22V, 90V, and 90H.

To derive an uncertainty that also incorporates the differences among the three reanalyses, the combined standard deviations among the three reanalyses is calculated according to

$$\sigma_{tot} = \sqrt{\frac{\left(\sigma_{GDAS}^2 + \sigma_{ERA-I}^2 + \sigma_{MERRA}^2\right)}{3} + \frac{\left(\mu_{GDAS} - \mu_{ERA}\right)^2 + \left(\mu_{GDAS} - \mu_{MERRA}\right)^2 + \left(\mu_{ERA} - \mu_{MERRA}\right)^2}{3}} \quad (4.2)$$

where σ_x is the standard deviation from Table 4.9 with '*x*' as GDAS, ERA-I or MERRA and μ_x is the mean of the 24 DDs for GDAS, ERA-I, or MERRA. The value σ_{tot} is then the error associated with each channel that incorporates uncertainty in the vicarious cold calibration double difference due to the simulations not being a true representation of reality. The inter-calibration difference between F13/AMSR-E and TMI, μ_{tot}, can then be calculated according to

$$\mu_{tot} = \frac{\mu_{GDAS} + \mu_{ERA} + \mu_{MERRA}}{3} \quad (4.3)$$

Table 4.10 gives the values of μ_{tot} and σ_{tot} for all channels for F13 and AMSR-E inter-calibrated to TMI. The H-pol channels typically have higher errors associated with them, with 90H having the highest error. When calculating the DD mean and uncertainty it is assumed that all three reanalyses have equal weight since it is not possible to

determine if one reanalysis is more accurate than another and would therefore deserve a greater weight.

		10V	**10H**	**19V**	**19H**	**22V**	**37V**	**37H**	**90V**	**90H**
F13	μ_{tot} (K)	--	--	1.41	2.49	2.52	1.25	2.32	0.94	1.33
	σ_{tot} (K)	--	--	0.28	0.37	0.39	0.22	0.42	0.34	0.58
AMSR-E	μ_{tot} (K)	-0.14	1.89	0.19	2.76	1.81	0.44	1.94	-0.09	0.92
	σ_{tot} (K)	0.21	0.16	0.25	0.42	0.42	0.23	0.58	0.41	1.05

Table 4.10: Double differences (μ_{tot}) and errors of the double differences (σ_{tot}) by channel for F13 and AMSR-E inter-calibrated to TMI.

4.4 Inter-Calibration Application: GPM Mission

One key application of the vicarious cold calibration double difference method is the GPM mission. The GPM mission will utilize several different microwave radiometers on individual satellites to provide global coverage of precipitation measurements. Inter-calibration of the radiometers is a key aspect of the mission, intended to ensure that consistent scientific interpretations of the measurements are made among the radiometers in the constellation. The GPM Inter-Calibration Working Group (X-Cal) is responsible for developing algorithms to inter-calibrate the radiometers included in GPM [83].

There are four teams in X-Cal who contribute to the inter-calibration algorithm for GPM: the University of Michigan (UM), Colorado State University (CSU), the University of Central Florida (UCF), and Texas A&M University (TAMU). The current GPM inter-calibration algorithm consists of inter-calibration offsets derived at a cold and warm TB to adjust radiometers in the constellation to the current reference radiometer TMI. When the GPM Core Observatory is launched, GMI will become the reference radiometer. Each group has developed individual methods to calculate inter-calibration offsets at the cold end, which are then combined into one number. Having several groups estimate inter-calibration offsets using different methods adds credibility to the inter-calibration differences if the groups attain similar results. UM is contributing to the inter-calibration algorithm by using the vicarious cold calibration double difference method as described in this chapter for the cold end and the Amazon warm calibration method for the warm end [46]. The other groups all use variations of the match-up inter-calibration method (*ref.* CSU [76], UCF [86], and TAMU [87]). X-Cal has developed inter-calibration offsets for AMSR-E, WindSat, SSM/I (F13, F14, and F15), the Advanced

Microwave Scanning Radiometer 2 (AMSR2), and SSMIS (F16, F17, and F18), each using TMI as the reference. Only AMSR2, TMI, and the SSMIS instruments are considered part of the GPM constellation since they are currently operating.

This section will present results using the vicarious cold calibration double difference method for AMSR2 and compare those results with the results from the other three groups in X-Cal. An inter-calibration difference is reported as well as the temperature at which that difference is calculated. This temperature is important for the X-Cal algorithm since it allows both a slope and offset to be calculated between the cold and warm inter-calibration differences. Having both a cold and warm tie point and calculating a scale and offset for inter-calibration is more accurate than just finding one point near the cold end and extending this constant offset to all temperatures.

AMSR2 was launched on the Global Change Observation Mission 1st-Water (GCOM W-1) in May 2012 [79]. It is the successor to AMSR-E which is no longer operating and has similar frequencies and EIAs as AMSR-E. Since AMSR2 is part of the GPM constellation, the X-Cal group obtained inter-calibration offsets for that instrument with reference to TMI using data from August 2012 to May 2013. Inter-calibration results for AMSR2–TMI from the four X-Cal group members are shown for all channels in Figure 4.17. Even though the X-Cal members have varying algorithms, especially the UM cold end method since it does not incorporate match-ups, the inter-calibration results are fairly consistent from group to group. X-Cal derives its credibility from this consistency.

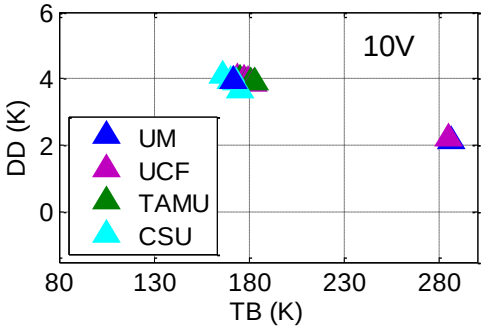
10V
DD (K)
TB (K)
UM
UCF
TAMU
CSU

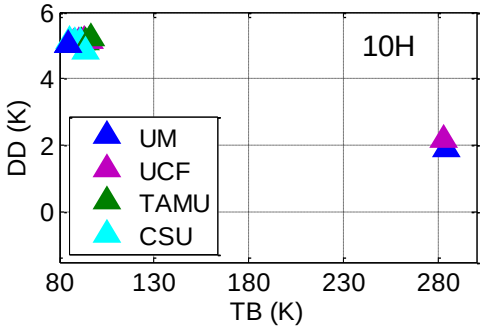
10H
DD (K)
TB (K)
UM
UCF
TAMU
CSU

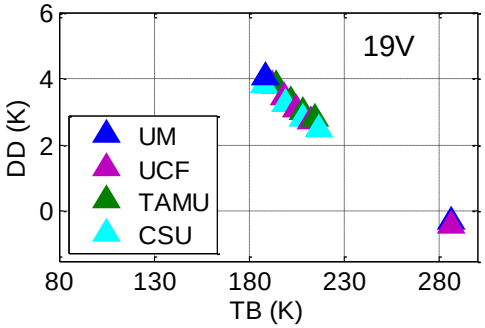
19V
DD (K)
TB (K)
UM
UCF
TAMU
CSU

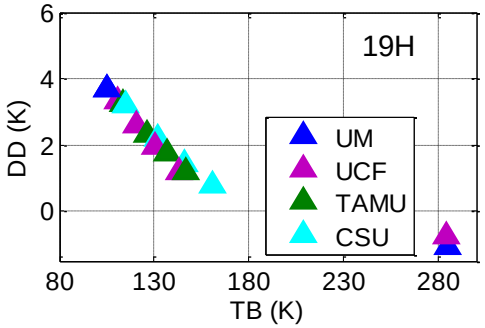
19H
DD (K)
TB (K)
UM
UCF
TAMU
CSU

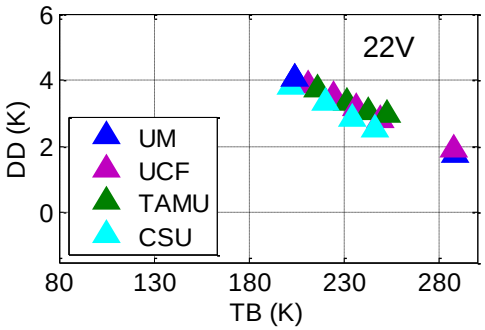
22V
DD (K)
TB (K)
UM
UCF
TAMU
CSU

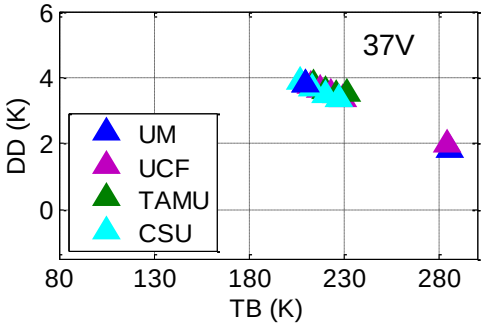
37V
DD (K)
TB (K)
UM
UCF
TAMU
CSU

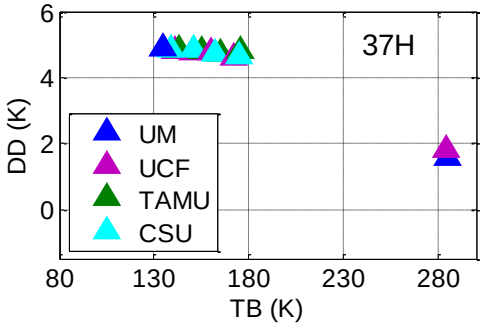
37H
DD (K)
TB (K)
UM
UCF
TAMU
CSU

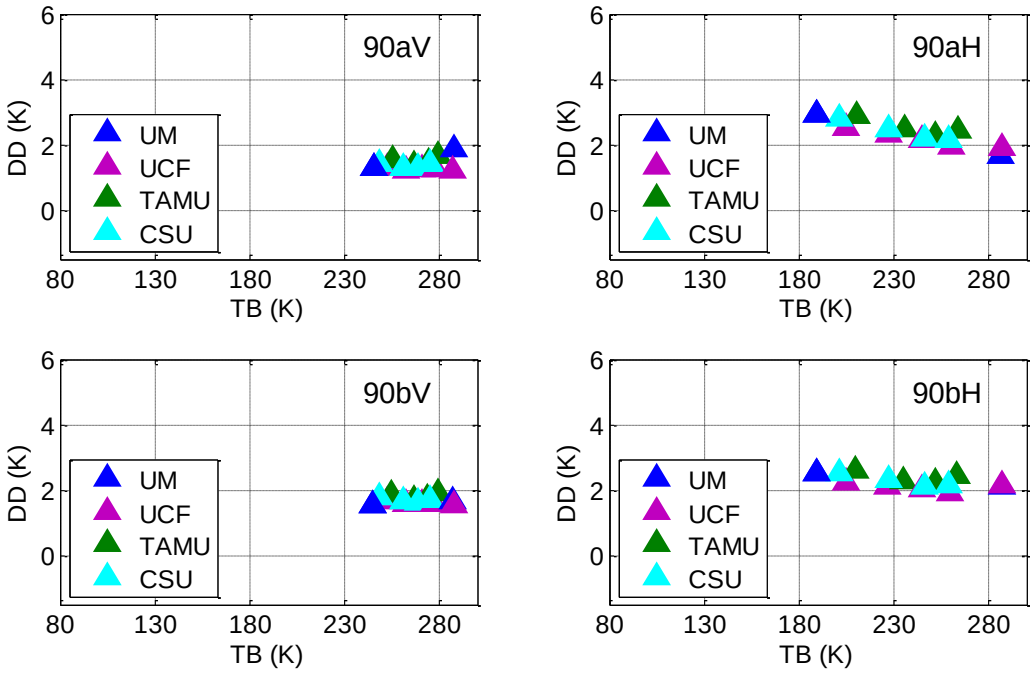

Figure 4.17: AMSR2 inter-calibration offsets with TMI as calculated by the 4 members of the GPM X-Cal group. The UM vicarious cold calibration double difference method gives very consistent results with the other methods of inter-calibration.

The AMSR2 instrument clearly shows that both a scale and offset calibration are needed in order for the measurements to be consistent with TMI for most channels. Using one tie point near the cold end and applying this calibration offset at all temperatures would result in large errors for the warmer temperatures. The vicarious cold calibration double difference method is an integral part of the X-Cal inter-calibration method, since for most channels it extends the range of known TBs to colder values. The consistency of the results using the vicarious cold calibration double difference with the other X-Cal inter-calibration methods shows that it is a valid and accurate method to be used for the inter-calibration of spaceborne microwave imagers.

4.5 Summary

The vicarious cold calibration double difference method was presented as an algorithm to inter-calibrate spaceborne microwave radiometers. The method makes use of the cold cal TB from Chapter 2 and the single difference from Chapter 3 to derive calibration differences between two radiometers that result from differences in the individual absolute calibrations.

Inter-calibration differences were calculated for AMSR-E and SSM/I F13 relative to TMI and the uncertainties in the vicarious cold calibration double difference were estimated. These uncertainties are the result of the double difference not properly accounting for geophysical (seasonal and diurnal) variability and potential errors in the geophysical inputs to the RTM.

The vicarious cold calibration double difference was calculated for AMSR2 relative to TMI and compared to results from other inter-calibration methods that are being used for the GPM mission. This method was shown to give good agreement with the other inter-calibration methods, validating vicarious cold calibration double difference as a suitable method for use with inter-calibration of spaceborne microwave radiometers.

Chapter 5
Impact of Inter-Calibration on Retrieved Rain for the Global Precipitation Measurement Mission

5.1 Introduction

Spaceborne microwave radiometers are essential instruments for the measurement of global precipitation. Since the instruments are onboard satellites, they are able to achieve measurements of precipitation over otherwise hard to reach areas (e.g. oceans) compared to *in situ* instruments or ground radar. To ensure that the precipitation derived from the radiometer measurements is accurate, the microwave radiometers need to be properly calibrated. Furthermore, if several radiometers are to be used together to derive precipitation, such as for the GPM mission, the radiometers also need to be inter-calibrated with each other to ensure that the precipitation derived from the various instruments is consistent.

The objective of this study is to determine how inter-calibrating radiometers impacts the rain rates retrieved from the radiometers. Much effort has gone into deriving calibration differences between radiometers for the GPM mission [83]. However, it is not well understood what quantitative effect the calibration differences have on the retrieved rain rates. Inter-calibration adjustments are made to the radiometer measurements to make the TBs agree as closely as possible. The level of agreement between rain estimates made by different radiometers is examined here, given the residual differences in the inter-calibration.

This chapter examines the effect of microwave radiometer inter-calibration on two of the rain products that will be produced for the GPM mission. These products are currently produced for TRMM using the PR and TMI onboard the spacecraft. Since the focus here is to study the impact of microwave radiometer inter-calibration on the rain retrievals, the products which only use TMI data for rain retrieval are examined. These precipitation products are the Level 2 2A12 instantaneous surface rain rates, the Level 3 3A11 monthly over-ocean rain accumulations, and the Level 3 3A12 monthly rain accumulations. TMI and SSM/I on the F15 platform (referred to as 'F15') are used as examples. Rain rates are first derived using the TBs from each radiometer without any inter-calibration adjustment applied. Next, the radiometers are inter-calibrated to make the TB measurements consistent. The rain rates are then re-calculated using the new TBs and the impact of the inter-calibration is examined.

The inter-calibration differences used for this analysis are given in Table 5.1. The numbers are derived using the vicarious cold calibration double difference method (cold DD), as described in Section 4.1.3, and the Amazon warm calibration (warm DD), as described in [46]. Both a cold and warm calibration difference are given so that a linear interpolation between the two temperatures can be found, as shown in Figure 5.1. The calibration differences are applied to F15 to make the F15 TBs consistent with the TMI TBs. Note that TMI calibration is not considered truth here; rather, the objective of this study is to compare the rain rates estimated by F15 and TMI, not to derive absolute rain measurements. In this case, it does not matter which radiometer is considered the calibration standard.

F15 – TMI	**19V**	**19H**	**22V**	**37V**	**37H**	**85V**	**85H**
Cold DD (K)	1.54	2.64	2.48	1.45	2.31	1.12	1.27
Cold Temp (K)	183.2	109.5	198.2	203.5	134.9	240.9	187.7
Warm DD (K)	1.71	0.88	3.32	1.54	1.62	0.83	1.19
Warm Temp (K)	287.5	285.9	287.9	283.6	283.1	285.3	284.7

Table 5.1: Inter-calibration differences for F15 - TMI at a cold temperature and warm temperature. These numbers were found using vicarious cold calibration for the cold DD and the Amazon warm calibration for the warm DD.

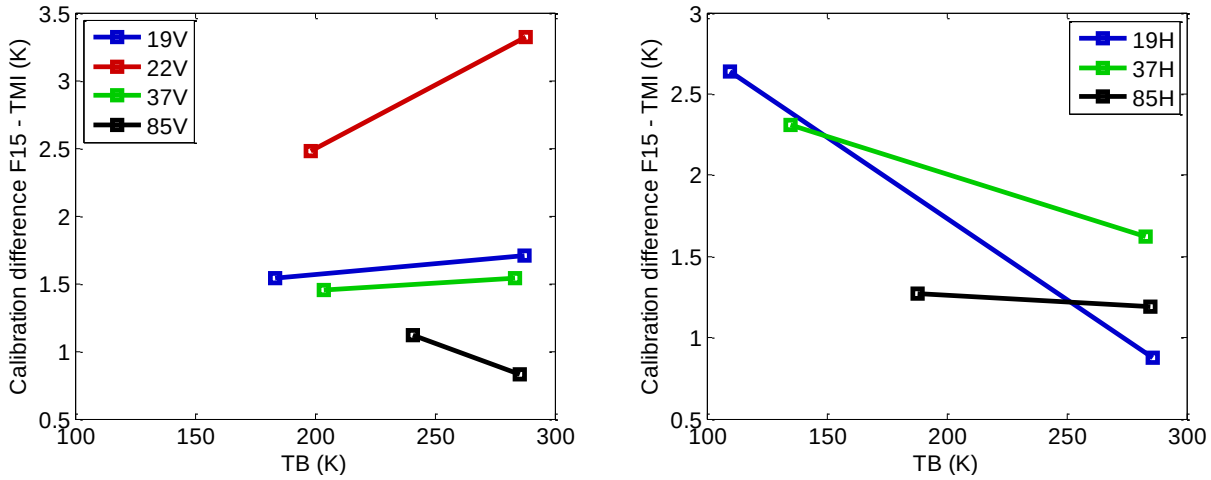

Figure 5.1: Calibration differences between SSM/I F15 and TMI for all similar channels.

5.2 Rain Retrieval using the WCC Algorithm

5.2.1 Algorithm Description

The TRMM 3A11 data product gives monthly rainfall accumulations over the ocean in 5° latitude/longitude gridded regions. Wilheit, Chang, and Chui (WCC) developed the algorithm that is used to derive the 3A11 rain accumulations [88]. The WCC algorithm was originally designed for SSM/I soon after the first SSM/I instrument was launched but was adapted for TMI so that the rainfall product could also be produced for TRMM. The algorithm makes use of just two channels to derive the rain accumulations: 19 GHz V-pol and 22 GHz V-pol. WCC operates directly on the Level 1 microwave radiometer TBs to derive the rain accumulations. Monthly histograms of the radiometer TBs are generated for the 19V and 22V channels for each 5° grid box and the freezing level is calculated using a radiative transfer model. This freezing level is then used with the histogram of a combined channel, $2*TB_{19V}-TB_{22V}$, to derive the over-ocean monthly rain accumulations. A complete description of the WCC algorithm is given in [88].

The RTM in the WCC algorithm was slightly modified from its original version for use in this study. As described in [88], the model used to derive the freezing level and rain accumulations is a parameterized version of the RTM developed by Wilheit et al. [18]. The parameterization is specific for the EIAs and frequencies of the SSM/I instrument. Since TMI has a different center frequency for the water vapor channel, as well as different EIAs, an alternate RTM was used for this study that still uses the concepts in [18] but is not parameterized for a specific radiometer. The RTM has the frequency and EIA as inputs, allowing for these inputs to be changed depending on the radiometer. This was done to ensure that the same RTM was used to derive rain rates for

both TMI and F15 so that differences in the algorithm would not contribute to differences seen in retrieved rain rates between the two instruments.

5.2.2 Rain Retrieval Results: Pre-Inter-Calibration

The WCC algorithm is applied to the TMI and F15 TBs from July 2005 to June 2006. An example of the accumulated rain for one month (July 2005) is shown in Figure 5.2 derived for TMI (top) and F15 (bottom). Since F15 is in a sun-synchronous orbit, the total rain accumulation is calculated by deriving the rain for the ascending (night) and descending (day) orbits separately and then averaging the two results to get the final rain accumulation for the month. The WCC algorithm for TMI does not distinguish between ascending or descending nodes of the satellite since TMI observes at all local times. Also, TMI only observes those latitudes roughly between 40°S and 40°N, so the F15 observations outside this latitude range are not used. TMI and F15 retrieve similar global rain features, but prior to inter-calibration, TMI retrieves significantly higher rain amounts than F15. This is most notable near the equator at the Inter-Tropical Convergence Zone (ITCZ).

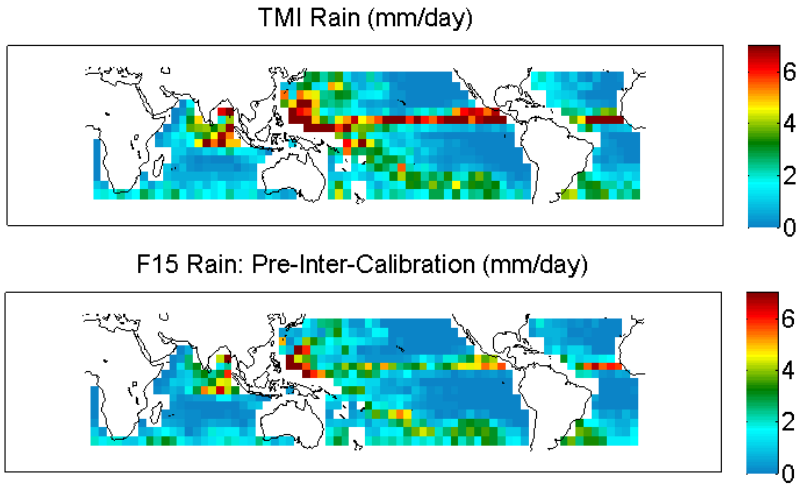

Figure 5.2: July 2005 rain accumulations for TMI (top) and SSM/I F15 (bottom). TMI appears to retrieve higher rain accumulations than F15, especially near the equator.

Figures 5.3 and 5.4 show comparisons between the TMI and F15 rain accumulations. Figure 5.3 is a zonal mean of the rain accumulation difference between F15 and TMI. This shows that the greatest differences in the rain accumulation occur near the equator at the ITCZ. The strength of the ITCZ varies depending on the season so the difference between the rain accumulations of TMI and F15 also changes with the season. Figure 5.4 is a scatter plot comparison between F15 and TMI rain accumulations for one year with each point representing one 5° box. The rain has been separated into two regions: the tropics (20°S to 20°N), and the sub-tropics (40°S to 20°S and 20°N to 40°N), since Figure 5.3 suggests that the magnitude of the rain accumulation difference changes with latitude. The black line in the figure is the 1:1 line where TMI and F15 rain accumulations are equal. TMI and F15 do not retrieve the same amount of rain, especially for high rain amounts primarily associated with the tropical region.

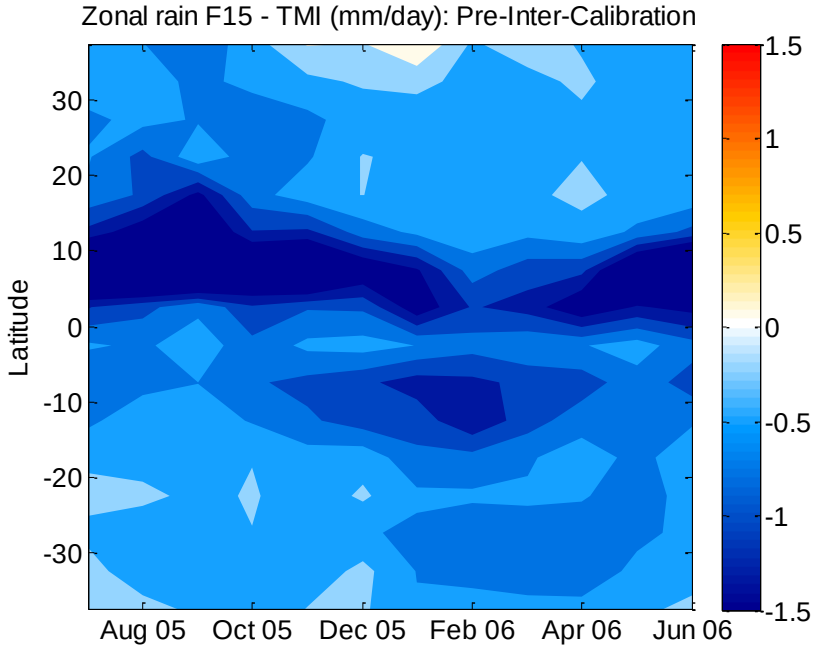

Figure 5.3: Zonal mean difference of rain accumulations for SSM/I F15 – TMI from July 2005 – June 2006. The greatest difference in rain occurs near the tropics.

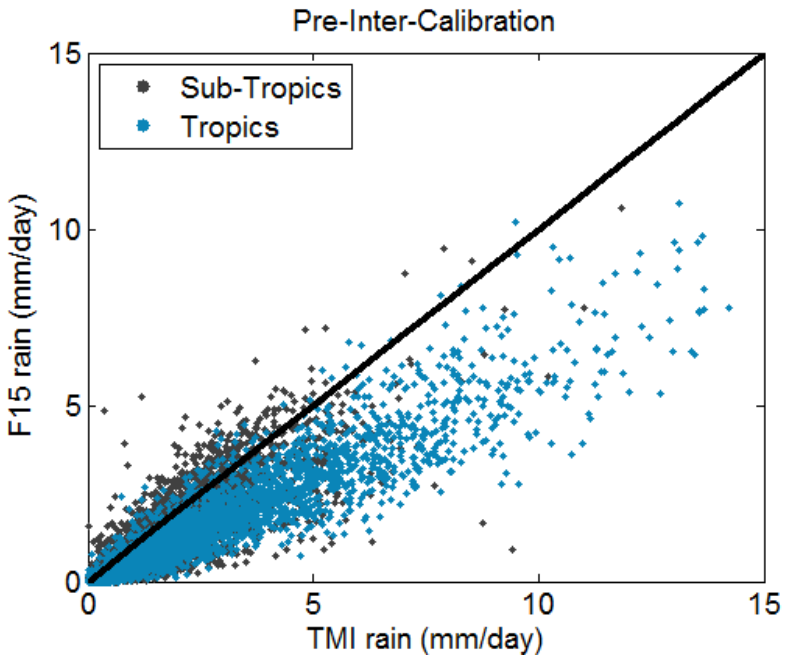

Figure 5.4: SSM/I F15 rain accumulation versus TMI rain accumulation, divided into the sub-tropics (grey) and the tropics (blue). The black line is the 1:1 line. TMI generally retrieves higher rain accumulation amounts than F15.

The conclusion from this analysis is that since TMI and F15 retrieve different rain accumulations, an adjustment needs to be made between the radiometers so that more consistent rain accumulations can be derived. The expectation is that by inter-calibrating the TMI and F15 TBs, the rain accumulations will show better agreement.

5.2.3 Rain Retrieval Results: Post-Inter-Calibration

Using a linear interpolation between the cold and warm DDs, the calibration differences from Table 5.1 are applied to the F15 19.35 GHz and 22.235 GHz V-pol TBs to adjust the F15 TBs to TMI. The WCC algorithm is then applied to the adjusted TBs for F15 and the resulting rain accumulations are compared to the TMI rain accumulations. The results are shown in Figures 5.5 and 5.6. There is a significant improvement in the agreement between the F15 and TMI rain accumulations. The large difference at the ITCZ has

decreased and the F15/TMI rain accumulation comparisons in the scatter plot lie more along the 1:1 line. There is still some discrepancy between F15 and TMI even after F15 has been inter-calibrated to TMI. It appears that the F15 TBs have not been adjusted far enough to the TMI TBs, since TMI still retrieves slightly higher rain amounts than F15 for most regions.

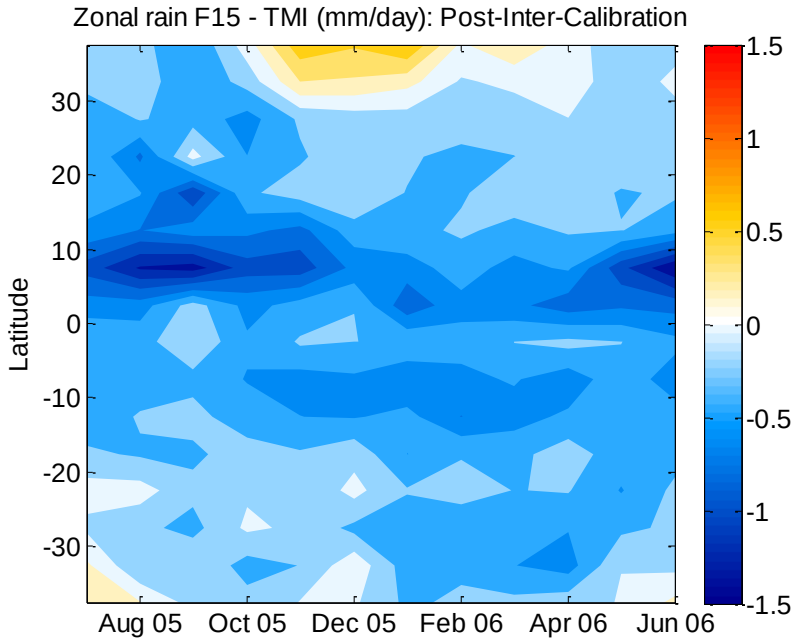

Figure 5.5: Zonal mean difference of rain accumulations for inter-calibrated F15 – TMI from July 2005 – June 2006. The large difference in the tropics has been greatly reduced.

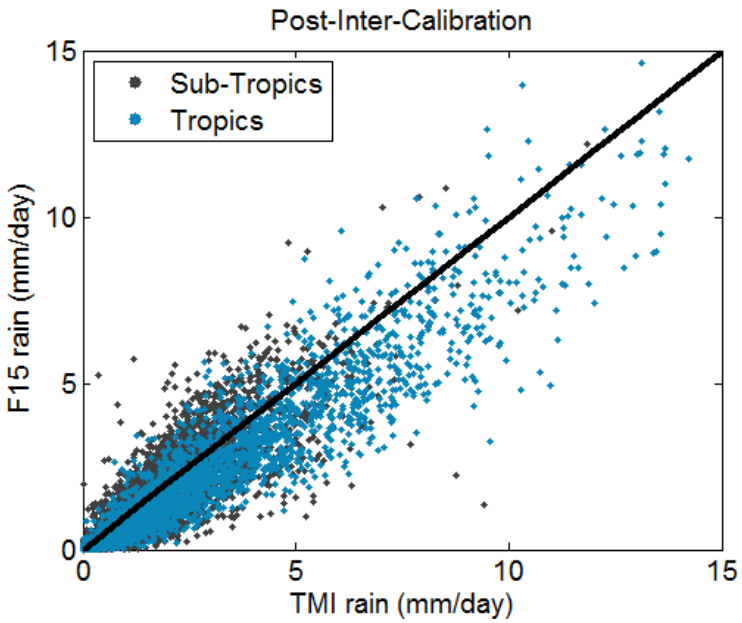

Figure 5.6: Inter-calibrated F15 rain accumulation versus TMI rain accumulation, divided into the sub-tropics (grey) and the tropics (blue). The black line is the 1:1 line. The rain accumulations show better agreement when F15 is inter-calibrated to TMI.

5.2.4 Analysis

Three separate analyses are done to quantify the difference in rain accumulations between TMI and F15. One analysis compares the rain accumulations averaged over all grid boxes and months. The average rain accumulations are grouped into three regions: the tropics (20°S to 20°N), sub-tropics (40°S to 20°S and 20°N to 40°N), and globe (40°S to 40°N). Table 5.2 shows the differences between the average rain accumulations for F15 and TMI, pre- and post-inter-calibration. All regions show a decrease in the rain accumulation difference between F15 and TMI after inter-calibration, but TMI still retrieves slightly higher rain amounts. This suggests that F15 may not have been adjusted enough to agree with TMI.

	Global avg rain difference (mm/day)	Tropics avg rain difference (mm/day)	Sub-tropics avg rain difference (mm/day)
F15 – TMI: *Pre-Inter-Cal*	-0.61	-0.85	-0.37
F15 – TMI: *Post-Inter-Cal*	-0.27	-0.42	-0.13

Table 5.2: Average rain accumulation difference (F15 - TMI) pre- and post-inter-calibration for three globe regions. All regions show a decrease in the rain difference between F15 and TMI after inter-calibration but TMI still retrieves higher rain amounts.

A second way to quantify the impact of inter-calibration on improved rain consistency is to perform a linear regression on the scatter plot of F15 vs. TMI rain accumulations. Before inter-calibration is applied, linear regression of the data gives a scale of 0.62 and offset of 0.08. When F15 is adjusted to TMI through inter-calibration, the scale increases to 0.83 and the offset decreases to 0.04. This analysis, like the first analysis with average rain accumulations, shows that inter-calibration increases the agreement between the TMI rain and F15 rain but that TMI still retrieves slightly more rain than F15. Figure 5.7 gives a graphical representation of the linear regression, where the black line is the 1:1 line and the red line is the line of best fit.

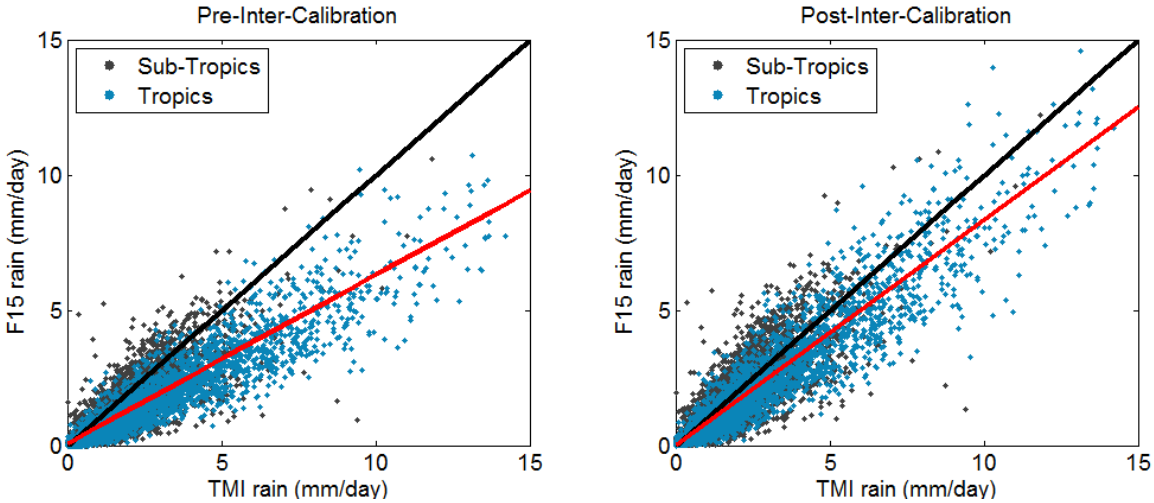

Figure 5.7: Scatter plots of F15 vs. TMI pre-inter-calibration (left) and post-inter-calibration (right) rain accumulation differences, divided into the sub-tropics (grey) and the tropics (blue). The black line is the 1:1 line and the red line is the line of best fit.

A third way to statistically quantify the rain accumulation differences is with a paired *t*-test. A *t*-test calculates the *t*-statistic, which measures the statistical significance of the differences between two data sets. The *t*-statistic is calculated according to

$$t = \frac{\left|\bar{x}_1 - \bar{x}_2\right|}{SE\left(\bar{x}_1 - \bar{x}_2\right)} \tag{5.1}$$

where *t* is the *t*-statistic and $\bar{x}_1$ and $\bar{x}_2$ are the sample means of the two sets of data, which in this case are the F15 and TMI rain accumulations. *SE* is the standard error calculated according to

$$SE\left(\bar{x}_1 - \bar{x}_2\right) = SD\sqrt{\frac{1}{n_1} + \frac{1}{n_2}} \tag{5.2}$$

where n_1 and n_2 are the sample sizes of the populations. *SD* is the pooled standard deviation calculated by

$$SD = \sqrt{\frac{(n_1 - 1)\sigma_1^2 + (n_2 - 1)\sigma_2^2}{n_1 + n_2 - 2}} \tag{5.3}$$

where σ_1^2 and σ_2^2 are the variances of each population. The *t*-test performed here is done on each 5° latitude/longitude grid box. The average of the rain accumulations for each box over the 12 months of rain accumulations is found for TMI and F15 separately ($\bar{x}_1$ and $\bar{x}_2$) along with the variance over the 12 months (σ_1^2 and σ_2^2). n_1 is equal to n_2, which is 12 for the number of months. Using these values, the value *t* can be calculated from (5.1) for each grid box.

To analyze what the *t*-statistic value represents, a null hypothesis is made. This hypothesis is then determined true or false based on the value of the *t*-statistic. The null hypothesis for this *t*-test is that the mean difference between TMI and F15 rain

accumulations is zero. For 11 degrees of freedom (12 months of rain accumulations), a *t*-statistic greater than 2.20 means there is a statistically significant difference between the TMI and F15 rain accumulations with 5% significance and the null hypothesis is rejected (i.e. TMI and F15 rain accumulations are not equal). A similar test was performed by Chang et al. to compare rain accumulations from SSM/I and TMI [89]. Figure 5.8 shows the *t*-statistic results of this analysis for F15 (top) and F15 inter-calibrated to TMI (bottom). For F15 without inter-calibration, the percentage of grid boxes that reject the null hypothesis is 13.1% (87 out of 665) while only 1.5% (10 out of 655) of grid boxes for F15 inter-calibrated reject the null hypothesis. Figure 5.8 also shows that overall the t-statistic for F15 inter-calibrated is lower than that prior to inter-calibration. This analysis further confirms that inter-calibrating F15 to TMI increases the consistency of the rain accumulations derived from each radiometer.

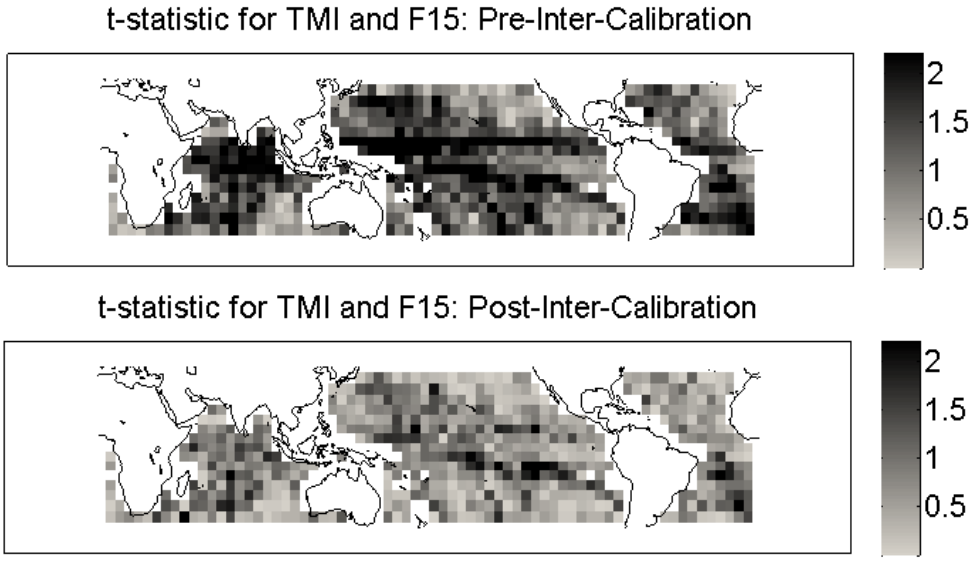

Figure 5.8: t-statistic values for TMI/F15 (top) and TMI/F15 inter-calibrated (bottom). 13.1% of grid boxes reject the null hypothesis for F15 unadjusted while only 1.5% reject it when F15 is inter-calibrated to TMI.

5.3 Rain Retrieval using the GPROF 2010 Algorithm

5.3.1 Algorithm Description

The second rain retrieval algorithm considered is the Goddard Profiling algorithm (GPROF) which produces the TRMM 2A12 and 3A12 data products. GPROF is a Bayesian retrieval method that derives instantaneous rain rates using an *a priori* database [90],[91]. The most recent version of the algorithm is GPROF 2010 (G10), which uses observations from TRMM's PR as the *a priori* database [92]. The G10 algorithm is also able to derive rain rates for SSM/I, SSMIS, AMSR-E, and AMSR2.

The 2A12 product gives instantaneous rain rates in mm/hr for all radiometer pixels. 3A12 integrates these instantaneous rain rates into gridded latitude/longitude boxes and derives monthly rain accumulations. Unlike the WCC algorithm, G10 incorporates all channels on TMI and F15, not just the 19V and 22V channels. F15 lacks a 10 GHz channel so the G10 algorithm is not able to use that frequency for retrieval, whereas the TMI rain retrieval algorithm does use the 10 GHz channel. The G10 algorithm includes retrievals for both over-ocean and over-land, but for purposes of comparison to the WCC algorithm only over-ocean rain rates are considered in this analysis. The impact of inter-calibration is considered here for the Level 3 product (gridded monthly rain accumulations).

5.3.2 Rain Retrieval Results: Pre-Inter-Calibration

The Level 2 rain rates are binned into 5° grid boxes for each month from July 2005 to June 2006. The average of all the rain rates that fall into each box is taken to give a Level 3 rain accumulation product similar to the one produced using the WCC algorithm from Section 5.2. Figure 5.9 shows an example of the G10 rain accumulations for July 2005.

Similar rain features as those seen in Figure 5.2 appear in Figure 5.9 (e.g. heavier rain accumulations just north of the equator), but there is not as noticeable a difference between the TMI and F15 rain accumulations as was seen with the WCC algorithm.

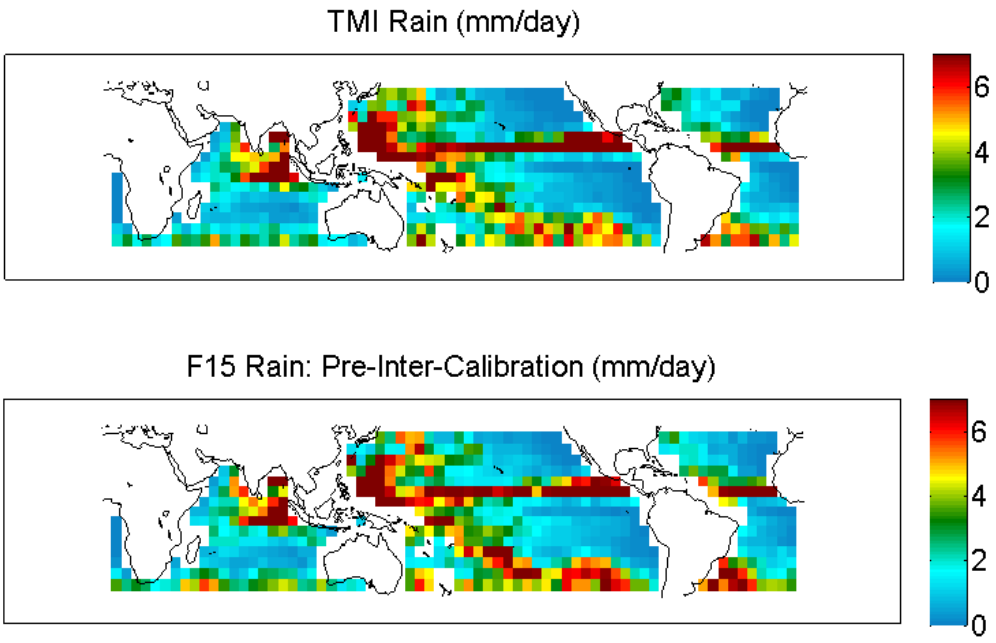

Figure 5.9: July 2005 rain accumulations for TMI (top) and SSM/I F15 (bottom).

Figure 5.10 shows the difference between F15 and TMI retrieved zonal mean rain by month. The difference is not nearly as large as that using the WCC algorithm for Level 3 rain accumulation (see Figure 5.3). Note that the scale has been restricted to a smaller range in order to emphasize important features. The ITCZ is still a prominent feature, showing that the greatest difference between F15 and TMI rain occurs near the equator. For the most part, TMI retrieves higher rain amounts than F15 (as was also noticed for the WCC algorithm), except in some places around the subtropics, most noticeably north of 30°N between October and January. Figure 5.11 gives the scatter plot for F15/TMI rain comparison. It is not immediately obvious from the scatter plot that the

rain accumulations of F15 and TMI disagree. The rain accumulations appear to be centered around the 1:1 line.

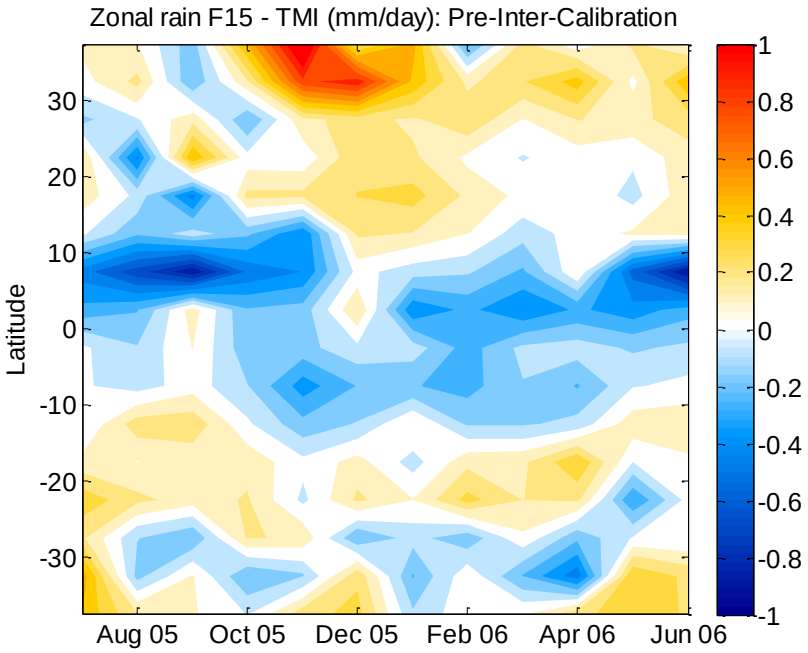

Figure 5.10: Zonal mean difference of rain accumulations for SSM/I F15 – TMI from July 2005 – June 2006. The difference is not nearly as large as the difference using the WCC algorithm for Level 3 rain accumulation.

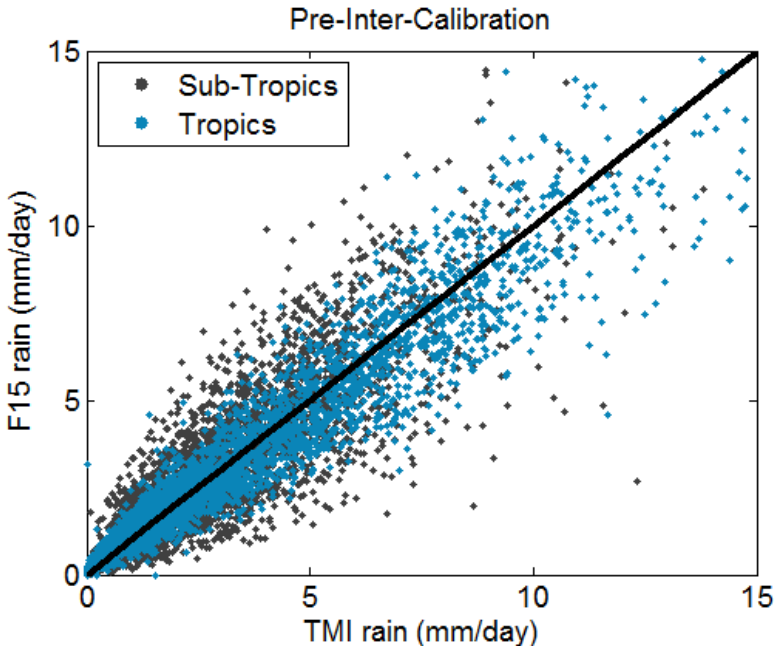

Figure 5.11: SSM/I F15 rain accumulation versus TMI rain accumulation. The black line is the 1:1 line. It appears that TMI and F15 retrieve fairly similar rain accumulations with some scatter.

5.3.3 Rain Retrieval Results: Post-Inter-Calibration

Inter-calibration is applied to the F15 TBs to make the TB measurements consistent with those of TMI and the rain accumulations are re-calculated using the inter-calibrated F15 TBs. The inter-calibrated zonal mean rain accumulation differences are shown in Figure 5.12. There is a noticeable improvement in the rain accumulation consistency for the regions around the equator at the ITCZ. The F15 vs. TMI rain accumulation scatter plot is shown in Figure 5.13, but there does not appear to be much change from the pre-inter-calibration scatter plot.

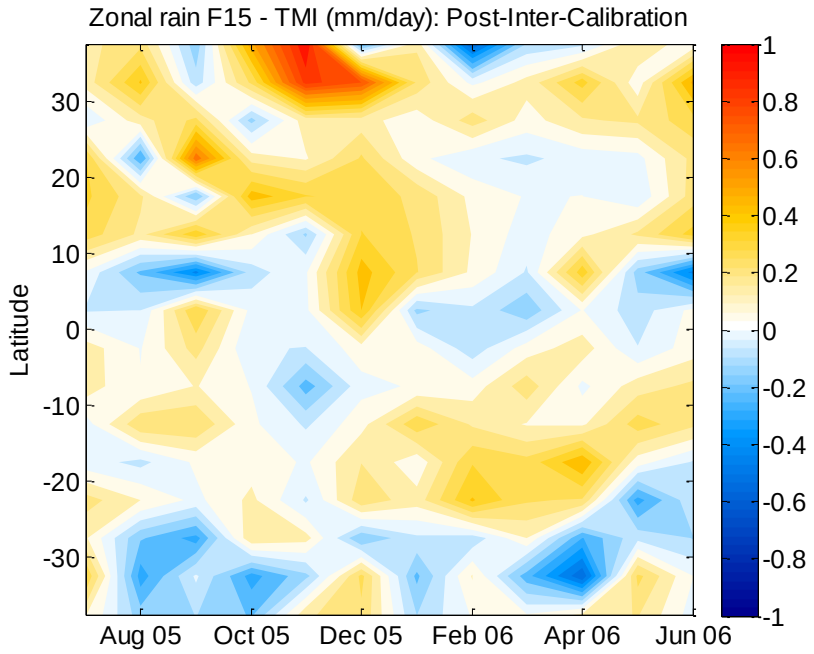

Figure 5.12: Zonal mean difference of rain accumulations for SSM/I F15 intercal – TMI from July 2005 – June 2006. There is a noticeable improvement in the consistency of rain accumulations near the equator.

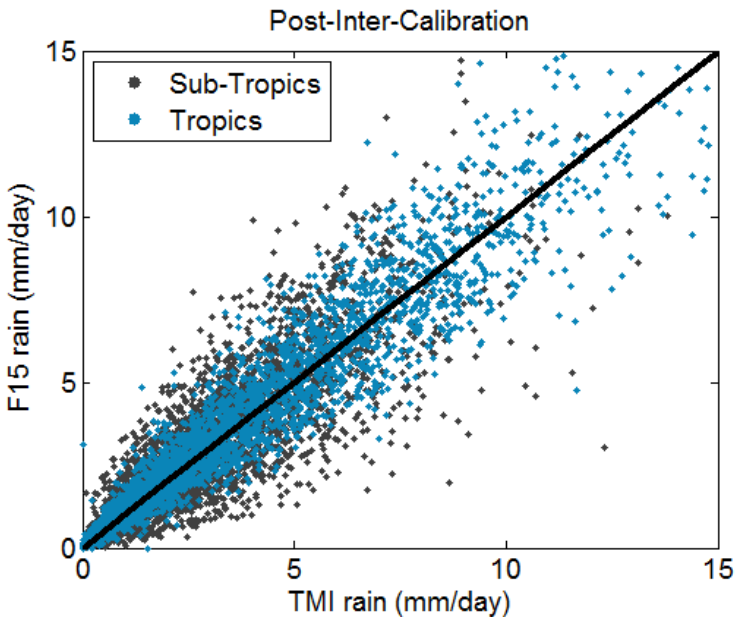

Figure 5.13: Inter-calibrated SSM/I F15 rain accumulation versus TMI rain accumulation. The black line is the 1:1 line. The rain accumulations do not appear to shift much from the pre-inter-calibration scatter plot.

5.3.4 Analysis

The same three analyses as were done with the WCC rain accumulation results are performed for the G10 rain accumulations. First, the line of best fit is found for the scatter plot data and the scale and offset are calculated for each case. The scatter plots with the lines of best fit overlaid are shown in Figure 5.14. The left plot shows F15 versus TMI pre-inter-calibration and the right plot shows F15 versus TMI with F15 inter-calibrated to TMI. The black line is the 1:1 line and the red line is the line of best fit to the data. Before inter-calibration, the line of best fit gives a scale of 0.91 and an offset of 0.29. After inter-calibration, the scale increases to 0.96 and the offset decreases to 0.20. This shows that there is a slight improvement in rain accumulation consistency when F15 and TMI are inter-calibrated.

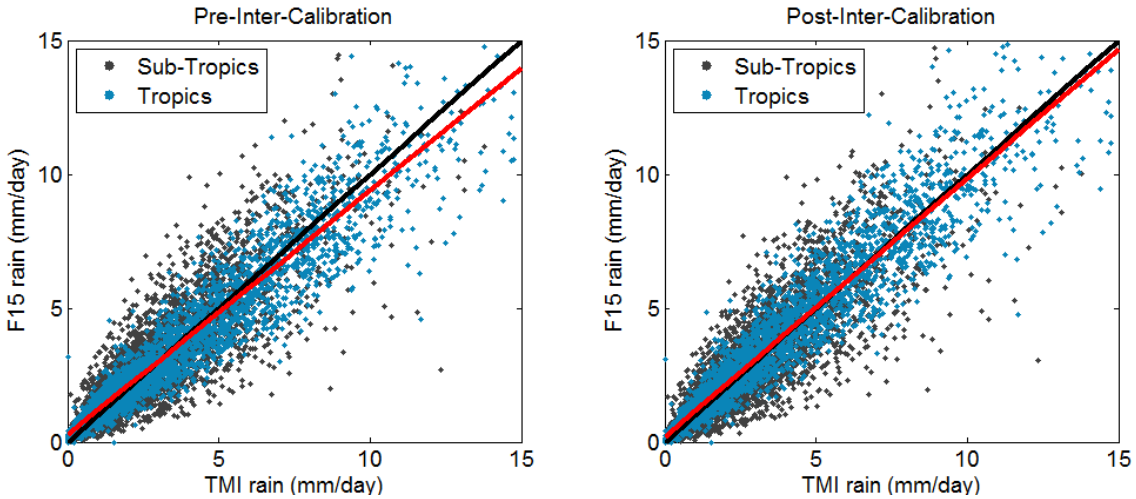

Figure 5.14: Scatter plots of F15 rain accumulations compared with TMI (left), and F15 inter-calibrated rain accumulations compared with TMI (right), along with the 1:1 line (black line) and the line of best fit to the data (red line). There is a slight improvement to the rain consistency when F15 is inter-calibrated to TMI.

Table 5.3 gives the average rain differences for F15 and TMI, comparing pre- and post- inter-calibration for the three regions used for the WCC algorithm in Section 5.2.4. The sub-tropics is the only region that shows an improvement in the average rain accumulation post-inter-calibration. However, the average rain difference post-inter-calibration for all three regions is about 0.1 mm/day which is still considered to be sufficient agreement between the rain accumulations.

	Global avg rain difference (mm/day)	**Tropics avg rain difference (mm/day)**	**Sub-tropics avg rain difference (mm/day)**
F15 – TMI: *Pre-Inter-Cal*	0.05	-0.05	0.14
F15 – TMI: *Post-Inter-Cal*	0.10	0.11	0.09

Table 5.3: Average rain accumulation difference for three regions: globe (all latitudes), tropics (20°S to 20°N) and sub-tropics (40°S to 20°S and 20°N to 40°N).

A *t*-test was performed on the G10 Level 3 rain accumulations as was done with WCC. Unfortunately, this *t*-test did not supply any evidence that rain consistency

increases with inter-calibration. For this study, 0.3% of the grid boxes rejected the hypothesis at the 5% significance level both before and after the inter-calibration was applied. This is most likely a result of the similarity between TMI and F15 G10 rain accumulations relative to WCC, so the *t*-test is not able to determine a significant difference between the rain accumulations.

5.4 Sensitivity of Rain Retrieval Algorithms to Cold and Warm DDs

Inter-calibration was shown to increase the rain accumulation consistency between F15 and TMI for both the WCC and G10 algorithms. The inter-calibration algorithm used both a cold and warm DD and derived a linear interpolation between the two points. This is referred to as two-point calibration and is assumed to be more accurate than a constant calibration offset at all temperatures. Typical inter-calibration algorithms that have been used in the past (e.g. [76]) rely on finding a calibration difference near the cold end and using it as a constant offset for all temperatures. This is referred to as one-point cold calibration. Another possible inter-calibration algorithm is to use the warm end DD as a constant offset for all temperatures. This is referred to as one-point warm calibration.

The sensitivity of the rain retrieval algorithm to the cold or warm end DD can be shown by comparing the rain accumulations using the two-point inter-calibration with the one-point cold and one-point warm inter-calibrations. Applying the inter-calibration adjustments to the F15 TBs was shown to affect the amount of rain derived from F15. However, it is not clear whether the rain retrieval is impacted more by the cold end DD or the warm end DD. Areas of rain over an ocean background are associated with warm TBs, typically much warmer than the TB where the cold end inter-calibration difference is found. This may indicate that the rain retrievals will be more sensitive to the warm end DD. Since the warm end DD typically has larger uncertainties than the cold end DD, the sensitivity of the rain retrieval to the cold or warm DD is important to know. If the rain accumulations are very sensitive to the warm end DD, this may suggest that more effort should be invested in deriving a warm end inter-calibration difference with smaller uncertainties.

Three inter-calibration algorithms are applied to the F15 TBs: the two-point inter-calibration as was done previously (intercal), the one-point cold end inter-calibration (intercal cold), and the one-point warm end inter-calibration (intercal warm). Rain accumulations for F15 are calculated using the adjusted TBs for each of these inter-calibration algorithms using both the WCC and G10 algorithms. The yearly average zonal mean rain accumulation differences are shown for the WCC and G10 algorithms in Figure 5.15 and Figure 5.16, respectively. The WCC algorithm appears to be more sensitive to the warm end calibration point than the cold end, since the inter-calibration algorithm that uses just the warm end point gives almost the same result as the algorithm that uses the two-point inter-calibration. The likely reason for this is that WCC groups all TBs into one histogram for each grid box and uses only the TBs at the warm end of the histogram for retrieving the rain. This makes the rain accumulations much more sensitive to the warm TBs than the cold TBs. Using just the cold end tie point for WCC does increase the consistency of F15 and TMI derived rain, but it is not a sufficient adjustment.

It is less obvious which inter-calibration algorithm performs the best for the G10 rain accumulations, except for those latitudes near the equator. The tropics have the greatest discrepancy between F15 and TMI retrieved rain pre-inter-calibration and show the greatest improvement in the retrieved rain when using the two-point inter-calibration. It is interesting to note that the one-point cold and warm inter-calibrations have hardly any impact on improving the rain consistency in the tropics while the two-point inter-calibration gives extremely good agreement.

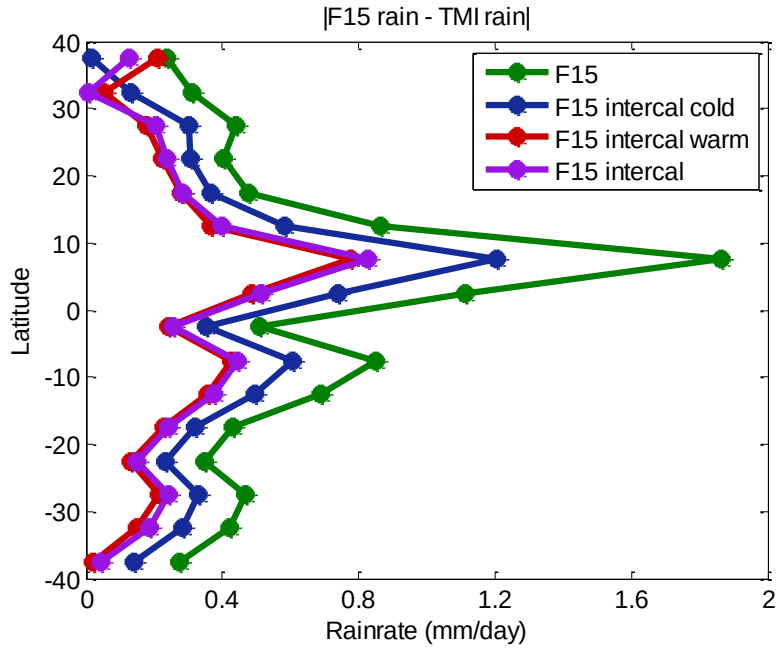

Figure 5.15: WCC zonal mean rain differences F15 - TMI comparing three different types of inter-calibration: constant bias using the cold end DD (intercal cold), constant bias using the warm end DD (intercal warm) and the linear interpolation between the cold and warm DDs (intercal).

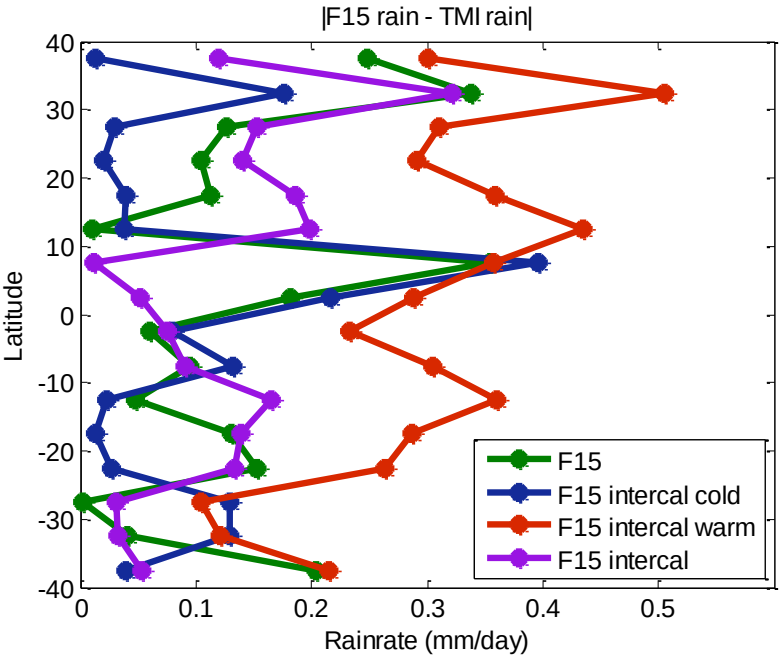

Figure 5.16: G10 zonal mean rain differences F15 - TMI comparing three different types of inter-calibration: constant bias using the cold end DD (intercal cold), constant bias using the warm end DD (intercal warm) and the linear interpolation between the cold and warm DDs (intercal).

This analysis shows that the warm end DD has a significant contribution to the retrieved rain and that large errors could result by just assuming a one-point cold inter-calibration. On the other hand, it is also not appropriate to just assume a constant warm end DD at all temperatures because the G10 algorithm shows that this makes the rain consistency worse. The two-point inter-calibration algorithm is the one that overall provides the best rain agreement for both the WCC and G10 algorithms.

Another conclusion from this analysis is that the WCC algorithm is more sensitive to inter-calibration than the G10 algorithm. This is most likely because the WCC algorithm operates directly on the radiometer TBs to derive a Level 3 rain accumulation product. The G10 Level 3 rain accumulations, on the other hand, are found using the intermediate Level 2 instantaneous rain rates which are derived using an *a priori* database. The retrieved rain rates are then sensitive to the *a priori* information rather than just depending on the TBs, which may in turn cause the inter-calibration to have less of an impact.

Another difference between the G10 and WCC algorithms is the channels used in the rain retrieval. WCC only uses the 19V and 22V channels on F15 and TMI while the G10 algorithm uses all channels available from the instrument. The 19V and 22V channels both have positive calibration differences at the cold and warm ends as well as a positive slope. This results in a decrease in the F15 TBs when F15 is inter-calibrated, which in turn results in more rain retrieved for F15 in the WCC algorithm. The WCC rain accumulations seem to suggest that the inter-calibration adjustments should be larger for 19V and/or 22V since F15 still retrieves less rain than TMI after inter-calibration. On the other hand, the G10 algorithm uses all channels including the H-pol channels which all

have a negative slope for the two-point calibration. It is less obvious for this algorithm what impact increasing or decreasing the TBs through inter-calibration might have on the retrieved rain rates.

5.5 Summary

The impact of microwave radiometer inter-calibration on retrieved rain rates was presented. Level 3 rain accumulations were calculated using two different retrieval methods: the WCC and G10 algorithms. WCC derives monthly rain accumulations directly from the TBs and G10 derives monthly rain accumulations by integrating Level 2 instantaneous rain rates. Rain accumulations were calculated for each algorithm using TB measurements from F15 and TMI, with and without inter-calibration adjustments applied to the TBs. It was shown that inter-calibration has a positive impact on improving the retrieved rain consistency between the two radiometers for both rain retrieval algorithms.

This study validates the work of the GPM X-Cal team since it shows that inter-calibrating the microwave radiometers in the GPM constellation has a significant positive impact on the agreement between rain accumulation products produced by different radiometers.

Chapter 6
Conclusions and Future Study

6.1 Summary

Microwave radiometer inter-calibration is necessary if the radiometer measurements are to be combined into a cohesive data set for scientific studies. The GPM mission seeks to utilize a constellation of radiometers on individual satellites to measure global precipitation. Inter-calibration is an important aspect of the mission, intended to ensure that consistent rain rates are derived among the radiometers in the constellation. This thesis describes the development of an inter-calibration algorithm for conical scanning microwave radiometers that will be used as part of the GPM mission. The inter-calibration algorithm uses vicarious cold calibration to derive a cold end calibration point for microwave radiometers with frequencies from 10 to 37 GHz and 85 to 92 GHz. This method is referred to as the vicarious cold calibration double difference method.

The performance of the vicarious cold calibration double difference method was demonstrated using one year of radiometer data from the AMSR-E and TMI instruments. First, the vicarious cold calibration algorithm was used to derive the cold cal TB for AMSR-E. The cold cal TB was shown to be sensitive to seasonal variability, as well as to instrumental characteristics such as EIA. The inclusion of simulated TBs through the single difference was shown to be effective to account for instrumental characteristics, such as frequency and EIA, as well as geophysical variability that is present in the cold cal TB. The vicarious cold calibration double difference method takes the difference

between the two single differences of two radiometers being inter-calibrated to calculate a calibration difference that is a result of the difference in absolute calibration between the radiometers.

Inter-calibration differences were calculated for AMSR2 and TMI using the vicarious cold calibration double difference method and compared to inter-calibration differences for AMSR2 and TMI using other algorithms. These other algorithms are also being utilized for the GPM mission. Similar calibration differences were found as the other methods, showing that the vicarious cold calibration double difference method is an accurate and valid inter-calibration algorithm.

Estimates of the uncertainty in the vicarious cold calibration double difference were calculated. These uncertainties are a result of potential errors in the geophysical inputs to the simulations that propagate into the inter-calibration. The uncertainties also take into account the fact that simulations improperly model seasonal and diurnal variability. Uncertainties were shown to be less than 0.5 K for most channels, with the horizontally polarized channels and the channels closest to the water vapor line showing the highest uncertainties.

Lastly, the inter-calibration differences were applied to radiometer TB data and used to derive rain accumulations to observe the impact of inter-calibration on the rain retrievals. Two different GPM rain retrieval algorithms were used to derive rain accumulations for the SSM/I F15 and TMI instruments, with and without inter-calibration applied to the radiometer TBs. Inter-calibration was shown to have a positive impact on rain data product consistency between SSM/I F15 and TMI. This analysis confirms that inter-calibration is beneficial to GPM.

6.2 Contributions

- An inter-calibration algorithm using vicarious cold calibration is developed for use with spaceborne microwave imagers.

  > R. A. Kroodsma, D. S. McKague, and C. S. Ruf, "Inter-calibration of microwave radiometers using the vicarious cold calibration double difference method," *J. Selected Topics Remote Sensing*, vol. 5, no. 3, pp. 1006-1013, Jun. 2012.

- Vicarious cold calibration is extended for use at frequencies from 85 to 92 GHz in order to calibrate those channels in addition to the lower frequency channels on microwave imagers.

  > R. A. Kroodsma, D. S. McKague, and C. S. Ruf, "Extension of vicarious cold calibration to 85 – 92 GHz for spaceborne microwave radiometers," *IEEE Trans. Geosci. Remote Sens.*, vol. 51, no. 9, pp. 4743–4751, Sep. 2013.

- Vicarious cold calibration is used to derive the pitch and roll offsets of a satellite with a microwave radiometer onboard. This method shows good agreement with a method that uses geolocation for deriving pitch and roll offsets.

  > R. Kroodsma, D. McKague, and C. Ruf, "Satellite attitude analysis using the vicarious cold calibration method for microwave radiometers," *Proc. 2012 International Geoscience and Remote Sensing Symposium*, Munich, Germany, pp. 3312–3315, 23-27 July 2012.

- Uncertainties in the vicarious cold calibration double difference method are estimated. These uncertainties incorporate errors in the inter-calibration as a result of the geophysical inputs used in the simulations.
- The vicarious cold calibration double difference method is used to derive inter-calibration differences for radiometers included in the GPM mission. These differences are included in the at-launch algorithm for GPM.
- The impact of inter-calibration on retrieved rain rates is analyzed for two different retrieval algorithms: a TB histogram method which gives Level 3 rain accumulations and the GPROF 2010 algorithm which gives Level 2 rain rates and

Level 3 rain accumulations. Inter-calibration has a positive impact on achieving consistency in the retrieved rain from the radiometers.

> R. Kroodsma, D. McKague, and C. Ruf, "Effect of microwave radiometer inter-calibration on rainfall accumulation for the Global Precipitation Measurement mission," *Proc. 2013 International Geoscience and Remote Sensing Symposium*, Melbourne, Australia, 22-26 July 2013.

6.3 Future Work

This section describes four areas of future work to be done related to the work in this thesis. The first area of work focuses on incorporating GMI into the GPM constellation. The next two areas of work involve improvements to the microwave radiometer inter-calibration algorithms. These improvements are: (1) developing a mid-point inter-calibration value; and (2) better quantifying the impact of RTM errors on the inter-calibration. Finally, the fourth area of future work is to continue the analysis of inter-calibration impact on rain accumulation measurements.

6.3.1 Application of Inter-Calibration to GMI

Once GMI is launched on the GPM Core Observatory in February 2014, GMI will need to be added to the constellation of radiometers that have been previously inter-calibrated using TMI as the reference. Inter-calibration offsets will be derived using GMI as the reference radiometer once there are sufficient data from GMI. GMI uses a new four-point onboard calibration system [93] which over-constrains the calibration of the radiometer. The expectation is that this will result in GMI having the best calibration relative to other current radiometers. This will be analyzed to determine if the onboard calibration is stable and accurate enough for the instrument to be used as the calibration standard for the GPM constellation.

6.3.2 Development of a Middle Calibration Point

Deriving a stable calibration value at a temperature between the cold and warm end points would help to improve the inter-calibration algorithm. Currently, a linear interpolation is assumed between the cold and warm calibration points since a reliable

and stable mid-point calibration is not available. A mid-point calibration would aid in determining whether a linear interpolation between the cold and warm ends can be used or if a non-linear assumption is more accurate. One potential Earth target for vicarious calibration at a mid-point temperature is the Antarctic ice sheet, specifically the location known as Dome-C [94]. The microwave frequencies used for GPM do show some sensitivity to annual variations in the ice sheet layers, so this would need to be further analyzed to determine if it can be used as a stable mid-point calibration reference.

6.3.3 RTM Errors in the Inter-Calibration

Section 4.3 presented an initial estimate of the uncertainty in the vicarious cold calibration double difference method, but this estimate only accounted for possible errors in the geophysical inputs to the RTM. Another potential source of error in the inter-calibration is the atmospheric absorption and surface emissivity models used in the RTM. Improved atmosphere absorption [95] and surface emissivity [96] models have been recently developed. These models should be incorporated into the inter-calibration algorithm to analyze whether the use of different models impacts the inter-calibration. If using a different atmosphere or surface model in the RTM significantly impacts the inter-calibration, this should be quantified and included in the uncertainty calculation.

6.3.4 Further Analysis of Inter-Calibration Impact on Retrieved Rain Rates

Chapter 5 presented an analysis of the impact of inter-calibration on retrieved rain rates for two radiometers: SSM/I F15 and TMI. The other radiometers in the GPM constellation, including GMI after it is launched, should also be included in this analysis. Also, the impact of inter-calibration uncertainties on the retrieved rain should be studied.

This study will give an indication of how large the uncertainties in the inter-calibration can be before they significantly impact the rain estimates. If the uncertainties do significantly impact the rain, the inter-calibration algorithm should be re-analyzed to determine ways to lower the uncertainties.

References

[1] M. New, M. Todd, M. Hulme, and P. Jones, "Precipitation measurements and trends in the twentieth century," *Int. J. Climate*, vol. 21, pp. 1899-1922, 2001.

[2] T. G. Huntington, "Evidence for intensification of the global water cycle: Review and synthesis," *J. Hydrol.*, vol. 319, no. 1, pp. 83-95, 2006.

[3] R. P. Allan and B. J. Soden, "Atmospheric warming and the amplification of precipitation extremes," *Science*, vol. 321, pp. 1481-1484, Sep. 2008.

[4] F. J. Wentz, L. Ricciardulli, K. Hilburn, and C. Mears, "How much more rain will global warming bring?," *Science*, vol. 317, pp. 233-235, Jul. 2007.

[5] P. Y Groisman and D. R. Legates, "Documenting and detecting long-term precipitation trends: Where we are and what should be done," *Climate Change*, vol. 42, pp. 243-283, 1995.

[6] D. R. Legates and C. J. Willmott, "Mean seasonal and spatial variability in gauge-corrected, global precipitation," *Int. J. Climatology*, vol. 10, pp. 111-127, 1990.

[7] G. Bloschl and M. Sirapalan, "Scale issues in hydrological modeling – A review," *Hydrol. Process.*, vol. 9, pp. 251-290, 1995.

[8] E. C. Barrett and D. W. Martin, *Use of Satellite Data in Rainfall Monitoring*, Academic Press, 340 pp., 1981.

[9] F. T. Ulaby, R. K. Moore, and A. K. Fung, *Microwave Remote Sensing Fundamentals and Radiometry*, vol. 1, 1981.

[10] P. W. Rosenkranz, "Water vapor microwave continuum absorption: A comparison of measurements and models," *Radio Sci.*, vol. 33, no. 4, pp. 919-928, 1998.

[11] H. J. Liebe, P. W. Rosenkranz, and G. A. Hufford, "Atmospheric 60-GHz oxygen spectrum: New laboratory measurements and line parameters," *J. Quant. Spectrosc. Radiat. Transf.*, vol. 48, pp. 629-643, 1992.

[12] C. G. Griffith, W. L. Woodley, P. G. Grube, D. W. Martin, J. Stout, and D. N. Sikdar, "Rain estimation from geosynchronous satellite imagery – visible and infrared studies," *Mon. Wea. Rev.*, vol. 106, no. 8, pp. 1153-1171, Aug. 1978.

[13] P. A. Arkin, R. Joyce, and J. E. Janowiak, "The estimation of global monthly mean rainfall using infrared satellite data: The GOES precipitation index (GPI)," *Remote Sens. Rev.*, vol. 11, pp. 107-124, 1994.

[14] F. Richards and P. Arkin, "On the relationship between satellite-observed cloud cover and precipitation," *Mon. Wea. Rev.*, vol. 109, no. 5, pp. 1081-1093, May 1981.

[15] S. Lovejoy and G. L. Austin, "The sources of error in rain amount estimating schemes from GOES visible and IR satellite data," *Mon. Wea. Rev.*, vol. 107, no. 8, pp. 1048-1054, Aug. 1979.

[16] T. Wilheit, "The electrically scanning microwave radiometer (ESMR) experiment," in *The Nimbus-5 User's Guide*, NASA/Goddard Space Flight Center, Greenbelt, MD, pp. 59-105, 1971.

[17] L. J. Allison, E. B. Rodgers, T. T. Wilheit, and R. W. Fett, "Tropical cyclone rainfall as measured by the Nimbus Electrically Scanning Microwave Radiometer," *Bull. Amer. Meteor. Soc.*, vol. 55, no. 9, pp. 1074 – 1089, Sep. 1974.

[18] T. T. Wilheit, A. T. C. Chang, M. S. V. Rao, E. B. Rodgers, and J. S. Theon, "A satellite technique for quantitatively mapping rainfall rates over the oceans," *J. Appl. Meteor.*, vol. 16, no. 5, pp. 551-560, May 1977.
[19] T. Wilheit, "The electrically scanning microwave radiometer (ESMR) experiment," in *The Nimbus-6 User's Guide*, NASA/Goddard Space Flight Center, Greenbelt, MD, pp. 87-108, 1975.
[20] J. A. Weinman and Pl. J. Guetter, "Determination of rainfall distributions from microwave radiation measured by the Nimbus 6 ESMR," *J. Appl. Meteor.*, vol. 16, no. 4, pp. 437-442, Apr. 1977.
[21] E. G. Njoku, J. M. Stacey, and F. T. Barath, "The Seasat scanning multichannel microwave radiometer (SMMR): Instrument description and performance," *IEEE J. Ocean. Engin.*, vol. 5, no. 2, pp. 100-115, Apr. 1980.
[22] J. P. Hollinger, J. L. Peirce, and G. A. Poe, "SSM/I Instrument Evaluation," *IEEE Trans. Geosci. Remote Sens.*, vol. 28, no. 5, pp. 781-790, Sep. 1990.
[23] T. Wilheit et al, "Algorithms for the retrieval of rainfall from passive microwave measurements," *Remote Sens. Rev.*, vol. 11, no. 1, pp. 163-194, 1994.
[24] R. R. Ferraro and G. F. Marks, "The development of SSM/I rain-rate retrieval algorithms using ground-based radar measurements," *J. Atmos. Oceanic Technol.*, vol. 12, no. 4, pp. 755 – 770, Aug. 1995.
[25] A. T. C. Chang, L. S. Chiu, G. Yang, "Diurnal cycle of oceanic precipitation from SSM/I data," *Mon. Wea. Rev.*, vol. 123, no. 11, pp. 3371–3380, Nov. 1995.
[26] C. Kummerow, W. Barnes, T. Kozu, J. Shiue, and J. Simpson, "The Tropical Rainfall Measuring Mission (TRMM) sensor package," *J. Atmos. Ocean. Technol*., vol. 15, no.3, pp. 809-817, Jun. 1998.
[27] J. Simpson, R. F. Adler, and G. R. North, "A proposed Tropical Rainfall Measuring Mission (TRMM) satellite," *Bull. Amer. Meteor. Soc.*, vol 69, no. 3, pp. 178-295, Mar. 1988.
[28] R. F. Adler, J. –J. Wang, G. Gu, and G. J. Huffman, "A ten-year rainfall climatology based on a composite of TRMM products," *J. Meteorol. Soc. Japan*, vol. 87A, pp. 281-293, 2009.
[29] S. W. Nesbitt and E. J. Zipser, "The diurnal cycle of rainfall and convective intensity according to three years of TRMM measurements," *J. Climate*, vol. 16, no. 10, pp. 1456-1475, May 2003.
[30] W. –K. Tao et al., "Retrieval of latent heating from TRMM measurements," *Bull. Amer. Meteor. Soc.*, vol. 87, no. 11, pp. 1555-1572, Nov. 2006.
[31] W. –K. Tao, "Goddard Cumulus Ensemble (GCE) model: Application for understanding precipitation processes, *Meteorological Monographs*, vol. 29, no. 51, Jan. 2003.
[32] R. J. Joyce, J. E. Janowiak, P. A. Arkin, and P. Xie, "A Method that Produces Global Precipitation Estimates from Passive Microwave and Infrared Data at High Spatial and Temporal Resolution," *J. Hydrometeor.*, vol. 5, no. 3, pp. 487-503, Jun. 2004.
[33] R. F. Adler, G. J. Huffman, D. T. Bolvin, S. Curtis, and E. J. Nelkin, "Tropical rainfall distributions determined using TRMM combined with other satellite and rain gauge information," *J. Appl. Meteor.*, vol. 39, no. 12, pp. 2007-2023, Dec. 2000.
[34] A. Y. Hou, S. Q. Zhang, A. M. da Silva, W. S. Olson, C. D. Kummerow, and J. Simpson, "Improving global analysis and short-range forecast using rainfall and moisture observations derived from TRMM and SSM/I passive microwave sensors," *Bull. Amer. Meteor. Soc.*, vol. 82, no. 4, pp. 659-680, Apr. 2001.
[35] K. Imaoka and R. W. Spencer, "Diurnal variation of precipitation over the tropical oceans observed by TRMM/TMI combined with SSM/I," *J. Climate*, vol. 13, no. 23, pp. 4149-4158, De. 2000.

[36] A. Y. Hou, G. Skofronick-Jackson, C. D. Kummerow, and J. M. Shepherd, "Global precipitation measurement" in Precipitation: Advances in Measurement, Estimation and Prediction, S. Michaelides, Ed., Springer, 2008, pp. 131-170.

[37] D. A. Newell, G. Rait, T. Ta, B. Berdanier, D. Draper, M. Kubitschek, and S. Krimchansky, "GPM Microwave Imager design, predicted performance and status," *Proc. International Geoscience and Remote Sensing Symposium (IGARSS)*, Vancouver, BC, Canada, pp. 546-549, 25-29 July 2011.

[38] Y. Senbokuya, S. Satoh, K. Furukawa, M. Kojima, H. Hanado,N. Takahashi, T. Iguchi, and K. Nakamura, "Development of the spaceborne dual frequency precipitation radar for the Global Precipitation Measurement mission," *Proc. IEEE International Geoscience and Remote Sensing Symposium (IGARSS)*, Anchorage, AK, USA, pp. 3566 – 3569, 20-24 Sep. 2004.

[39] G. M. Skofronick-Jackson, M. –J. Kim, J. A. Weinman, and D. –E. Chang, "A physical model to determine snowfall over land by microwave radiometry," *IEEE Trans. Geosci. Remote Sens.*, vol. 42, no. 5, pp. 1047 – 1058, May 2004.

[40] P. N. Swanson and A. L. Riley, "The Seasat scanning multichannel microwave radiometer (SMMR): Radiometric calibration algorithm development and performance," *IEEE J. Ocean. Engin.*, vol. 5, no. 2, pp. 116-124, Apr. 1980.

[41] E. G. Njoku, E. J. Christensen, and R. E. Cofield, "The Seasat scanning multichannel microwave radiometer (SMMR): Antenna pattern corrections – Development and implementation," *IEEE J. Ocean. Engin.*, vol. 5, no. 2, pp. 125-137, Apr. 1980.

[42] F. J. Wentz, P. Ashcroft, and C. Gentemann, "Post-launch calibration of the TRMM microwave imager," IEEE Trans. Geosci. Remote Sens., vol. 39, no. 2, pp. 415-422, Feb. 2001.

[43] K. Imaoka, Y. Fujimoto, M. Kachi, T. Takeshima, K. Shiomi, H. Mikai,T. Mutoh, M. Yoshikawa, and A. Shibata, "Post-launch calibration and data evaluation of AMSR-E," in *Proc. IGARSS*, vol. 1, pp. 666–668, Jul. 2003.

[44] C. S. Ruf, Y. Hu, and S. T. Brown, "Calibration of WindSat polarimetric channels with a vicarious cold reference," *IEEE Trans. Geosci. Remote Sens.*, vol. 44, no. 3, pp. 470 – 475, Mar. 2006.

[45] C. S. Ruf, "Detection of calibration drifts in spaceborne microwave radiometers using a vicarious cold reference," *IEEE Trans. Geosci. Remote Sens*., vol. 38, no. 1, pp. 44-52, Jan. 2000.

[46] S. T. Brown and C. S. Ruf, "Determination of a hot blackbody reference target over the Amazon Rainforest for the on-orbit calibration of microwave radiometers," *AMS J. Oceanic Atmos. Tech.*, vol. 22, no. 9, pp. 1340-1352, 2005.

[47] U.S. National Centers for Environmental Prediction, Updated Daily: NCEP FNL Operational Model Global Tropospheric Analyses, Continuing From July 1999. Dataset ds083.2 Published by the CISL Data Support Section at the National Center for Atmospheric Research. Boulder, CO [Online]. Available: http://dss.ucar.edu/datasets/ds083.2/

[48] J. P. Peixoto and A. H. Oort, "The climatology of relative humidity in the atmosphere," *J. Climate*, vol. 9, no. 12, pp. 3443 – 3463, Oct. 1996.

[49] R. W. Reynolds and T. M. Smith, "A high-resolution global sea surface temperature climatology," *J. Climate*, vol. 8, no. 6, pp. 1571-1583, Jun. 1995.

[50] R. Wu and J. A. Weinman, "Microwave radiances from precipitating clouds containing aspherical ice, combined phase, and liquid hydrometeors," *J. Geophys. Res.*, vol. 89, no. D5, pp 7170-7178, Aug. 1984.

[51] T. T. Wilheit, A. T. C. Chang, J. L. King, E. B. Rodgers, R. A. Nieman, B. M. Krupp, A. S. Milman, J. S. Stratigos, and H. Siddalingaiah, "Microwave radiometric observations near

19.35, 92, and 183 GHz of precipitation in tropical storm Cora," *J. Appl. Meteorol.*, vol. 21, pp. 1137-1145, Aug. 1982.
[52] I. M. Hakkarinen and R. F. Adler, "Observations of convective precipitation at 92 and 183 GHz: Aircraft results," *Meteor. Atmos. Phys.*, vol. 38, pp. 164-182, 1988.
[53] R. W. Spencer, H. M. Goodman, and R. E. Hood, "Precipitation retrieval over land and ocean with the SSM/I: Identification and characteristics of the scattering signal," *J. Atmos. Oceanic. Technol.*, vol. 6, no. 2, pp. 254–273, Apr. 1989.
[54] A. P. Stogryn, C. T. Butler, and T. J. Bartolac, "Ocean surface wind retrievals from special sensor microwave/imager data with neural networks," *J. Geophys. Res.*, vol. 90, pp. 981-984, 1994.
[55] N. C. Grody, "Classification of snow cover and precipitation using the Special Sensor Microwave Imager," *J. Geophys. Res.*, vol. 96, no. D4, pp. 7423-7435, Apr. 1991.
[56] R. F. Adler, A. J. Negri, P. R. Keehn, and I. M. Hakkarinen, "Estimation of monthly rainfall over Japan and surrounding waters from a combination of low-orbit microwave and geosynchronous IR data," *J. Appl. Meteor.*, vol. 32, pp. 335-356, Feb. 1993.
[57] T. Meissner and F. J. Wentz, "The complex dielectric constant of pure and sea water from microwave satellite observations," *IEEE Trans. Geosci. Remote Sens.*, vol. 42, no. 9, pp. 1836–1849, Sep. 2004.
[58] J. Hollinger, "Passive microwave measurements of sea surface roughness," *IEEE Trans. Geosci. Electron.*, vol. 9, no. 3, pp. 165–169, Jul. 1971.
[59] A. Stogryn, "The emissivity of sea foam at microwave frequencies," *J. Geophys. Res.*, vol. 77, no. 9, pp. 1659–1666, Mar. 1972.
[60] T. Wilheit, "A model for the microwave emissivity of the ocean's surface as a function of wind speed," *IEEE Trans. Geosci. Electron.*, vol. GE-17, no. 4, pp. 244–249, Oct. 1979.
[61] G. Elsaesser, "A parametric optimal estimation retrieval of the nonprecipitating parameters over the global oceans,"M.S. thesis, Colorado State Univ., Fort Collins, CO, 2006.
[62] T. Meissner and F. J.Wentz, "An updated analysis of the ocean surface wind direction signal in passive microwave brightness temperatures," *IEEE Trans. Geosci. Remote Sens.*, vol. 40, no. 6, pp. 1230–1240, Jun. 2002.
[63] H. J. Liebe, G. A. Hufford, and T. Manabe, "A model for the complex permittivity of water at frequencies below 1 THz," *Int. J. Infr. Millim. Waves*, vol. 12, no. 7, pp. 659–675, 1991.
[64] S. Platnick, M. D. King, S. A. Ackerman, W. P. Menzel, B. A. Baum, J. C. Riedi, and R. A. Frey, "The MODIS cloud products: algorithms and examples from Terra," *IEEE Trans. Geosci. Remote Sens.*, vol. 41, no. 2, pp. 459-473, Feb. 2003.
[65] A. P. Stogryn, C. T. Butler, and T. J. Bartolac, "Ocean surface wind retrievals from special sensor microwave/imager data with neural networks," *J. Geophys. Res.*, vol. 90, pp. 981-984, 1994.
[66] W. E. Purdy, P. W. Gaiser, G. A. Poe, E. A. Uliana, T. Meissner, and F. J. Wentz, "Geolocation and pointing accuracy analysis for the WindSat sensor," *IEEE Trans. Geosci. Remote Sens.*, vol. 44, no. 3, pp. 496–505, Mar. 2006.
[67] T. Meissner and F. J. Wentz, "Polarization rotation and the third Stokes parameter: The effects of spacecraft attitude and Faraday rotation," *IEEE Trans. Geosci. Remote Sens.*, vol. 44, no. 3, pp. 506–515, Mar. 2006.
[68] G. A. Poe, E. A. Uliana, B. A. Gardiner, T. E. vonRentzell, D. B. Kunkee, "Geolocation Error Analysis of the Special Sensor Microwave Imager/Sounder," *IEEE Trans. Geosci. Remote Sens.*, vol. 46, no. 4, pp. 913-922, April 2008.
[69] D. A. Vallado, W. D. McClain, *Fundamentals of Astrodynamics and Applications*, El Segundo, CA: Microcosm Press, 2004, pp. 140-145.
[70] I. Corbella, A. J. Gasiewski, M. Klein, and J. R. Piepmeier, "Compensation of elevation angle variations in polarimetric brightness temperature measurements from airborne

microwave radiometers," *IEEE Trans. Geosci. Remote Sens.*, vol. 39, no. 1, pp. 193–195, Jan. 2001.

[71] P. Gaiser, et. al., "The WindSat Spaceborne Polarimetric Microwave Radiometer: Sensor Description and Early Orbit Performance," *IEEE Trans. Geosci. Remote Sens.*, vol. 42, no. 11, pp. 2347-2361, Nov. 2004.

[72] M. C. Colton and G. A. Poe, "Intersensor calibration of DMSP SSM/I's: F-8 to F-14, 1987-1997," *IEEE Trans. Geosci. Remote Sens.*, vol. 37, no. 1, pp. 418-439, Jan. 1999.

[73] C. Cao, M. Weinreb, and H. Xu, "Predicting simultaneous nadir overpasses among polar-orbiting meteorological satellites for the intersatellite calibration of radiometers," *J. Atmos. Ocean. Technol.*, vol. 21, no. 4, pp. 537-542, Apr. 2004.

[74] B. Yan and F. Weng, "Intercalibration between Special Sensor Microwave Imager/Sounder and Special Sensor Microwave Imager," *IEEE Trans. Geosci. Remote Sens.*, vol. 46, no. 4, pp. 984-995, Apr. 2008.

[75] F. J. Wentz, P. Ashcroft, and C. Gentemann, "Post-launch calibration of the TRMM microwave imager," *IEEE Trans. Geosci. Remote Sens.*, vol. 39, no. 2, pp. 415-422, Feb. 2001.

[76] M. R. P. Sapiano, W. K. Berg, D. S. McKague, and C. D. Kummerow, "Toward an intercalibrated fundamental climate data record of the SSM/I sensors," *IEEE Trans. Geosci. Remote Sens.*, vol. 51, no. 3, pp. 1492-1503, March 2013.

[77] T. Kawanishi et al., "The Advanced Microwave Scanning Radiometer for the Earth Observing System (AMSR-E), NASDA's contribution to the EOA for global energy and water cycle studies," *IEEE Trans. Geosci. Remote Sens.*, vol. 41, no. 2, pp. 184–194, Feb. 2003.

[78] D. B. Kunkee, G. A. Poe, D. J. Boucher, S. D. Swadley, Y. Hong, J. E. Wessel, and E. A. Uliana, "Design and evaluation of the first Special Sensor Microwave Imager/Sounder," *IEEE Trans. Geosci. Remote Sens.*, vol. 46, no. 4, pp. 863–883, Apr. 2008.

[79] K. Imaoka, T. Maeda, M. Kachi, M Kasahara, N. Ito, and K. Nakagawa, "Status of AMSR2 instrument on GCOM-W1," *Proc. SPIE 8528, Earth Observing Missions and Sensors: Development, Implementation, and Characterization II*, 852815, Nov. 2012.

[80] N. Karouche, C. Goldstein, A. Rosak, C. Malassingne, and G. Raju, "Megha-Tropiques satellite mission: In flight performances results," *Proc. 2012 IEEE International Geoscience and Remote Sensing Symposium*, Munich, Germany, pp. 4684–4687, 22-27 July 2012.

[81] D. McKague, C. Ruf and J. Puckett, "Vicarious calibration of Global Precipitation Measurement microwave radiometers," Proc. 2008 IEEE International Geoscience and Remote Sensing Symposium, 2008, pp. 459-462.

[82] K. Gopalan, L. Jones, T. Kasparis, and T. Wilheit, "Inter-satellite radiometer calibration of WindSat, TMI, and SSMI," Proc. 2008 IEEE International Geoscience and Remote Sensing Symposium, 2008, pp. 1216-1219.

[83] T. Wilheit, W. Berg, L. Jones, R. Kroodsma, D. McKague, C. Ruf, and M. Sapiano, "A consensus calibration based on TMI and WindSat," Proc. 2011 IEEE International Geoscience and Remote Sensing Symposium, 2011, pp. 2641-2644.

[84] D. P. Dee et al, "The ERA-Interim reanalysis: Configuration and performance of the data assimilation system," *Q. J. R. Meteorol. Soc.*, vol. 137, no. 656, pp. 553–597, Apr. 2011.

[85] M. M. Rienecker et al, "MERRA – NASA's modern-era retrospective analysis for research and applications," *J. Climate*, vol. 24, no. 14, pp. 3624–3648, Jul. 2011.

[86] S. K. Biswas, S. Farrar, K. Gopalan, A. Santos-Garcia, W. L. Jones, and S. Bilanow, "Intercalibration of microwave radiometer brightness temperatures for the Global Precipitation Measurement mission," *IEEE Trans. Geosci. Remote Sens.*, vol. 51, no. 3, pp.1465-1477, March 2013.

[87] T. T. Wilheit, "Comparing calibrations of similar conically scanning window-channel microwave radiometers," *IEEE Trans. Geosci. Remote Sens.*, vol. 51, no. 3, pp. 1453-1464, March 2013.
[88] T. T. Wilheit, A. T. C. Chang, and L. S. Chiu, "Retrieval of monthly rainfall indices from microwave radiometric measurements using probability distribution functions," *J. Atmos. Oceanic Tech.*, vol. 8, no. 1, pp. 118-136, Feb. 1991.
[89] A. T. C. Chang, L. S. Chiu, C. Kummerow, J. Meng, and T. T. Wilheit, "First results of the TRMM Microwave Imager (TMI) monthly oceanic rain rate: Comparison with SSM/I," *Geophys. Res. Letters*, vol. 26, no. 15, pp. 2379-2382, Aug. 1999.
[90] C. D. Kummerow, W. S. Olson, and L. Giglio, "A simplified scheme for obtaining precipitation and vertical hydrometeor profiles from passive microwave sensors," *IEEE Trans. Geosci. Remote Sens.*, vol. 34, no. 5, pp. 1213-1232, Sep. 1996.
[91] C. D. Kummerow, Y. Hong, W. S. Olson, S. Yang, R. F. Adler, J. McCollum, R. Ferraro, G. Petty, D. –B. Shin, an T. T. Wilheit, "The evolution of the Goddard Profiling Algorithm (GPROF) for rainfall estimation from passive microwave sensors," *J. Appl. Meteor.*, vol 40, no. 11, pp. 1801–1820, Nov. 2001.
[92] C. D. Kummerow, S. Ringerud, J. Crook, D. Randel, and W. Berg, "An observationally generated a priori database for microwave rainfall retrievals," *J. Atmos. Ocean Technol.*, vol 28, no. 2, pp. 113–130, Feb. 2011.
[93] J. B. Sechler, "GPM microwave imager selected calibration features and predicted performance," *Proc. International Geoscience and Remote Sensing Symposium (IGARSS)*, Barcelona, Spain, pp. 5237–5239, 23-28 July 2007.
[94] G. Macelloni, M. Brogioni, P. Pampaloni, A. Cagnati, and M. R. Drinkwater, "DOMEX 2004: An experimental campaign at Dome-C Antarctica for the calibration of spaceborne low-frequency microwave radiometers," *IEEE Trans. Geosci. Remote Sens.*, vol. 44, no. 10, pp. 2642–2653, Oct. 2006.
[95] V. H. Payne, E. J. Mlawer, K. E. Cady-Pereira, and J. Moncet, "Water vapor continuum absorption in the microwave," *IEEE Trans. Geosci. Remote Sens.*, vol. 49, no. 6, pp. 2194–2208, Jun. 2011.
[96] T. Meissner and F. J. Wentz, "The emissivity of the ocean surface between 6 and 90 GHz over a large range of wind speeds and earth incidence angles," *IEEE Trans. Geosci. Remote Sens.*, vol. 50, no. 8, pp. 3004–3026, Aug. 2012.